Observing Coupled Nuclear and Electronic Motions Involved in Intramolecular Hydrogen Bonding and Proton Transfer with Ultrafast Multicolor Spectroscopy

Caroline M. Loe

A dissertation
submitted in partial fulfillment of the
requirements for the degree of

Doctor of Philosophy

University of Washington

2024

Reading Committee:
Munira Khalil, Chair
Anne McCoy
Marjorie Olmstead

Program Authorized to Offer Degree:
Chemistry

University of Washington

Abstract

Observing Coupled Nuclear and Electronic Motions Involved in Intramolecular Hydrogen Bonding and Proton Transfer with Ultrafast Multicolor Spectroscopy

Caroline M. Loe

Chair of the Supervisory Committee:
Munira Khalil
Chemistry

The use and development of of multidimensional spectroscopy have allowed scientists to uncover coupled motions of electrons and nuclei in solution-state systems. Wavelengths ranging from X-ray to infrared offer both localized and delocalized pictures of the coupled degrees of freedom in solution and their influence on one another. As multidimensional, multicolor spectroscopy develops further, experiments and calculations in tandem have aided in understanding the coupled nuclear and electronic motions involved in fundamental chemical processes such as intramolecular hydrogen bonding (IHB) and proton transfer. IHB mediates many solution-phase reactions in chemistry and biology such as protein folding, DNA replication, proton transfer, and more, and is a key component of many molecular structures. Model complexes offer a convenient approach to systematically investigate IHB and proton transfer because they are much smaller than many systems found in nature and used in industry. 10-Hydroxybenzo[h]quinoline (HBQ) is a particularly useful, synthetically tunable, model complex for studying both proton transfer and IHB. It undergoes excited state intramolecular proton transfer (ESIPT), while the proton donor and acceptor participate in a strong intramolecular hydrogen bond.

To understand the relationship between hydrogen bonding, proton transfer and the electronic and nuclear structure of HBQ, we must be able to examine the whole molecule and

the microscopic interactions within the molecule. Infrared and X-ray spectroscopy provide a complementary understanding of the atomic and electronic fluctuations affected by and involved in hydrogen bonding. Electronic spectroscopy in the UV-visible region reports on the entire delocalized electronic structure of the molecule, while X-ray spectroscopy also offers deeper insight to the local electronic structure in an atom of interest. As a combination of femtosecond pulses used in the form of pulsed light, these three wavelength regions (infrared, UV-Vis, and X-ray) serve as powerful spectroscopic tools to investigate ultrafast chemical reactions. This dissertation presents the use of transient X-ray absorption spectroscopy (t-XAS) calculations and multidimensional vibrational-electronic (VE) spectroscopy to investigate the coupled electronic and nuclear motions involved in IHB and ESIPT in HBQ, as well as recent advances in VE experimental development.

One- and two-dimensional vibrational-electronic (1D and 2D VE) spectroscopy utilize two vibrationally-resonant pump pulses to excite ground state vibrations, and an electronically-resonant visible or near-UV probe pulse to observe the changes in the electronic absorption spectrum caused by the interaction of the pump with a sample of interest. This work details improvements made to the recently developed 1D and 2D VE experiments and their ongoing experimental challenges. In particular, the addition of a broadband visible probe source and a broader infrared pump with improved stability and increased pulse energies has enabled the study of new systems with electronic absorption in the near-UV. Experimental protocols have also been optimized to improve data collection times, replicability, and processing. Polarization-selective 1D and 2D VE spectroscopy are used to investigate the coupled low- and high-frequency modes in the $S_1 \leftarrow S_0$ electronic transition of HBQ. Coherent low-frequency oscillations are observed in the 1D VE spectra at 242 cm^{-1} and 386 cm^{-1}, coupled to the electronic transition through the high-frequency OH stretch. 2D VE spectra at three time delays (τ_2) reveal that regions of the ground state OH stretch couple differently to the $S_1 \leftarrow S_0$ transition, and likely oscillate at the same low frequencies as observed in the

1D experiments.

On the electronic excited state, intramolecular hydrogen bonding mediates the ESIPT in HBQ. The proton donor and acceptor atoms undergo significant changes to their local electronic environments during and following proton transfer. Transient X-ray absorption calculations at the oxygen (proton donor) and nitrogen (acceptor) K-edges reveal that the local electronic environment of each is influenced by the coherent oscillations as HBQ relaxes through the excited vibrational manifold of the electronic potential. Shifting X-ray absorption peak energies report on the changes to each local electronic environment in the proton transfer moiety. This is the first successful example of using transient X-ray spectroscopy calculations to track an ESIPT, and it paves the way for future experiments at X-ray free electron laser facilities.

TABLE OF CONTENTS

LIST OF FIGURES

LIST OF TABLES

GLOSSARY

BBNUV: Broadband near-ultraviolet, roughly spanning the wavelength region around 350-450 nm

ESIPT: Excited state intramolecular proton transfer

ESA: Excited state absorption

2D EV: Two-dimensional electronic-vibrational spectroscopy

FFT: Fast Fourier transform, which is the discrete Fourier transform algorithm used in MATLAB

FS: Femtosecond (10^{-15})

FTIR: Fourier-transform infrared spectroscopy

GSB: Ground state bleach

HBQ: 10-hydroxybenzo[h]quinoline

IHB: Intramolecular hydrogen bonding

IR: Infrared

IRF: Instrument response function

K-EDGE: Relating to the excitation of an electron from a 1s core orbital

MIR: Mid-infrared

SNP: Sodium nitroprusside

UV-VIS: Ultraviolet-visible spectroscopy

1D VE: One-dimensional vibrational-electronic spectroscopy

2D VE: Two-dimensional vibrational-electronic spectroscopy

VIBRONIC TRANSITION: A transition that has both vibrational and electronic character (neither purely vibrational nor purely electronic)

VIBRONIC COUPLING: The interplay or relationship between two states with electronic and vibrational character that have an effect on one another

ACKNOWLEDGMENTS

A Ph.D. would not have been possible to complete without the help and support of many people. First, thank you to my advisor, Dr. Munira Khalil for her steadfast confidence that even amidst the setbacks and unanticipated roadblocks that come with setting up an entirely new laser system, I could and would rebuild the lab to achieve a functioning experiment again. I owe a massive thank you to Dr. Niranjan Govind for his endless patience and enthusiasm in teaching me about computational chemistry and theory. I never felt embarrassed for asking naive questions. My experience as a pandemic grad student was made into an extremely productive period thanks to his collaboration and tutelage.

There are many people who work in administrative and support roles in the Chemistry Department and make graduate students' work possible. Thank you to Loch Hickock and Ella Miltner in the Chemistry Storeroom, who saved more than one experiment, contributed to more experiments than I can count, and were always friendly faces to see in the Bagley Hall basement. Thank you to Kevin Soderlund, who helped with the logistics of ordering and installing a new (and very heavy) laser system and the accompanying electrical work. Thank you especially to Nick Breen for helping us keep stable temperatures and humidity in the laser labs, which is no easy feat in a building this old.

Thank you to past and current Khalil Krew members. Thanks to Chelsea Liekhus-Schamltz, who taught me about X-ray spectroscopy, that "writing is thinking," and much more. I have thought (and written) a lot over the last few months. Thanks to Jason Sandwisch for his drive to understand and fix the tiniest of details in any lab, and his enthusiasm for trying new ways to stay productive. Thank you to Megan Klein for her support, friendship, amazing pep talks, and constant voice of reason. Thanks to Ben Poulter

for his friendship and willingness to hear about the latest problems in lab. I can't wait to see the amazing research he does as a beamline scientist. Thanks to Zhaoyuan Yang, Amke Nimmrich, Bailey Vahsholtz, Srijan Chatterjee, William Miller, Will Jeffries, Somnath Biswas, Doyk Hwang, and Lily Von Feldt for their camaraderie, support, patience, and feedback. Thank you to Casey Bisted who began this journey in the Khalil group with me. I valued the time we spent talking back and forth between our laser labs, the input we offered one another on our research, and most of all the many hours we spent together not doing any science. Finally, I am endlessly grateful to Rob Weakly, who taught me everything I needed to know (and more) to become independent in a laser lab. His steady presence and sarcasm were sorely missed after he graduated. I know he will use his incredible gift as a teacher to support many more students to come, and I'm thankful that I got to be one of them.

Friends in Seattle made pandemic life bearable and frequently fun; without them, completing a PhD would have been exponentially harder. Micaela and Casey were my "pandemic pod" — I would not have made it through that era of grad school (and all the rest) without them. Thank you also to the many friends who traveled to Seattle to visit and explore with me. Anne, Maddie, Katie, Danielle, Lisa, Rose, and Monica — your visits were bright spots over the last five years and I'm looking forward to being able to return the favor soon.

My family's support has meant a great deal to me, and not only over the last five years. I credit my parents with many things, but one of the most helpful was that they taught me that math was fun! I have fond memories of playing math games like "Hurkle," counting pennies in the car, and doing math with smarties and m & m's at the kitchen table after lunch. Even more important than encouraging my math skills has been their support for me to study what I wanted to study, whether it was music, math, chemistry, or Spanish. Not only did they encourage me to pursue new interests, but they were also actively interested in hearing about what I was learning. Thank you also to my sisters, Abby, Katie, and Maren, for their support, willingness to commiserate, and desire to travel to Seattle. (Aunt Irene

would have approved.) I couldn't have asked for a more wonderful family.

If I had written my thesis acknowledgements by hand, then this last bit would be a little smudged. Peder, there was never a time when the years of long distance weren't worth it, but I'm so glad we plan to never do that again. The last year of my Ph.D. was the hardest in many ways, and I don't have the words to express how much it has meant to be able to come home to you every day. I am more grateful than you know for your patience, love, steadfast support, flexibility, kindness, (I could keep going) and sense of humor. I love you.

DEDICATION

For Irene, the first chemist in my family.

Chapter 1

INTRODUCTION

From a chemist's perspective, it is imperative to understand why and how chemical reactions take place. At first, this goal may seem straightforward; understand the underlying mechanisms of chemical reactions in order to gain access to chemical truths. Unfortunately the reality of our chemical understanding is still quite limited. The details of some of the most fundamental reactions and interactions, such as intramolecular hydrogen bonding and proton transfer have yet to be fully understood. Part of the challenge in understanding these reactions is that they frequently occur on an ultrafast timescale. Proton transfer is among one of the fastest chemical reactions currently known, occurring down to within ones to tens of femtoseconds. [1] For perspective on this scale, there are as many femtoseconds in one second (10^{15} fs = 1 s) as there are seconds in roughly 31.7 million years (10^{15} s = 3.17 x 10^{7} years). Central to our understanding of a reaction's mechanism is information on the timescales and order of various steps in the reaction. In order to learn this information, it is necessary to develop tools with ultrafast time resolution. During a chemical reaction, a molecule may experience changes to both nuclear and electronic degrees of freedom (motions of atoms and electrons). These degrees of freedom may interact with and influence one another, which means that we need a way to access the timescales and to differentiate between various motions in a molecule. Luckily, each molecule has unique "spectral signatures," dictated by its nuclear (atomic) and electronic structure. Time-resolved spectroscopy allows us to access and monitor these spectral signatures.

1.1 Hydrogen Bonding

Hydrogen bonding is an extremely well-studied yet poorly understood chemical phenomenon. It gives water the unique properties that allow life on Earth to flourish, but is the subject of millions of studies. Hydrogen bonding is generally considered to be the electrostatic attraction between a hydrogen covalently bonded to a hydrogen bond donor and an acceptor, which are typically electronegative atoms such as oxygen, nitrogen, or fluorine. Seemingly simple, it facilitates many chemical reactions such as inter- and intramolecular proton transfers. For example, proton transfers in many protein interactions are facilitated by intermolecular hydrogen bonding [2], and the structures of proteins and nucleic acids (biomolecules) depend on hydrogen bonding as well. [3] Hydrogen bonds also stabilize DNA at various locations within the strands and play an important role in DNA replication. [4]

Excited state hydrogen bonding is integral to many photophysical reactions. Hydrogen bonding can facilitate energy redistribution or relaxation and dictate pathways from excited electronic states to the ground state. [5] Many hydrogen bonded systems in solution also display photochromism of the electronic absorption spectrum, which can be tuned through intermolecular hydrogen bonding with the solvent. [6] The dynamics of hydrogen bonds on the excited state are dictated by the electronic redistribution accompanying an electronic excitation and by the vibrational motion of the rest of the complex surrounding the hydrogen bond donor and acceptor. [7]

Systems in solution are naturally disordered due to interactions between solute and solvent. Infrared spectroscopy is an excellent structural probe of hydrogen bonded systems in solution. It reports on the structural effects of hydrogen bonding and is sensitive to solute-solvent interactions. Furthermore, developments in ultrafast laser systems have enabled the time-resolved study of hydrogen bonding in solution on the pico- to femtosecond timescale. Infrared and terahertz studies on the electronic ground state have revealed valuable information about the strength and effect of hydrogen bonds on molecules in solution. [8–11] As shown in Fig. 1.1, hydrogen bonding has a pronounced effect on the infrared spectra of

molecules in solution. [12] A free OH stretch has a narrow frequency of ≈3600 cm^{-1} (Fig. 1.1(a)). A weakly hydrogen bonded OH stretch (Fig. 1.1(b)) is slightly red-shifted and has a broader line shape than the free OH stretch. A moderate to strongly hydrogen bonded OH stretch (Fig. 1.1(c)) is even broader, further red-shifted, and has structure on top of the infrared stretching band. This structure can arise from anharmonically coupled low frequency modes to the OH stretch and combination bands of lower frequency vibrations.

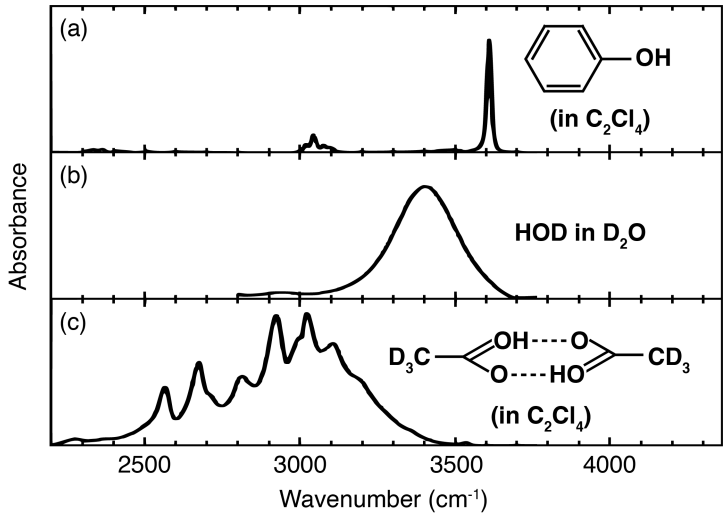

Figure 1.1. Ground state FTIR spectra of free OH stretch (a), weakly hydrogen bonded OH stretch (b), and medium-strongly hydrogen bonded OH stretch (c). Adapted from Ref. 12 with permission. Copyright 2004 American Chemical Society.

Intramolecular hydrogen bonding is present in many important systems and biochemical processes. It is distinct from intermolecular hydrogen bonding in that the hydrogen bond donor and acceptor are located within the same molecule. An intramolecular hydrogen bond has many effects on a molecule's physical, chemical, and biological properties. It can induce a more planar structure by inhibiting torsional motion and introducing structural constraints, or it can have a stabilizing effect on the geometry. [3] Intramolecular hydrogen bonds can affect chemical reaction rates, such as mediating intramolecular proton transfer on the ground and excited electronic states. [7, 13] They can also affect the aciditiy and basicity of hydrogen

bond donating and accepting sites. [14] Intramolecularly hydrogen bonded molecules are crucial for many biological processes and are becoming increasingly common subjects of drug discovery studies. Tuning the strength or position of an intramolecular hydrogen bond has even been demonstrated to change the potency and permeability of drugs. [15] It is clear that the effects of intramolecular hydrogen bonding are complex and affect the underlying electronic structure of a system in addition to its geometry. This thesis will address the questions of how an intramolecular hydrogen bond affects an electronic absorption spectrum and excited state intramolecular proton transfer.

1.2 Excited State Intramolecular Proton Transfer in Solution

Proton transfer is a ubiquitous chemical reaction, fundamental to many chemical and biological processes. Proton transfer occurs via the transfer of a hydrogen (proton) from a donor atom (D) to an acceptor atom (A). The reaction may occur intramolecularly, in which case the donor and acceptor are connected by a hydrogen bond (D—H$\cdots$A), while intermolecular proton transfers are generally mediated by the solvent. [16] Figure 1.2(a) shows the general photocycle of a tautomerization excited state intramolecular proton transfer (ESIPT) reaction. The enol (E) form of the tautomer is photoexcited from S_0 to S_1 (E*). The intramolecular proton transfer occurs on the femtosecond timescale to the keto tautomer (K*) before decaying radiatively to the ground state keto (K). For a system in which only the enol form of the tautomer exists in the ground state, the reverse proton transfer will occur on an ultrafast timescale as well. [17] ESIPT molecules are characterized by a large Stokes shift, which makes them ideal candidates for use in light emitting applications, such as in stable white light generation and displays. Mixtures of ESIPT molecules or single compounds with halves that emit complementary colors have been shown to be excellent candidates for the develoment of organic light emitting diode (OLED) devices and as "molecular lasers." [17, 18] Their uses in fluorescent probes and for imaging also make them a highly studied class of systems. [19] Chen et al. demonstrated the selective binding and switching off and on of the fluorescence in an ESIPT molecule and proposed its use as a molecular "switch" in

bioanalytical probes. [20]

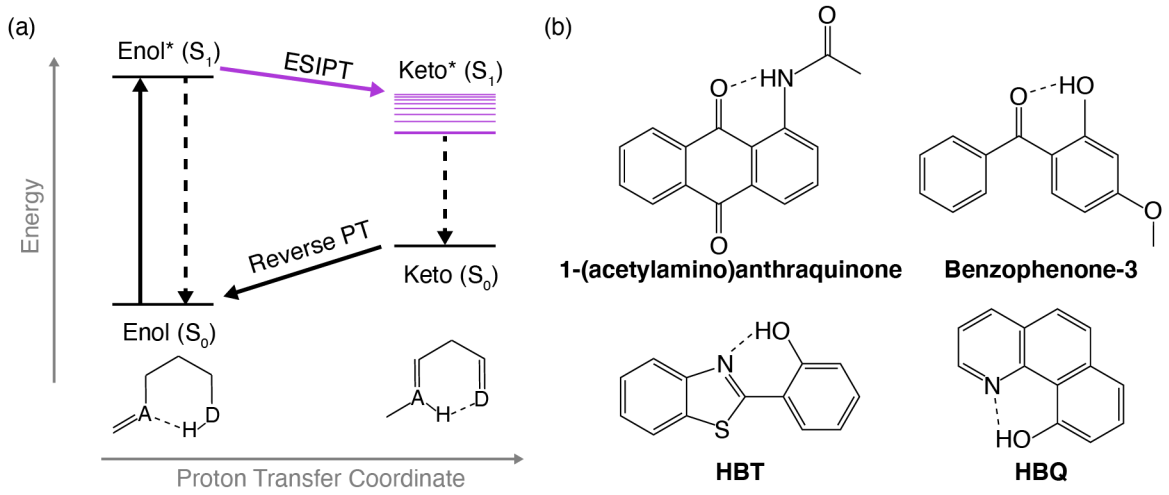

Figure 1.2. ESIPT schematic and examples of common ESIPT fluorophores. a) Following photoexcitation of the enol (E) form of tautomer from the electronic ground state E* ($S_1 \leftarrow S_0$), either emission from the enol (dashed black arrow) or ESIPT (magenta arrow) occurs. Keto emission from K* to K (dashed black arrow) is significantly red-shifted from the enol absorption and emission. A = proton acceptor, and D = proton donor. b) Several common ESIPT fluorophores described in Ref. 19.

Although evidence of the ESIPT in salicylic acid was first observed in 1955 by Weller based on the large Stokes shift in the fluorescence spectra, it was several more decades before the technology required to observe the dynamics of proton transfer reactions in real time was available. [21] The advent of ultrafast laser sources has facilitated the study of ESIPT with now nearly-ubiquitous methods such as pump-probe spectroscopy. In 1986, Elsaesser and Kaiser observed direct evidence of the ESIPT in 2-(2-hydroxyphenyl)-bezothiazole (HBT) with visible pump, infrared probe (transient infrared or tIR) spectroscopy. However, the time resolution of this experiment was still such that the excited state tautomer of HBT was observed, but not the E* state or any intermediate. [22] Ahmed Zewail's research group has made significant contributions to the field of ultrafast spectroscopy and to our understanding of proton transfer reaction mechanisms and dynamics. They have studied proton transfer reactions in real-time with ultrafast spectroscopy, and argued that vibrational modes

delocalized through an entire molecule play an important role in the ESIPT process. [23]

As shown in Fig. 1.2(b), ESIPT reactions are commonly mediated by an intramolecular hydrogen bond between two oxygen atoms or an oxygen and a nitrogen. Depending on the system, either the nitrogen or the oxygen may be the proton donor or acceptor. Electron density is delocalized along a conjugated ring backbone, and the absorption and fluorescence spectra are characterized by a large Stokes shift (≈10,000 cm^{-1}). [19] Fluorophores such as HBT allow the structure to rotate freely around the single bond connecting conjugated rings, while structures like 10-Hydroxybenzo[*h*]quinoline (HBQ) and 1-(acetylamino)anthraquinone have rigid conjugated backbones that do not allow for free rotation. Model systems such as the ones shown in Fig. 1.2(b) are useful for building on our understanding of ESIPT with both experiments and theory or calculations.

1.3 10-Hydroxybenzo[h]quinoline

10-Hydroxybenzo[*h*]quinoline (HBQ) is a model complex that undergoes ultrafast ESIPT upon photoexcitation with near-UV light. [24–26] In the ground state, the proton donor (oxygen) and acceptor (nitrogen) are connected to the hydrogen via a covalent and an intramolecular hydrogen bond, respectively (O—H$\cdots$N). On the excited electronic state, the intramolecular hydrogen bond is predicted to facilitate the ultrafast intramolecular proton transfer from O to N. Based on bond length distances of the O—H and ground state infrared spectra of the OH stretch (ν_{OH}), HBQ has been classified as strongly hydrogen bonding. [11, 24, 27] X-ray crystallography studies found two stable structures present. The bond distances of the O—H or O$\cdots$H bond in each structure was reported to be 1.34 Å and 1.36 Å and the N$\cdots$H (or N—H) was 1.41 Å and 1.45 Å. [27] Although the authors did not specify which structure was which, or why multiple stable structures were observed, these were likely the enol and keto forms of HBQ. However, in solution only the enol form is present in the ground electronic state. DFT geometry optimizations have given bond distances of 1.00 Å and 1.64 Å for O—H and N$\cdots$H in the enol form, respectively, and 2.56 Å for the N$\cdots$O distance. [28] In the same study, the keto ground state optimized geometry

was 1.56 Å for O$\cdots$H, 1.06 Å for N—H, and 2.52 Å for N$\cdots$O. In the excited state, the OH bond lengthens as the NH bond shortens and ESIPT occurs. The strong intramolecular hydrogen bond between O—H$\cdots$N facilitates the ultrafast ESIPT, and the proton transfer in HBQ has been shown to take place on the order of 13 $\pm$5 fs, or within the period of an OH stretching vibration (ν_{OH}). [1, 29] Calculations and experiments have shown that adding substituents to the conjugated backbone of HBQ can tune both the energy and speed of the proton transfer reaction. [6, 30, 31] Several of the studied derivatives are shown in Fig. 1.3, where substitutions of hydrogen atoms at the R_1, R_2, and R_3 sites may consist of combinations of NO_2 and H, or CN and H.

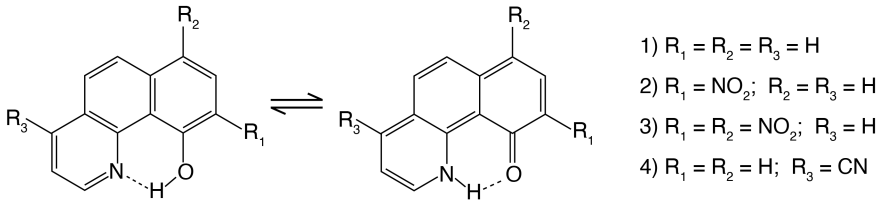

Figure 1.3. 10-Hydroxybenzo[h]quinoline structure and its derivatives.

On the ground electronic state, coherent oscillations after femtosecond excitation of the ν_{OH} vibration have been observed experimentally with a broadband infrared probe and a broadband electronic probe (Ref. 11 and Chapter 2 of this work, respectively). Low-frequency vibrations are known to couple anharmonically to the ν_{OH} stretch in HBQ and other strongly intramolecularly hydrogen bonded systems. [8, 12] However, the impact of these low frequency couplings on the electronic transition ($S_1 \leftarrow S_0$) is still a subject of investigation. Comparatively, the excited state dynamics during and following ESIPT in HBQ have been studied extensively. [1, 6, 26, 30, 32–35] After the discovery of a barrierless ESIPT by Chou et al. [26], coherent oscillations with frequency-dependent dephasing times on the excited state were observed by Takeuchi and Tahara in a visible transient absorption experiment. [35] They estimated the ESIPT to take place in $\leq$30 fs, and concluded that coherence transfer on the excited state was responsible for the long-lived oscillations.

Kim and Joo observed non-Born-Oppenheimer behavior in HBQ, meaning that nuclear and electronic coordinates cannot be separated; they argued that an electronic change on the excited state was induced by nuclear changes, rather than the other way around. [32] This finding emphasizes the importance of considering not only excited state vibrations following photoexcitation, but also the coupling of ground state vibrations to the $S_1 \leftarrow S_0$ excitation. In contrast to the large body of work investigating the coherent oscillations on the excited electronic state, this thesis presents the first study linking ground state vibrations to the electronic transition in HBQ. Developing a deeper understanding of the motions that drive and affect ESIPT requires studies that link the nuclear and electronic motions prior to proton transfer.

HBQ is useful as a model complex to help us understand both strong intramolecular hydrogen bonding and the ESIPT process in larger systems as well. As a small organic molecule, modeling both processes is simpler than in large biological systems such as proteins or DNA. The single proton donor and acceptor sites and individual hydrogen bond are ideal for pinpointing the origin of spectral signatures and phenomena in complex experiments. Understanding the motions that drive proton transfer and electronic excitation, such as low frequency skeletal deformations or high frequency OH stretches, starts with smaller systems before it can be translated to larger biological and technological questions. Finally, the ability to synthetically tune the proton transfer allows for control over experimental conditions, the gradual addition of degrees of freedom, and translating the assignment of spectral signatures to larger systems and similarly short timescales.

1.4 Multidimensional Spectroscopy

Time-resolved and multidimensional spectroscopies enable the observation of coupled electronic and/or nuclear degrees of freedom on ultrafast timescales. One of the most widely used third-order nonlinear spectroscopy methods is pump-probe spectroscopy. The initial pulse (pump) excites a population or coherence, and the change in transmitted intensity of the second pulse (probe) caused by the pump is monitored after the sample. Figure 1.4(a)

shows a general pulse sequence of a third-order experiment. In a pump-probe experiment, the time delay between the electric fields of the pump pulse (E_1 and E_2) is $\tau_1 = 0$, and the delay between pump and probe pulses, τ_2, is scanned or stepped incrementally to monitor the time evolution of populations or coherences excited by the pump. In a 2D experiment, an additional delay (τ_1) between two identical pump pulses is introduced. A Fourier transform over τ_1 provides excitation frequency resolution and allows the direct correlation of excitation with detection frequencies, which is particularly useful when multiple or broad transitions are excited coherently by the pump. Figure 1.4(b) shows a pump-probe experimental geometry. The directions of the wavevectors for the pump pulses ($\vec{k}_{vib}$) cancel one another, so that the wavevectors of the probe and signal ($\vec{k}_{elec}$ and $\vec{k}_{sig}$) point in the same direction. The evolution of these optical spectroscopies has spanned many decades, starting with single- and multi-color pump-probe experiments such as transient absorption (TA), infrared pump-probe, and transient infrared (tIR) spectroscopy. Coherent multidimensional spectroscopies such as two-dimensional terahertz (2D THz), two-dimensional infrared (2D IR), and two-dimensional electronic spectroscopy (2D ES) have accessed valuable information on chemically and biologically relevant timescales. [36–40]

2D THz, 2D IR, and 2D ES allow the observation of signals that shift frequencies along pump and/or probe wavelengths. These off-diagonal signals, known as cross-peaks, contain information about the coupling between various different degrees of freedom, such as nuclear motion like a vibration, and electronic motion such as an electron transfer or electronic excitation. Figure 1.4(c) shows the types of multidimensional spectroscopy experiments that have been performed in recent decades. It is not a comprehensive list, but rather a representative example of the frequency ranges that have been accessed in 2D spectroscopy. 2D THz, IR, and ES experiments access both on-diagonal and cross-peaks, and predominate the examples shown in Fig. 1.4(c). On-diagonal peaks are significantly stronger than cross-peaks, and experiments using the same pump and probe wavelengths are generally more straightforward to build and perform due to their stronger signals. However, as the stability and power of ultrashort broadband laser sources have improved, access to the information-

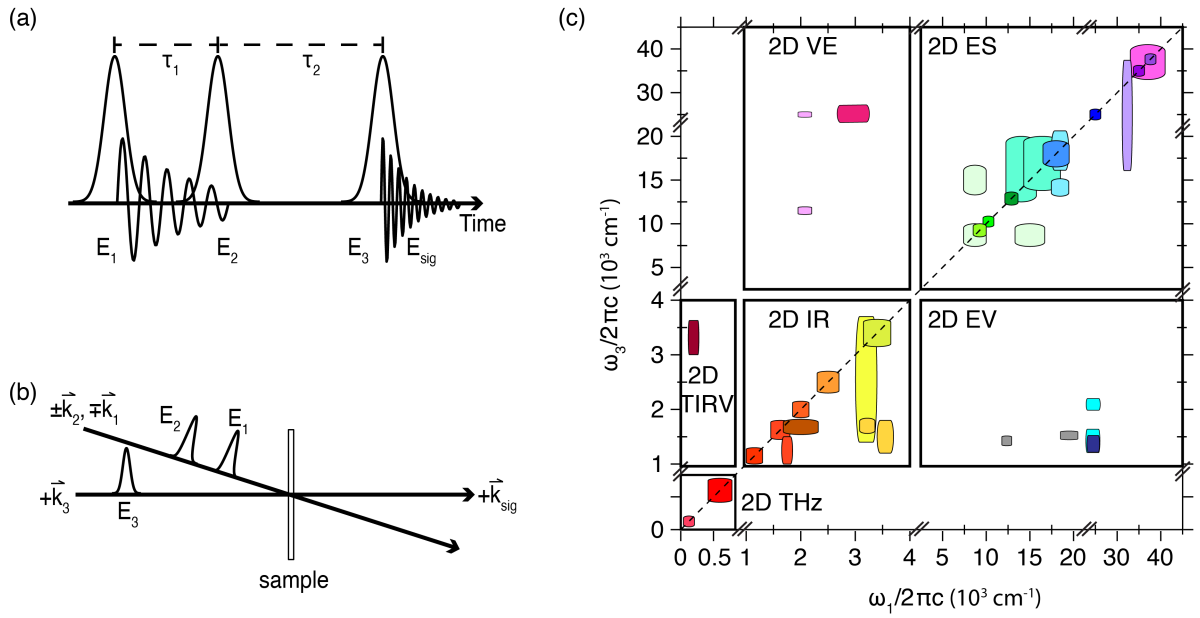

Figure 1.4. a) Third-order spectroscopy pulse sequence. b) Pump-probe geometry. Pump pulses propagate collinearly and overlap at the sample with the probe pulse. The signal co-propagates with the probe until detection. c) Map of multidimensional spectroscopy experiment frequency ranges from 2000–2024. Colored boxes represent the frequency ranges accessed by multidimensional spectroscopy experiments. Updated from reference 41 with permission of corresponding author.

rich cross peaks in multicolor spectroscopies has increased.

Many experiments that mix infrared and visible or ultraviolet wavelengths have been developed over the last several decades, observing both coherent and incoherent (population) dynamics. Some directly access vibronic coupling, while others incorporate visible pulses into infrared spectroscopy experiments to selectively enhance signals of interest. Detection of an electronic absorption following an infrared pump pulse has also been demonstrated as a useful method for several applications. Vibrational pump - electronic probe experiments were performed by Cheatum et al. to determine the vibrational population relaxation timescales of Franck-Condon active modes in a molecular liquid. [42] Rather than using a vibrationally-resonant probe pulse (i.e. an IR pump-probe experiment), the electronically-

resonant probe had the distinct advantage of its sensitivity to probing only Franck-Condon active vibrations. Thus, signal from non-Franck-Condon active vibrations was not observed which simplified the detected signal. A similar infrared pump - visible probe experiment from the Tahara group investigated the role of mechanical versus electrical anharmonicity in the electronic transition of a strongly hydrogen bonded compound in solution. [43] Rather than solely determining vibrational population lifetimes, Ishii and Tahara implemented a Fourier transform over the pump-probe delay to resolve a coherent low-frequency vibration modulating the electronic signal. This experiment and our analog experiment are discussed in greater detail in Chapter 2. The four and six wave mixing spectroscopies developed by John Wright's group also accessed vibronic coupling with a combination of infrared and visible wavelengths. [44] Doubly vibrationally enhanced four wave mixing (DOVE-FWM) utilizes electronically-detected raman and infrared absorption processes. Selectively enhanced combination bands are able to enhance and distinguish between inter- and intramolecular signals and components of an isotopic mixture.

More recently, vibrationally promoted electronic resonance (VIPER) spectroscopy, developed by the Bredenbeck group, has made use of long electronic excited state lifetimes to extend the lifetime of vibrational signals. [45] A visible pulse resonant with the $|g,1\rangle$ to $|e,0'\rangle$ transition but too low in energy to access the $|g,0\rangle$ to $|e,0'\rangle$ transition is inserted between infrared pump and infrared probe pulses. The notation of g and e refer to the ground and excited electronic states, respectively. 0 and 1 refer to vibrational levels in the ground electronic state, while 0' and 1' refer to vibrational energy levels in the excited electronic state. The vibrational population from the excited $|g,1\rangle$ is encoded in the long-lived electronic excited state ($|e,0'\rangle$), and the time-dependent dynamics of a long-timescale process such as chemical exchange may be tracked by monitoring the removal of population from $\nu = 1$ without the restriction of a comparatively short vibrational lifetime. The Bakulin group recently demonstrated coherent control of an optoelectronic device by resonantly exciting vibrations with two infrared pump pulses and detecting an electronic photocurrent signal in an experiment called "PC-VIPER." [46] Fluorescence encoded infrared spectroscopy (FEIR) also utilizes

sum frequency generation of an infrared pulse and a visible pulse. Rather than detecting excited state vibrations, the fluorescence from the excited electronic state is detected. This measurement can be made sensitive to single molecules in solution, avoiding the need for an ensemble average. A second infrared pump pulse can also be added to obtain frequency resolution of the excitation axis. [47–50] Both VIPER and FEIR require a molecule to have some amount of vibronic coupling and Franck-Condon active vibrations of interest in order to observe the transition from $|g,1\rangle$ to $|e,0'\rangle$.

Two multidimensional vibronic spectroscopies, called two-dimensional electronic-vibrational (2D EV) and vibrational-electronic (2D VE) spectroscopy have also been developed recently. [41, 51–58] 2D EV probes the coupling of vibrations on the excited electronic state to an electronic transition ($S_1 \leftarrow S_0$) such as a proton or electron transfer. 2D VE probes the coupling of the ground state vibrations to the electronic transition. The selection rules for vibronic spectroscopies are briefly discussed in Chapter 2.3, and are described in greater detail in Refs. 52, 57–59. Both inherently access vibronic transitions and couplings between nuclear and electronic degrees of freedom and may be used with polarization-selectivity to enhance or suppress orientation-dependent signals or determine relative orientations of transition dipole moments of molecules in solution. As such, they are powerful methods for studying complex processes such as proton transfer and hydrogen bonding, which involve intimately coupled structural and electronic fluctuations. This thesis discusses recent developments and improvements to the implementation of 2D VE spectroscopy, and the use of 1D and 2D VE spectroscopy to observe low- and high-frequency modes coupled to the electronic transition in HBQ.

1.5 Tracking Hydrogen Bonding and Proton Transfer with X-ray Spectroscopy

X-ray absorption spectroscopy (XAS) offers an element-specific method to investigate electronic structure. Figure 1.5(a) demonstrates the excitation energies for different X-ray absorption processes. The excitation of a core electron to a valence energy level requires much more energy than a valence excitation. An excitation from quantum number n = 1 (1s or-

bital) into the valence is described as a "K-edge" excitation. An excitation from n = 2 (2s and 2p orbitals) is described as the "L-edge," and from n = 3 (3s, 3p, and 3d orbitals) is called the "M-edge." An X-ray absorption spectroscopy experiment is performed by scanning a range of X-ray wavelengths with a monochromator and monitoring the absorption of the X-rays at the sample of interest. Single atoms of each element have well-defined and recorded ionization energies of electrons from their core orbitals. When bonded to other atoms in a molecule, the pre-edge features — transitions into unoccupied valence orbitals — are spectral signatures that offer a rich description of the local electronic environment around the atom whose core electron was excited. Figure 1.5(b) shows a cartoon energy diagram of three pre-edge features. The corresponding cartoon absorption spectrum is shown in Fig. 1.5(c). Valence orbitals are delocalized throughout a molecule compared to the highly localized atomic orbitals, but XAS provides a useful connection between the two. The energies and intensities of the pre-edge absorption features are sensitive to structural fluctuations in the molecule, and report on changes in atom position and bonding environment. For example, oxygen K-edge XAS can differentiate between various oxygen functional groups in small organic molecules. [33]

X-ray spectroscopy has proved extremely useful in connecting structural fluctuations with a molecule's electronic environment. One such structural fluctuation is in hydrogen bonding and proton transfer. Because of its sensitivity to the local electronic and structural environment of the probed atom, soft X-ray spectroscopy is ideal for tracking processes in solution such as these. XAS experiments have shown evidence of proton transfers, and time-resolved computational studies have tracked them. [28, 60–62] Van Kuiken et al. describe the use of transient sulfur K-edge XAS to track the evolution of two excited state species in 2-thiopyridone (2-TP), another small organic molecule. Using a combination of computational and experimental transient XAS (t-XAS), they determined that some of the excited species of 2-TP converts to the tautomer species, 2-mercaptopyridine, before returning to the ground state. [60] This study successfully observed the presence of the tautomer species, but did not have the time resolution to observe the tautomer's formation and determine the

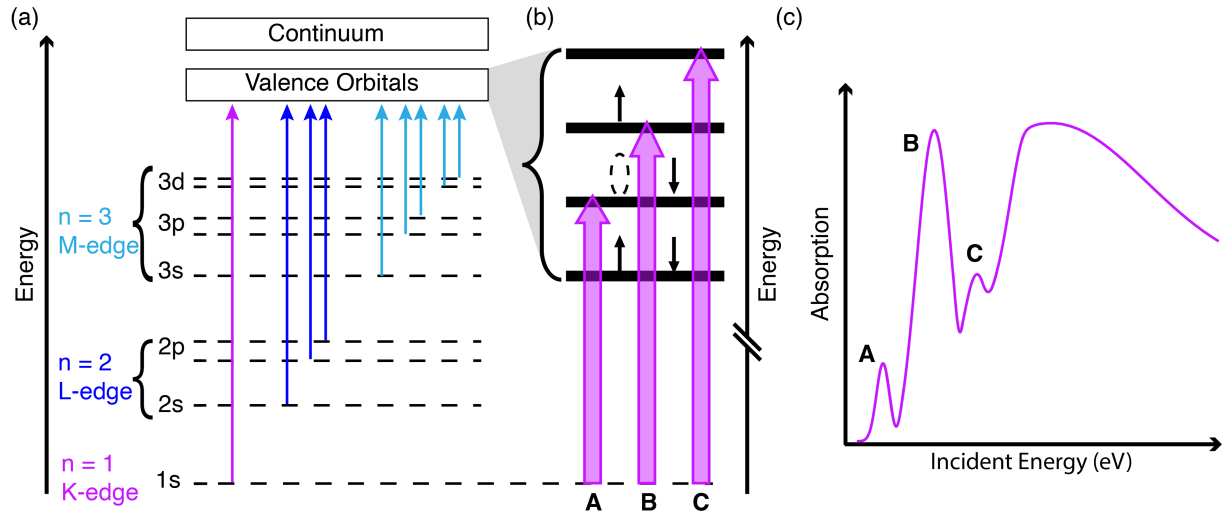

Figure 1.5. X-ray absorption spectroscopy (XAS) energy diagrams. Energies not to scale. a) K-edge, L-edge, and M-edge XAS excite electrons from core levels with quantum numbers corresponding to n = 1, n = 2, and n = 3, resepctively. b) The lowest energy transitions in K-edge XAS are electrons excited from the 1s orbital into partially occupied or unoccupied valence orbitals. Transitions to unoccupied valence orbitals are labeled as A, B, and C and correspond to the labeled features in (c).

pathways involved. Recent innovations in X-ray free electron lasers (XFELS) have resulted in improvements to time- and frequency-resolution that will enable the experimental observation of ultrafast processes, and help determine relaxation pathways like those mentioned above. Later transient nitrogen K-edge XAS experiments on 2-TP successfully identified the excited state proton transfer pathway, although it remained inconclusive if the mechanism of the proton transfer was inter- or intramolecular. [61] Rather than a photoexcitation-induced proton transfer, Stevens et al. observed clear chemical shifts in the N K-edge XAS spectrum following a temperature change-induced intermolecular proton transfer from squaric acid to 4,4'-Bipyridine. [62]

X-ray studies have also been used to monitor inter- and intramolecular hydrogen bonding in solution. [63–72] Nitrogen K-edge XAS was shown to be an accurate probe of systems such as amines in aqueous solution and in polar organic solvents. [63–66] The differences in

intermolecular hydrogen bonding of solute with the solvent were revealed with soft X-ray spectroscopy, which is sensitive to different protonation states at nitrogen sites. [67] N K-edge XAS is a particularly important probe for hydrogen bonding environments in amino acids such as glycine and diglycine. [69] Oxygen K-edge X-ray spectroscopy has also been proven sensitive to hydrogen bonding environments, and monitoring the O K-edge intensity allowed for the determination of the order or disorder in a hydrogen bonding environment in alcohol-water mixtures. [71] Resolving emission wavelengths at each absorption wavelength with resonant inelastic X-ray scattering (RIXS) experiments at the O K-edge showed modulations of the hydrogen bond network in liquid water and was even as sensitive to hydrogen bond strength as infrared spectroscopy. [70, 72]

X-ray spectroscopy is sensitive to local electronic structure and reports on both structural and electronic fluctuations in molecules. When paired with calculations, it is possible to monitor hydrogen bonding and proton transfer environments, and the advent of ultrafast X-ray free electron laser sources has paved the way for the experimental use of time-resolved X-ray spectroscopy to study and track ultrafast chemical processes. The benefit of element-specificity allows for complementary investigation at multiple sites in a system, which makes it well-suited for investigating a model proton transfer system such as HBQ, which has distinct proton donor and acceptor atoms. Chapter 3 of this dissertation describes our computational study using multicolor excited-state XAS calculations to observe coherent atomic motions coupled to the local electronic environments of both the proton donor and acceptor sites in HBQ. [28]

1.6 Dissertation Overview

The first part of this dissertation, Chapters 2 and 3, describes the use of multicolor time-resolved spectroscopy to investigate the role of vibrations in the electronic ground and excited states of 10-Hydroxybenzo[h]quinoline, a model complex which has a strong intramolecular hydrogen bond that facilitates an ultrafast ESIPT. On the electronic ground state, 1D and 2D VE spectroscopy allow the observation of both low and high frequency modes which couple

to the red edge of the electronic excitation, $S_1 \leftarrow S_0$. By linking ground state vibrations to the electronic excitation we are able to determine which atomic motions in the strongly hydrogen bonded complex may influence the electronic transition, and eventually the proton transfer dynamics. On the electronic excited state, multicolor transient X-ray absorption spectroscopy TD-DFT calculations provide insight to the local electronic environment around the proton (or hydrogen bond) donor and acceptor. During and following the ESIPT, there is a modulation in the X-ray absorption energy at both proton donor and acceptor sites because the local electronic environment is sensitive to the strucutral fluctuations in the K* tautomer of HBQ as it relaxes through a manifold of vibrationally excited states. These computational results show that transient X-ray spectroscopy can serve as an accurate local electronic probe for tracking ultrafast photochemical reactions such as excited state intramolecular proton transfer, and have assisted the group in winning beamtime to perform the proposed experiments.

The second part of this dissertation, Chapter 4, will discuss the implementation and design of a two-dimensional vibrational-electronic spectrometer. A great deal of work goes into collecting experimental spectra in a nonlinear spectroscopy lab, and this work is made less challenging when complex experimental procedures and quirks of the lab are clearly communicated between lab members. Although a lab notebook is typically sufficient to act as a record of this information, the purpose of a detailed experimental chapter is to serve as both a manual and a well-organized and compiled reference for 2D VE experiments in the future. We have found 2D VE experiments to be particularly challenging to perform for a number of reasons, which is why as much detail as possible is included. The final part of Chapter 4 discusses 2D VE spectra of cyanoferrates in solution and some of the surprising results that we have encountered with the use of various solvents. Data presented here are not included in any current published works, but nevertheless are important to discuss and keep record of for future experimental endeavors. The last part of this dissertation, Chapter 5, offers some final perspective on the conclusions and future outlook for these projects.

BIBLIOGRAPHY

[1] C. H. Kim and T. Joo, "Coherent Excited State Intramolecular Proton Transfer Probed by Time-Resolved Fluorescence," *Physical Chemistry Chemical Physics*, vol. 11, no. 44, pp. 10266–10269, 2009.

[2] H. Ishikita and K. Saito, "Proton transfer reactions and hydrogen-bond networks in protein environments," *Journal of The Royal Society Interface*, vol. 11, p. 20130518, Feb. 2014.

[3] S. Horowitz and R. C. Trievel, "Carbon-Oxygen Hydrogen Bonding in Biological Structure and Function," *Journal of Biological Chemistry*, vol. 287, pp. 41576–41582, Dec. 2012.

[4] E. T. Kool, "Hydrogen Bonding, Base Stacking, and Steric Effects in DNA Replication," *Annual Review of Biophysics*, vol. 30, pp. 1–22, Jun. 2001.

[5] G. Zhao and K. Han, "Effects of Hydrogen Bonding on Tuning Photochemistry: Concerted Hydrogen-Bond Strengthening and Weakening," *ChemPhysChem*, vol. 9, pp. 1842–1846, Sep. 2008.

[6] S. Hristova, G. Dobrikov, F. S. Kamounah, S. Kawauchi, P. E. Hansen, V. Deneva, D. Nedeltcheva, and L. Antonov, "10-Hydroxybenzo[*h*]quinoline: Switching Between Single- and Double-Well Proton Transfer Through Structural Modifications," *RSC Advances*, vol. 5, pp. 102495–102507, 2015.

[7] G.-J. Zhao and K.-L. Han, "Hydrogen Bonding in the Electronic Excited State," *Accounts of Chemical Research*, vol. 45, pp. 404–413, Mar. 2012.

[8] D. Madsen, J. Stenger, J. Dreyer, E. T. J. Nibbering, P. Hamm, and T. Elsaesser, "Coherent vibrational ground-state dynamics of an intramolecular hydrogen bond," *Chemical Physics Letters*, vol. 341, pp. 56–62, Jun. 2001.

[9] C. J. Fecko, J. D. Eaves, J. J. Loparo, A. Tokmakoff, and P. L. Geissler, "Ultrafast Hydrogen-Bond Dynamics in the Infrared Spectroscopy of Water," *Science*, vol. 301, pp. 1698–1702, Sep. 2003.

[10] M. Grechko, T. Hasegawa, F. D'Angelo, H. Ito, D. Turchinovich, Y. Nagata, and M. Bonn, "Coupling between intra- and intermolecular motions in liquid water revealed by two-dimensional terahertz-infrared-visible spectroscopy," *Nature Communications*, vol. 9, pp. 1–8, Feb. 2018.

[11] M. Balasubramanian, A. Reynolds, T. J. Blair, and M. Khalil, "Probing Ultrafast Vibrational Dynamics of Intramolecular Hydrogen Bonds with Broadband Infrared Pump-Probe Spectroscopy," *Chemical Physics*, vol. 519, pp. 38–44, Mar. 2019.

[12] E. T. J. Nibbering and T. Elsaesser, "Ultrafast Vibrational Dynamics of Hydrogen Bonds in the Condensed Phase," *Chemical Reviews*, vol. 104, pp. 1887–1914, Apr. 2004.

[13] H. P. Upadhyaya, "Ground-state intramolecular proton transfer and observation of high energy tautomer in 1,4-Dihydroxyanthraquinone," *Journal of Molecular Structure*, vol. 1232, p. 130050, May 2021.

[14] F. T. T. Huque and J. A. Platts, "The effect of intramolecular interactions on hydrogen bond acidity," *Organic & Biomolecular Chemistry*, vol. 1, pp. 1419–1424, Apr. 2003.

[15] G. Caron, J. Kihlberg, and G. Ermondi, "Intramolecular hydrogen bonding: An opportunity for improved design in medicinal chemistry," *Medicinal Research Reviews*, vol. 39, no. 5, pp. 1707–1729, 2019.

[16] T. Kumpulainen, B. Lang, A. Rosspeintner, and E. Vauthey, "Ultrafast Elementary Photochemical Processes of Organic Molecules in Liquid Solution," *Chemical Reviews*, vol. 117, pp. 10826–10939, Aug. 2017.

[17] J. E. Kwon and S. Y. Park, "Advanced Organic Optoelectronic Materials: Harnessing Excited-State Intramolecular Proton Transfer (ESIPT) Process," *Advanced Materials*, vol. 23, pp. 3615–3642, 2011.

[18] S. Park, E. K. Ji, H. K. Se, J. Seo, K. Chung, S. Y. Park, D. J. Jang, B. M. Medina, J. Gierschner, and Y. P. Soo, "A White-Light-Emitting Molecule: Frustrated Energy Transfer Between Constituent Emitting Centers," *The Journal of the American Chemical Society*, vol. 131, pp. 14043–14049, 2009.

[19] A. C. Sedgwick, L. Wu, H. H. Han, S. D. Bull, X. P. He, T. D. James, J. L. Sessler, B. Z. Tang, H. Tian, and J. Yoon, "Excited-State Intramolecular Proton-Transfer (ESIPT) Based Fluorescence Sensors and Imaging Agents," *Chemical Society Reviews*, vol. 47, pp. 8842–8880, 2018.

[20] W. H. Chen, Y. Xing, and Y. Pang, "A Highly Selective Pyrophosphate Sensor Based on ESIPT Turn-On in Water," *Organic Letters*, vol. 13, no. 6, pp. 1362–1365, 2011.

[21] A. Weller, "Über die Fluoreszenzder Salizylsäure und verwandter Verbindungen.," *Die Naturwissenschaften*, vol. 42, pp. 176–177, 1955.

[22] T. Elsaesser and W. Kaiser, "Visible and infrared spectroscopy of intramolecular proton transfer using picosecond laser pulses," *Chemical Physics Letters*, vol. 128, pp. 231–237, Jul. 1986.

[23] A. Douhal, F. Lahmani, and A. H. Zewail, "Proton-transfer reaction dynamics," *Chemical Physics*, vol. 207, pp. 477–498, Jul. 1996.

[24] M. L. Martinez, W. C. Cooper, and P.-T. Chou, "A Novel Excited-State Intramolecular Proton Transfer Molecule, 10-Hydroxybenzo[*h*]quinoline," *Chemical Physics Letters*, vol. 193, no. 1-3, pp. 151–154, 1992.

[25] P.-T. Chou and M. L. Martinez, "Photooxygenation of 3-hydroxyflavone and molecular design of the radiation-hard scintillator based on the excited-state proton transfer," *Radiation Physics and Chemistry*, vol. 41, no. 1/2, pp. 373–378, 1993.

[26] P.-T. Chou, Y.-C. Chen, W.-S. Yu, Y.-H. Chou, C.-Y. Wei, and Y.-M. Cheng, "Excited-State Intramolecular Proton Transfer in 10-Hydroxybenzo[*h*]quinoline," *The Journal of Physical Chemistry A*, vol. 105, pp. 1731–1740, Mar. 2001.

[27] M. Kubicki, T. Borowiak, and W. Z. Antkowiak, "10-Hydroxybenzo[h]quinoline," *Acta Crystallographica Section C*, vol. 51, pp. 1173–1175, 1995.

[28] C. M. Loe, C. Liekhus-Schmaltz, N. Govind, and M. Khalil, "Spectral signatures of ultrafast excited-state intramolecular proton transfer from computational multi-edge transient x-ray absorption spectroscopy," *The Journal of Physical Chemistry Letters*, vol. 12, pp. 9840–9847, Oct. 2021.

[29] M. Zhou, J. Zhao, Y. Cui, Q. Wang, Y. Dai, P. Song, and L. Xia, "Theoretical Study on the Excited-State Intramolecular Proton-Transfer Reaction of 10-Hydroxybenzo[*h*]quinoline in Methanol and Cyclohexane," *Journal of Luminescence*, vol. 161, pp. 1–6, May 2015.

[30] H. Marciniak, S. Hristova, V. Deneva, F. S. Kamounah, P. E. Hansen, S. Lochbrunner, and L. Antonov, "Dynamics of Excited State Proton Transfer in Nitro Substituted 10-Hydroxybenzo[*h*]quinolines," *Physical Chemistry Chemical Physics*, vol. 19, no. 39, pp. 26621–26629, 2017.

[31] S. Chai and S.-L. Cong, "Excited State Intramolecular Proton Transfer and Substituent Effect of 10-Hydroxybenzo[h]quinoline: A Time-Dependent Density Functional Theory Study," *Computational and Theoretical Chemistry*, vol. 1034, pp. 80–84, 2014.

[32] J. W. Kim, C. H. Kim, C. Burger, M. Park, M. F. Kling, D. E. Kim, and T. Joo, "Non-Born–Oppenheimer Molecular Dynamics Observed by Coherent Nuclear Wave Packets," *The Journal of Physical Chemistry Letters*, vol. 11, pp. 755–761, 2020.

[33] K. Kim, P. Zhu, N. Li, X. Ma, and Y. Chen, "Characterization of oxygen containing functional groups on carbon materials with oxygen K-edge X-ray absorption near edge structure spectroscopy," *Carbon*, vol. 49, pp. 1745–1751, Apr. 2011.

[34] W. Chansen, R. Salaeh, C. Prommin, K. Kerdpol, R. Daengngern, and N. Kungwan, "Theoretical Study on Influence of Geometry Controlling Over the Excited-State Intramolecular Proton Transfer of 10-Hydroxybenzo[h]quinoline and its Derivatives," *Computational and Theoretical Chemistry*, vol. 1113, pp. 42–51, 2017.

[35] S. Takeuchi and T. Tahara, "Coherent Nuclear Wavepacket Motions in Ultrafast Excited-State Intramolecular Proton Transfer: Sub-30-fs Resolved Pump–Probe Absorption Spectroscopy of 10-Hydroxybenzo[h]quinoline in Solution," *The Journal of Physical Chemistry A*, vol. 109, pp. 10199–10207, Nov. 2005.

[36] W. Kuehn, K. Reimann, M. Woerner, T. Elsaesser, R. Hey, and U. Schade, "Strong Correlation of Electronic and Lattice Excitations in GaAs/AlGaAs Semiconductor Quantum Wells Revealed by Two-Dimensional Terahertz Spectroscopy," *Physical Review Letters*, vol. 107, p. 067401, 2011.

[37] P. Hamm, M. Lim, and R. M. Hochstrasser, "Structure of the Amide I Band of Peptides Measured by Femtosecond Nonlinear-Infrared Spectroscopy," *The Journal of Physical Chemistry B*, vol. 102, pp. 6123–6138, 1998.

[38] M. C. Asplund, M. T. Zanni, and R. M. Hochstrasser, "Two-dimensional infrared spectroscopy of peptides by phase-controlled femtosecond vibrational photon echoes," *Proceedings of the National Academy of Sciences*, vol. 97, pp. 8219–8224, Jul. 2000.

[39] O. Golonzka, M. Khalil, N. Demirdöven, and A. Tokmakoff, "Vibrational Anharmonicities Revealed by Coherent Two-Dimensional Infrared Spectroscopy," *Physical Review Letters*, vol. 86, pp. 2154–2157, Mar. 2001.

[40] J. D. Hybl, A. W. Albrecht, S. M. Gallagher Faeder, and D. M. Jonas, "Two-dimensional electronic spectroscopy," *Chemical Physics Letters*, vol. 297, no. 3-4, pp. 307–313, 1998.

[41] T. L. Courtney, Z. W. Fox, K. M. Slenkamp, and M. Khalil, "Two-dimensional vibrational-electronic spectroscopy," *The Journal of Chemical Physics*, vol. 143, p. 154201, Oct. 2015.

[42] C. M. Cheatum, M. M. Hecksher, D. Bingemann, and F. F. Crim, "CH2I2 fundamental vibrational relaxation in solution studied by transient electronic absorption spectroscopy," *The Journal of Chemical Physics*, vol. 115, no. 15, 2001.

[43] K. Ishii, S. Takeuchi, and T. Tahara, "Infrared-induced coherent vibration of a hydrogen-bonded system: Effects of mechanical and electrical anharmonic couplings," *The Journal of Chemical Physics*, vol. 131, p. 044512, Jul. 2009.

[44] W. Zhao and J. C. Wright, "Doubly Vibrationally Enhanced Four Wave Mixing: The Optical Analog to 2D NMR," *Physical Review Letters*, vol. 84, pp. 1411–1414, Feb. 2000.

[45] L. J. van Wilderen, A. T. Messmer, and J. Bredenbeck, "Mixed IR/Vis two-dimensional spectroscopy: Chemical exchange beyond the vibrational lifetime and sub-ensemble selective photochemistry," *Angewandte Chemie International Edition*, vol. 53, pp. 2667–2672, 2014.

[46] N. P. Gallop, D. R. Maslennikov, N. Mondal, K. P. Goetz, Z. Dai, A. M. Schankler, W. Sung, S. Nihonyanagi, T. Tahara, M. I. Bodnarchuk, M. V. Kovalenko, Y. Vaynzof, A. M. Rappe, and A. A. Bakulin, "Ultrafast vibrational control of organohalide perovskite optoelectronic devices using vibrationally promoted electronic resonance," *Nature Materials*, vol. 23, pp. 88–94, Jan. 2024.

[47] J. N. Mastron and A. Tokmakoff, "Two-Photon-Excited Fluorescence-Encoded Infrared Spectroscopy," *The Journal of Physical Chemistry A*, vol. 120, pp. 9178–9187, Nov. 2016.

[48] J. N. Mastron and A. Tokmakoff, "Fourier Transform Fluorescence - Encoded Infrared Spectroscopy," *The Journal of Physical Chemistry A*, vol. 122, pp. 554–562, Jan. 2018.

[49] L. Whaley-Mayda, S. B. Penwell, and A. Tokmakoff, "Fluorescence-Encoded Infrared Spectroscopy: Ultrafast Vibrational Spectroscopy on Small Ensembles of Molecules in Solution," *The Journal of Physical Chemistry Letters*, vol. 10, pp. 1967–1972, Apr. 2019.

[50] A. Guha, L. Whaley-Mayda, S. Y. Lee, and A. Tokmakoff, "Molecular factors determining brightness in fluorescence-encoded infrared vibrational spectroscopy," *The Journal of Chemical Physics*, vol. 160, p. 104202, Mar. 2024.

[51] T. A. Oliver, N. H. Lewis, and G. R. Fleming, "Correlating the motion of electrons and nuclei with two-dimensional electronic-vibrational spectroscopy," *Proceedings of the National Academy of Sciences*, vol. 111, pp. 10061–10066, Jul. 2014.

[52] T. L. Courtney, Z. W. Fox, L. Estergreen, and M. Khalil, "Measuring Coherently Coupled Intramolecular Vibrational and Charge-Transfer Dynamics with Two-Dimensional Vibrational-Electronic Spectroscopy," *The Journal of Physical Chemistry Letters*, vol. 6, pp. 1286–1292, Apr. 2015.

[53] Z. W. Fox, T. J. Blair, R. B. Weakly, T. L. Courtney, and M. Khalil, "Implementation of Continuous Fast Scanning Detection in Femtosecond Fourier-Transform Two-Dimensional Vibrational-Electronic Spectroscopy to Decrease Data Acquisition Time," *Review of Scientific Instruments*, vol. 89, pp. 113104–1–7, Nov. 2018.

[54] J. D. Gaynor, A. Petrone, X. Li, and M. Khalil, "Mapping vibronic couplings in a solar cell dye with polarization-selective two-dimensional electronic-vibrational spectroscopy," *The Journal of Physical Chemistry Letters*, vol. 9, pp. 6289–6295, 11 2018.

[55] J. D. Gaynor, J. Sandwisch, and M. Khalil, "Vibronic coherence evolution in multidimensional ultrafast photochemical processes," *Nature Communications*, vol. 10, pp. 1–9, 2019.

[56] Z. W. Fox, T. J. Blair, and M. Khalil, "Determining the Orientation and Vibronic Couplings between Electronic and Vibrational Coordinates with Polarization-Selective Two-Dimensional Vibrational-Electronic Spectroscopy," *The Journal of Physical Chemistry Letters*, vol. 11, pp. 1558–1563, 2020.

[57] J. D. Gaynor, R. B. Weakly, and M. Khalil, "Multimode two-dimensional vibronic spectroscopy. I. Orientational response and polarization-selectivity," *The Journal of Chemical Physics*, vol. 154, p. 184201, 2021.

[58] R. B. Weakly, J. D. Gaynor, and M. Khalil, "Multimode two-dimensional vibronic spectroscopy. II. Simulating and extracting vibronic coupling parameters from polarization-selective spectra," *The Journal of Chemical Physics*, vol. 154, p. 184202, 2021.

[59] J. D. Gaynor and M. Khalil, "Signatures of vibronic coupling in two-dimensional electronic-vibrational and vibrational-electronic spectroscopies," *TheJournal of Chemical Physics*, vol. 147, p. 094202, 2017.

[60] B. E. Van Kuiken, M. R. Ross, M. L. Strader, A. A. Cordones, H. Cho, J. H. Lee, R. W. Schoenlein, and M. Khalil, "Picosecond sulfur K-edge X-ray absorption spectroscopy with applications to excited state proton transfer," *Structural Dynamics*, vol. 4, p. 044021, 2017.

[61] S. Eckert, J. Norell, R. M. Jay, M. Fondell, R. Mitzner, M. Odelius, and A. Föhlisch, "T1 Population as the Driver of Excited-State Proton-Transfer in 2-Thiopyridone," *Chemistry - A European Journal*, vol. 25, pp. 1733–1739, 2019.

[62] J. S. Stevens, M. Walczak, C. Jaye, and D. A. Fischer, "In Situ Solid-State Reactions Monitored by X-ray Absorption Spectroscopy: Temperature-Induced Proton Transfer Leads to Chemical Shifts," *Chemistry - A European Journal*, vol. 22, pp. 15600–15604, Oct. 2016.

[63] M. Ekimova, W. Quevedo, Ł. Szyc, M. Iannuzzi, P. Wernet, M. Odelius, and E. T. Nibbering, "Aqueous Solvation of Ammonia and Ammonium: Probing Hydrogen Bond Motifs with FT-IR and Soft X-Ray Spectroscopy," *Journal of the American Chemical Society*, vol. 139, pp. 12773–12783, 2017.

[64] M. Ekimova, M. Kubin, M. Ochmann, J. Ludwig, N. Huse, P. Wernet, M. Odelius, and E. T. Nibbering, "Soft X-Ray Spectroscopy of the Amine Group: Hydrogen Bond Motifs in Alkylamine/Alkylammonium Acid–Base Pairs," *The Journal of Physical Chemistry B*, vol. 122, pp. 7737–7746, Aug. 2018.

[65] M. Prémont-Schwarz, S. Schreck, M. Iannuzzi, E. T. Nibbering, M. Odelius, and P. Wernet, "Correlating Infrared and X-Ray Absorption Energies for Molecular-Level Insight into Hydrogen Bond Making and Breaking in Solution," *The Journal of Physical Chemistry B*, vol. 119, pp. 8115–8124, 2015.

[66] L. Weinhardt, E. Ertan, M. Iannuzzi, M. Weigand, O. Fuchs, M. Bär, M. Blum, J. D. Denlinger, W. Yang, E. Umbach, M. Odelius, and C. Heske, "Probing hydrogen bonding orbitals: resonant inelastic soft X-ray scattering of aqueous NH3," *Physical Chemistry Chemical Physics*, vol. 17, pp. 27145–27153, Oct. 2015.

[67] S. Eckert, P. S. Miedema, W. Quevedo, B. O'Cinneide, M. Fondell, M. Beye, A. Pietzsch, M. Ross, M. Khalil, and A. Föhlisch, "Molecular Structures and Protonation State of 2-Mercaptopyridine in Aqueous Solution," *Chemical Physics Letters*, vol. 647, pp. 103–106, 2016.

[68] J. Norell, S. Eckert, B. E. Van Kuiken, A. Föhlisch, and M. Odelius, "*Ab Initio* Simulations of Complementary K-Edges and Solvatization Effects for Detection of Proton Transfer in Aqueous 2-Thiopyridone," *The Journal of Chemical Physics*, vol. 151, p. 114117, 2019.

[69] B. M. Messer, C. D. Cappa, J. D. Smith, W. S. Drisdell, C. P. Schwartz, R. C. Cohen, and R. J. Saykally, "Local hydration environments of amino acids and dipeptides studied by X-ray spectroscopy of liquid microjets," *The Journal of Physical Chemistry B*, vol. 109, pp. 21640–21646, Nov. 2005.

[70] A. Pietzsch, F. Hennies, P. S. Miedema, B. Kennedy, J. Schlappa, T. Schmitt, V. N. Strocov, and A. Föhlisch, "Snapshots of the Fluctuating Hydrogen Bond Network in Liquid Water on the Sub-Femtosecond Timescale With Vibrational Resonant Inelastic X-Ray Scattering," *Physical Review Letters*, vol. 114, pp. 088302–1–5, 2015.

[71] R. K. Lam, J. W. Smith, and R. J. Saykally, "Communication: Hydrogen bonding interactions in water-alcohol mixtures from X-ray absorption spectroscopy," *The Journal of Chemical Physics*, vol. 144, p. 191103, May 2016.

[72] V. Vaz da Cruz, F. Gel'mukhanov, S. Eckert, M. Iannuzzi, E. Ertan, A. Pietzsch, R. C. Couto, J. Niskanen, M. Fondell, M. Dantz, T. Schmitt, X. Lu, D. McNally, R. M. Jay, V. Kimberg, A. Föhlisch, and M. Odelius, "Probing hydrogen bond strength in liquid water by resonant inelastic X-ray scattering," *Nature Communications*, vol. 10, pp. 1–9, 2019.

Chapter 2

OBSERVING VIBRONIC COUPLING IN A STRONGLY HYDROGEN BONDED COMPLEX WITH COHERENT MULTIDIMENSIONAL VIBRATIONAL-ELECTRONIC SPECTROSCOPY

The work in this chapter has been submitted for publication. The supporting information is included in Appendix A.

- Caroline M. Loe, Srijan Chatterjee, Robert B. Weakly, and Munira Khalil, "Observing Vibronic Coupling in a Strongly Hydrogen Bonded Complex with Coherent Multidimensional Vibrational-Electronic Spectroscopy," *Under review,* 2024.

The coupled structural and electronic parameters of intramolecular hydrogen bonding play an important role in ultrafast chemical reactions such as proton transfer processes. In this chapter, I describe one- and two-dimensional vibrational-electronic (1D and 2D VE) spectroscopy experiments to understand the couplings between vibrational and electronic coordinates in 10-Hydroxybenzo[h]quinoline, an ultrafast proton transfer complex. The experiments reveal that the OH stretch (ν_{OH}) is strongly coupled to the electronic excitation, and Fourier analysis of the one-dimensional data shows coherent oscillations from the low frequency backbone vibrational modes coupled to the ν_{OH} mode, resulting in an electronically detected vibronic signal. In-plane low-frequency vibrations at 242 cm^{-1} and 386 cm^{-1} change the hydrogen bond distance and modulate the observed electronic signal in the polarization-selective 1D VE experiment through orientation-dependent coupling with the ν_{OH} mode. Access to the excitation frequency axis with 2D VE experiments reveals that excitation frequency, detection frequency, and experimental delay affect the frequency and strength of the vibronic transitions observed. These results demonstrate evidence of direct coupling of the

high frequency ν_{OH} mode with the $S_1 \leftarrow S_0$ electronic transition in HBQ, and orientation-dependent couplings of the low-frequency 242 cm^{-1} and 386 cm^{-1} modes to the ν_{OH} mode and the electronic transition. This demonstration of multidimensional VE spectroscopy on HBQ reveals the potential of using 1D and 2D VE spectroscopy to develop a quantitative understanding of the role of vibronic coupling in hydrogen bonding and ultrafast proton transfer for complex systems.

2.1 Introduction

Proton transfer is an elementary reaction fundamental to many chemical and biological processes such as photosynthesis, biocatalysis, and enzymatic and protein function. [1, 2] Molecules which undergo excited state proton transfer have been investigated as promising luminescent components of stable white light generation and as fluorescent molecular probes. [3, 4] Hydrogen bonding is a key structural parameter influencing inter- and intramolecular proton transfer reactions in many molecules, and identifying the microscopic parameters impacting hydrogen bonding environments is essential to achieving an understanding of proton transfer processes. In the case of intramolecular proton transfer mediated by intramolecular hydrogen bonding the proton connects the donor (D) and acceptor (A) atoms via a covalent bond and hydrogen bond, respectively (D—H$\cdots$A). The motions of the proton and the electron density across the intramolecular hydrogen bond are intimately coupled in excited state intramolecular proton transfer (ESIPT) processes. Developing experimental tools to directly measure the couplings of proton vibrational motions (both high- and low-frequency) and electronic transitions will lead to an increased understanding of the role of vibronic couplings in proton transfer on the ground and excited electronic states in molecules.

10-Hydroxybenzo[h]quinoline (HBQ, Fig. 2.1) is a model complex that undergoes ultrafast ESIPT upon photoexcitation. [5–7] The ESIPT has been found to take place within 13 ± 5 fs. [8] On the ground state, it has a strong intramolecular hydrogen bond between the hydroxyl group and the proton acceptor (nitrogen) atom. [5, 9, 10] On the excited electronic

state, computational studies have predicted that the strong intramolecular hydrogen bond facilitates the ultrafast ESIPT. [11] It is generally well understood that many low-frequency modes (generally ≈50–300 cm^{-1}) couple anharmonically to hydrogen bonded OH stretches for solution-state molecules, and as hydrogen bond strength increases, the width of the OH stretching band increases and it shifts to lower frequencies. [12] The red-shifted frequency from a free OH stretch and broad bandwidth (≈500 cm^{-1} FWHM) of the IR spectrum of the OH stretch (ν_{OH}) in HBQ indicate that it is a strongly hydrogen-bonded system. Coherent low-frequency oscillations (<500 cm^{-1}) have been observed in the ultrafast infrared pump-probe spectra of HBQ and are shown to modulate the proton donor-acceptor, or hydrogen bond, distance in the electronic ground state. [10] Similar coherent oscillations have been observed on the excited electronic state of HBQ with a variety of ultrafast experiments and computational methods. [8, 13–21] While the ground state dynamics and the photophysics of HBQ — during and following proton transfer — have been extensively studied, little information exists regarding the contributions of the ν_{OH} mode and coupled low-frequency modes to the electronic transition itself. The vibronic progression on the electronic absorption spectrum of HBQ has been noted and fit to a sum of gaussians. [17, 22] In addition to an intramolecular hydrogen bond likely influencing the electronic structure of HBQ, intermolecular hydrogen bonding with the solvent and the addition of electron donating or withdrawing substituents to the phenyl ring in the backbone of HBQ change both the structure and energy of the electronic absorption spectrum. [23, 24] Gaining an understanding of the vibronic coupling between the ν_{OH} vibration, coupled low-frequency vibrations, and the $S_1 \leftarrow S_0$ transition is crucial for developing a quantitative description of the ESIPT process in HBQ.

Although many studies already employ electronic pump - vibrational probe experiments to investigate vibronic coupling in condensed phase systems, fewer experimental examples exist which map the coherent coupling of ground state vibrations to an electronic transtion. In an important work, Ishii et al. studied the roles of mechanical and electrical anharmonicity in the vibronic coupling of a ground state ν_{OH} mode to the electronic transition in quinizarin,

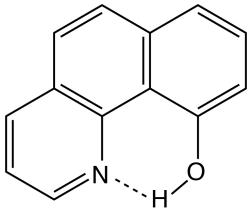

Figure 2.1. 10-hydroxybenzo[h]quinoline

a similar system to HBQ, with a strong intramolecular hydrogen bond. Their experiment used an infrared pump resonant with the ν_{OH} mode and a visible probe pulse resonant with the red edge of an optical transition to measure the modulation of the electronic absorption spectrum following the excitation of the ν_{OH} mode. [25] Vibrational pump - electronic probe studies have also been used to determine intra- and intermolecular vibrational relaxation timescales in molecular liquids. [26] Various other methods make use of both vibrational pump and electronic push pulse or detection schemes, such as fluorescence encoded infrared spectroscopy (FEIR), two-dimensional terahertz-infrared-visible spectroscopy (2D TIRV), and vibrationally promoted electronic resonance (VIPER). [27–29] Gallop et al. recently utilized a similar multicolor experiment with two resonant IR excitation pulses followed by a resonant electronic probe pulse to demonstrate vibrational control of an optoelectronic device. [30] We have developed one- and two-dimensional coherent vibrational-electronic spectroscopy (1D and 2D VE) to map vibronic coupling strength and relative orientation between coupled ground state vibrational modes and electronic transitions involving ligand-to-metal and metal-to-metal charge transfer excitations. [31–37]

In this work, we resonantly pump the ν_{OH} and ν_{CH} vibrational modes in HBQ, which coherently excites low-frequency vibrations anharmonically coupled to the ν_{OH} mode, and detect an oscillatory signal in the near-UV, resonant with the $S_1 \leftarrow S_0$ transition using 1D VE spectroscopy. Oscillation signal frequencies are found to match low-frequency backbone vibrations that modulate the hydrogen bonding moiety. 2D VE experiments provide IR excitation frequency resolution, and show different coupling strengths of the excited ν_{OH}

mode to the electronic transition, depending on IR excitation frequency (ω_1), near-UV detection frequency (ω_3), and experimental delay between the IR and the near-UV pulses (τ_2). Our experiments demonstrate evidence of direct coupling between the high-frequency ν_{OH} mode and orientation-dependent coupling of the two low-frequency modes at 242 cm^{-1} and 386 cm^{-1} to the $S_1 \leftarrow S_0$ transition in HBQ.

2.2 Experimental Methods

To produce the pump and probe lines, a 1 kHz regenerative amplifier (Coherent Astrella) is seeded with the output of an oscillator (Coherent Vitara) to produce 7 mJ, sub-35 fs pulses centered at 800 nm (Fig. 2.2). The amplified output is split; a 3 mJ portion enters an optical parametric amplifier (Light Conversion TOPAS), whose output signal and idler produce 3.45 µm mid-infrared (MIR) pulses via difference frequency generation (DFG, Light Conversion NDFG) with a spectral bandwidth of 517 cm^{-1} at full width at half maximum (FWHM). Pump pulses were characterized with an autocorrelation and found to be 50 fs FWHM at the sample area. The broadband near-UV (BBnUV) probe pulse is produced via a method similar to that previously reported by Gaynor et al., but with several modifications and updates. [38, 39] A concave spherical mirror with a 1.5 m focal length is used to focus the fundamental through the spectral broadening media. The thin media used for spectral broadening here are five 100 ± 0.127 µm UV grade fused silica plates (Valley Design), rather than N-BK7. The plates are set to Brewster's angle to minimize reflective losses, and spaced to maximize spectral broadening via self-phase modulation as described by He et al. and Lu et al. [40, 41] Figure 2.3 shows the difference between spectrally broadened (solid black) and un-broadened (dashed gray) light. The broadened fundamental is re-collimated using a second concave spherical mirror, this time with a 300 mm focal length. The pulse is frequency doubled in a 50 µm thick type I BBO crystal and then compressed with a pair of fused silica prisms, re-collimated, and routed to the sample area. The probe pulse was characterized by a cross-correlation with the MIR pump pulse in calcium fluoride, [32, 42] and found to be ≈ 100 fs with a 1,140 cm^{-1} (19 nm) bandwidth at FWHM.

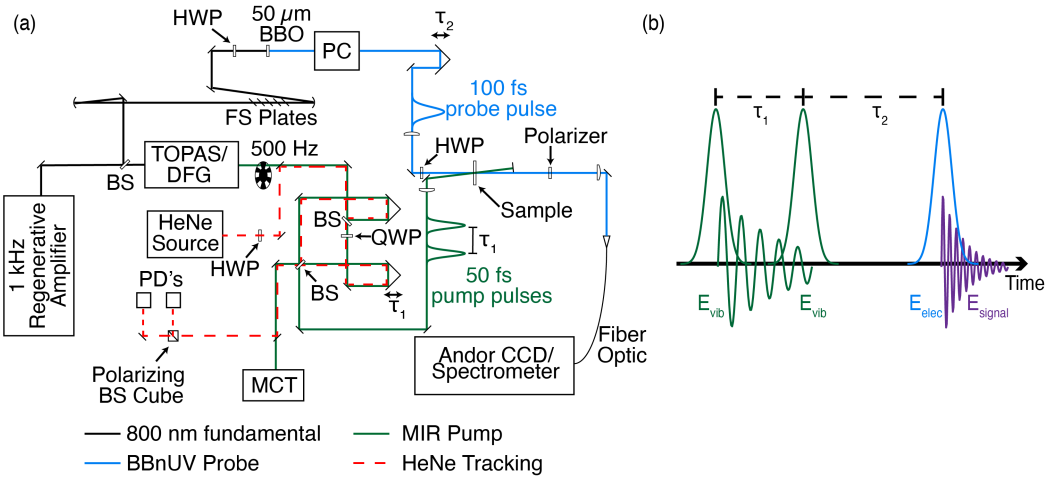

Figure 2.2. a) 2D VE experimental layout. The 800 nm output of a 1 kHz regenerative amplifier (Coherent Astrella) is split by a beamsplitter (BS). One arm is focused, sent through five 100 µm-thick fused silica (FS) plates, a half waveplate (HWP), and doubled with a 50 µm thick BBO crystal to produce the BBnUV probe, which is then compressed using a pair of fused silica prisms (PC) and routed to the sample. The other 800 nm output is sent through an optical parametric amplifier (Light Conversion TOPAS and DFG). Difference frequency generation (DFG) of the signal and idler produce 3.45 µm MIR light, which is mechanically chopped at 500 Hz, vertically offset from the HeNe laser output and passed through a Mach-Zehnder interferometer. The HeNe is detected at the two photodiodes using the fast scanning method with quadrature detection described previously. [34] The dark output of the interferometer is routed to the MCT detector to monitor the MIR interference for τ_1 tracking. The bright output provides the two phase-matched MIR pump pulses, separated by a variable delay, τ_1. Signal and probe copropagate following the sample area and are detected at the fiber optic. b) 2D VE pulse sequence. MIR pump pulses (green, E_{vib}) are separated by τ_1 and followed by the BBnUV probe pulse (blue, E_{elec}), which propagates with the signal (purple, E_{sig}). In a 1D VE experiment, $\tau_1 = 0$ fs.

The MIR pump pulses are focused to a $1/e^2$ diameter of 150 µm and spatially overlapped with the BBnUV probe pulse at the sample area using a 100 µm pinhole. Temporal overlap is found using a 250 µm thick piece of silicon prior to characterization via cross-correlation. In a 1D VE experiment the delay stage is set to $\tau_1 = 0$ fs in order to use a single pump pulse. The MIR pump power for 1D VE was 4.0 µJ. Each pump pulse was 1.1 µJ in the 2D VE experiments. In a 2D VE experiment, the pump pulses are continually scanned over $\tau_1 =$

-150 fs – +1,800 fs at a rate of 0.06 mm/s; the collected shots are Fourier transformed to build the ω_1 frequency axis. The τ_1 delay is tracked with a HeNe laser beam offset vertically from the MIR pump pulses and the dark output of the interferometer. [34] The BBnUV probe is focused to a $1/e^2$ diameter of 130 µm, and delayed by τ_2 with respect to the second MIR pump pulse. The probe power was 10 nJ for both 1D and 2D VE experiments. In a 1D VE experiment, τ_2 is stepped in 10 fs increments to build the time axis. In a 2D VE experiment, τ_2 is held at a constant delay from the second pump pulse for each surface collected. Following the sample area, the probe and signal co-propagate and are coupled into a multimode optical fiber for 2D experimnents (Thorlabs M15LO2) or a single mode optical fiber for 1D experiments (Thorlabs S405-XP) using a 10X magnification objective lens (Newport). The output of the fiber is coupled to a spectrometer (Andor Shamrock 303i) which spectrally disperses the signal and probe onto a 200 x 1600 pixel array EMCCD (Andor Newton DU970P, without the use of electron multiplying mode). The bottom 20 rows of 1600 pixels each are integrated for each laser shot. Alternating shots (pump on – pump off) are subtracted from one another and divided by the transmitted probe to obtain a normalized difference spectrum in $\Delta T/T$.

A solution of HBQ (TCI, used without further purification) in anhydrous carbon tetrachloride (Millipore Sigma) was prepared at a concentration of 25 mM. The sample solution was continually refreshed in a flow cell with a 50 µm teflon spacer between two 2 mm thick CaF_2 windows. The sample cell was translated vertically to further avoid sample damage. The polarization of the BBnUV probe was rotated 0° or 90° relative to the MIR pump pulses using a half waveplate, and the ZZZZ (parallel) or ZZYY (crossed) component of the signal was selected using an ultrabroadband linear polarizer (ThorLabs) immediately following the sample area for the polarization-selective experiments. Signal strength was found to scale linearly with MIR pump power (Fig. A.1).

The entire bandwidth of the ν_{OH} and ν_{CH} band in HBQ is resonantly excited with the pair of MIR pump pulses. Figure 2.2(b) shows the sequence of pulses used in a 2D VE experiment. The electronic transition, $S_1 \leftarrow S_0$, is resonantly probed by the BBnUV pulse following the

τ_2 delay. The resulting vibronic signal is detected, and alternating shots are subtracted from one another (pump on – pump off). Collected laser shots are assigned relative bin values (+1, -1, +0) based on the interference of the CW HeNe at the two photodiodes. One bin spans the time equivalent to a half-cycle of a HeNe wave, or 1.055 fs. Binned data are assigned τ_1 time values based on the $\tau_1 = 0$ shot and relative bin assignments, then zero-padded and fast Fourier transformed to construct a 2D plot with x- and y-axes corresponding to excitation (ω_1, with 7.7 cm^{-1} resolution) and detection (ω_3, with 2.4 cm^{-1} resolution) frequencies, respectively. Ref. 34 explains the data collection and processing for 2D VE experiments in greater detail. Each 2D scan is collected with 60,000 total shots across all τ_1 times. The 2D surfaces shown in this study are composed of 45-60 averaged scans (45-60 minutes of data) for each τ_2 delay and consist of between 730 and 975 difference shots per τ_1 point. 1D VE scans of HBQ in CCl_4 were collected by averaging four and eight scans of 1000 shots each per time point for ZZZZ and ZZYY, respectively. Neat solvent spectra were collected by averaging four scans of 1000 shots per time point for both polarization conditions. Frequency calculations with the anharmonic correction were performed with the unrestricted B3LYP functional and the 6-311++G(d,p) basis set, and are obtained from Ref. 10.

2.3 Results and Discussion

We present 1D VE spectra of HBQ in CCl_4 with probe frequency resolution in parallel (ZZZZ) and crossed (ZZYY) pump-probe polarization orientations. A Fourier transform of the 1D VE signal over τ_2 reveals that the intensities and positions of the frequencies are a function of input pulse polarization and detection frequency (ω_3). We find that relative intensities of frequencies in the Fourier transformed 1D VE spectra change between polarization conditions, including the correlation to detection frequency of the signal. Furthermore, we perform 2D VE measurements, gaining frequency resolution of the excitation (IR, ω_1) axis. We view changes in relative coupling strength of different regions of the ground state ν_{OH} mode to the electronic transition at different τ_2 delays, suggesting that coherently excited low-frequency vibrations also modulate the 2D VE signal.

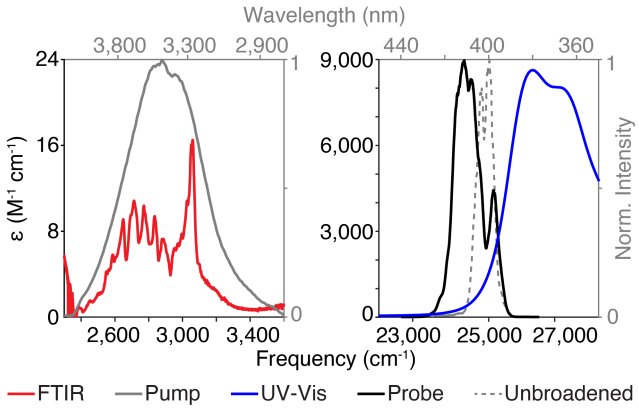

Figure 2.3. Ground state infrared and UV-Vis spectra of HBQ in CCl_4. FTIR spectrum (red) in the ν_{OH} and ν_{CH} stretching region and MIR pump spectrum (gray) are shown in the left panel in molar absorptivity and normalized intensity, respectively. The righthand panel shows the electronic absorption spectrum (blue) in molar absorptivity, and BBnUV probe spectrum (black) and unbroadened probe spectrum (dashed gray, shown for comparison) in normalized intensity. The bottom x-axes are shown in wavenumbers, while the tops are shown in nanometers. The IR pump bandwidth at FWHM = 517 cm^{-1}. The BBnUV probe bandwidth at FWHM = 1,140 cm^{-1} (19 nm), centered at 24,570 cm^{-1} (407 nm).

The ground state FTIR spectrum of HBQ in CCl_4 is reported in Fig. 2.3, which shows a ν_{OH} vibration centered at ≈2,755 cm^{-1} that is broadened and red-shifted from a free ν_{OH} vibration (≈3600 cm^{-1}). [12] The sharp feature at ≈3,050 cm^{-1} is assigned to the ν_{CH} mode, although there is some overlap between the ν_{OH} and ν_{CH} modes. [10] The complex structure, bandwidth, and red shift are all signatures of a strongly hydrogen bonded system, and arise from anharmonically coupled low-frequency modes with the ν_{OH} mode. The IR pump pulse is centered around the entire band to resonantly excite all modes in the band structure. The steady state electronic absorption spectrum of HBQ in CCl_4 is shown in Fig. 2.3 and is also structured, indicating a vibronic progression on the electronic excitation. The spectrum can be fit to a sum of gaussians, assuming that a single anharmonic vibration at ≈1290 cm^{-1} is responsible for the progression. [17, 22] The BBnUV pulse resonantly probes the red edge of the $S_1 \leftarrow S_0$ transition.

We have previously reported propensity rules for obtaining 1D and 2D VE signals. These

include nonzero linear and/or quadratic vibronic coupling, dependence of the electronic transition on the vibrational coordinates, and differences in vibrational dephasing dynamics for different electronic states. A 1D or 2D VE experiment accesses two types of signals; measured in transmission mode, they are a positively-signed ground state bleach (GSB) and a negatively-signed excited state absorption (ESA). For the excitation of a single vibrational mode, various GSB and ESA signals overlap across the detection frequency axis, separated by combinations of the frequency differences between vibrations in the ground and excited electronic states. For example, the pump pulses may excite a population in the first vibrational level of the electronic ground state ($\nu = 1$), which decays over τ_2. The probe excites the vibronic transition from $\nu = 1$ to the zeroth vibrational level in the excited electronic state, $\nu = 0'$, which corresponds to an ESA. A low frequency vibration (ν_{low}) may be coherently excited at the same time; rather than a population over τ_2, a coherence between $\nu = 1$ and ν_{low} could occur, which would modulate the observed vibronic signal over τ_2 in a VE experiment. A comprehensive discussion of the signals observed in VE spectroscopy following the excitation of one or more vibrational modes is provided in Refs. 32, 33, 36, 37.

2.3.1 1D VE Spectroscopy of HBQ in CCl_4

The 1D VE spectra measure the change in transmission of the BBnUV probe following resonant excitation of the ν_{OH} and ν_{CH} modes in HBQ. The negatively-signed signal indicates an ESA, or a new absorption from the high-frequency excited ν_{OH} mode to the electronic excited state. In addition to the high-frequency vibrations, low-frequency vibrations within the bandwidth of the IR pump pulse are coherently excited. Given that the BBnUV probe pulse is located at the very red edge of the electronic absorption spectrum, we predict that the observed ESA signal corresponds to a transition from $\nu_{OH} = 1$ to $\nu_{OH} = 0$'. The ESA signal can be fit with a biexponential decay plus an offset, both of which vary across the ω_3 axis. The fast decay time constant for both polarizations is less than ≈100 fs, or within the instrument response. For the ZZZZ signal, the slow time component ranges from 1.3 ± 0.2 ps to 4.1 ± 0.6 ps. For the ZZYY signal, the slow time component ranges from 1.0 ± 0.2 ps to

3.3 ± 0.9 ps. Error bars are calculated from averages of the data over separate scans. These time scales are within the range previously reported for infrared pump-probe studies of the ν_{OH} vibration in HBQ, including the offset past 4 ps which has been attributed to thermal equilibration dynamics. [10] On top of the broad ESA, there are clear oscillations over τ_2 at positive delays. Although the ESA signal exists past 4 ps, the oscillations decay earlier. Cuts with biexponential fits at single detection frequencies across the probe bandwidth are shown for sample and neat solvent in each polarization condition in Fig. A.2.

2.3.2 Frequency Analysis of 1D VE Spectra

We perform a fast Fourier transform (FFT) along τ_2 to construct the frequency correlation spectra shown in Figs. 2.5(c) and 2.5(d) as ω_3 (detection frequencies) versus ω_2. Prior to FFT, an offset and the biexponential fit are subtracted from the decaying oscillatory signal at each detection wavelength. A hyperbolic tangent windowing function (Fig. A.5) is applied to the residual from the exponential fit, and then zero padded and Fourier transformed to result in a frequency resolution of 6.5 cm^{-1} in the ω_2 axis. Biexponential fits and residuals at ω_3 = 24,288 cm^{-1} for ZZZZ and ZZYY polarizations are shown in Fig. 2.4(c). Following FFT, the spectrum is divided by the Fourier transform of the instrument response function (Fig. A.6) in order to return only the contribution to the observed signal that is proportional to the third order nonlinear response. [43] Projections are then normalized to the strongest solvent Raman peak, at 464 cm^{-1}, which is the polarized, totally symmetric C-Cl stretch. [44] Much of the oscillatory signal observed in the time domain is dominated by the solvent response (see Figs. A.3 and A.4 for neat solvent spectra). The Fourier transformed spectra in Fig. 2.5(b), seen as the projection onto ω_2, show that strong features appear at several frequencies in ω_2 for each polarization. In both polarization conditions, we observe frequencies at around 216 cm^{-1}, 320 cm^{-1}, and 464 cm^{-1} which we attribute to Raman-active modes of the CCl_4 solvent, and are denoted by red arrows in Fig. 2.5(b). [44] The IR pump pulse has sufficient bandwidth to excite these solvent vibrations, which then cause the solvent to experience a Raman-induced Kerr effect changing its index of refraction

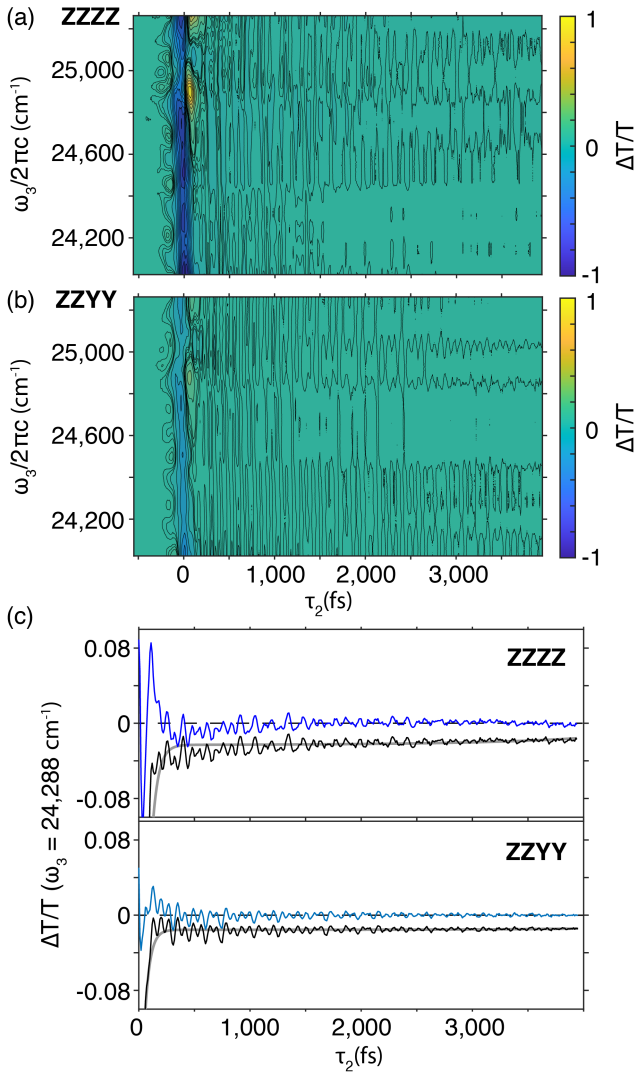

Figure 2.4. 1D VE spectra of 25 mM HBQ dissolved in CCl_4, normalized by the probe. a) Parallel polarization conditions (ZZZZ). b) Crossed polarization conditions (ZZYY). Contours in (a) and (b) are plotted every 10% with additional levels at 1.5, 3, and 4.5%, and are normalized to the maximum intensity in the ZZZZ spectrum. c) Cuts with biexponential fit at $\omega_3 = 24{,}288$ cm^{-1} in ZZZZ (black, top panel) and ZZYY (black, bottom panel). The residual from each fit is shown in dark blue and light blue for ZZZZ and ZZYY, respectively.

measured by change in transmission of the BBnUV probe pulse. [25, 45]

In addition to the solvent peaks, we find two additional low-frequency vibrational modes at 242 cm^{-1} and 386 cm^{-1}. The peak at 242 cm^{-1}, seen in the ZZZZ and ZZYY 1D VE

spectra (Figs. 2.5(b)-2.5(d)), has been observed in a multitude of experiments on both the ground and the excited electronic states in HBQ. Balasubramanian et al. reported this mode at 245 cm^{-1} coupling to the ν_{OH} mode using an IR pump-probe experiment, while accompanying anharmonic DFT calculations on the ground state show the mode at 241.8 cm^{-1} (Table 2.1). [10] DFT calculations show this mode to be a symmetric in-plane bend that modulates the hydrogen bond moiety (O–H$\cdots$N, Fig. 2.5(a)). Takeuchi and Tahara observed a Raman active mode in the ground state at 243 cm^{-1}. [13] Time-resolved experiments on the electronic excited state of HBQ have reported a low-frequency mode at 237–243 cm^{-1} with transient absorption [13, 16, 17] and at 240–241 cm^{-1} via time-resolved fluorescence. [8, 14] They assign this mode to the same in-plane breathing that we observe in our 1D VE spectra. Computational methods on the S_1 state have reported this mode at 247–254 cm^{-1}. [15, 16, 21]

The 1D VE FFT projections in Fig. 2.5(b) also show a weaker low-frequency mode in both polarization conditions at 386 cm^{-1}. We assign the 386 cm^{-1} feature to another skeletal deformation of the backbone of HBQ (asymmetric in-plane bend, Fig. 2.5(a)), calculated at 386.9 cm^{-1} (see Table A.1 in Appendix A for a full list of calculated frequencies). It has also been reported by experimental and computational studies on the ground and excited electronic states, as discussed below. Our previous IR pump-probe experiment did not observe this higher frequency mode, likely due to pump bandwidth limitations. [10] Ground state resonance Raman from Takeuchi et al. reports a 380 cm^{-1} mode, while on the excited state, transient absorption spectra show frequencies ranging from 388–396 cm^{-1}. [13, 16, 17] Time-resolved fluorescence experiments observed the mode at 389–392 cm^{-1}. [8, 14] Computational studies report frequencies of this mode at 389–408 cm^{-1}. [15, 16, 21] We note that the 386 cm^{-1} mode also modulates the O–H$\cdots$N distance along with the 242 cm^{-1} mode.

The ω_3 vs. ω_2 correlation spectra reveal that the strong low-frequency modes observed in the FFT projections in the 200-500 cm^{-1} range are localized to slightly different frequencies along the ω_3 axis (Figs. 2.5(c) and 2.5(d)). Of particular interest are the HBQ

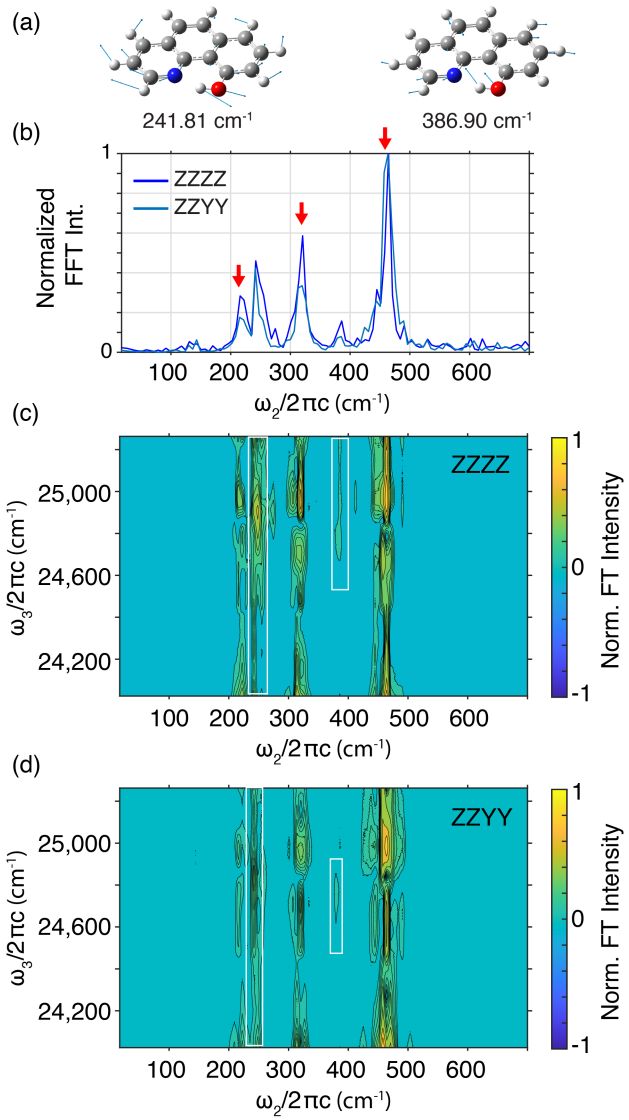

Figure 2.5. a) Relevant low-frequency ground state vibrations from DFT calculations. [10] b) Absolute value projections of the Fourier transform intensity for parallel (ZZZZ, dark blue) and crossed (ZZYY, light blue) polarization schemes, normalized to the most intense solvent peak. Red arrows denote solvent peaks from CCl_4. c) Absolute value FFT surface for ZZZZ experiment. d) Absolute value FFT surface for ZZYY experiment. Contours in (c) and (d) are plotted at 10, 20, 30, 40, 60, 80, and 100%, and are normalized to the maximum intensity in the ZZZZ FFT spectrum.

backbone modes at 242 cm^{-1} and 386 cm^{-1}. Both modes are more localized to higher probe energies where the electronic absorption of HBQ is stronger, whereas the solvent peaks are across the entire bandwidth of the probe. Slight differences of the frequency maxima in ω_3 ($\approx$ 100 cm^{-1}) between polarization conditions indicate that the relative angle between transition dipoles depends on where the $S_1 \leftarrow S_0$ transition is probed. Additionally, both polarizations show that the 242 cm^{-1} mode is localized to higher frequencies in ω_1 than the 386 cm^{-1} mode is. In the ZZZZ experiment, both modes are more highly correlated with probe frequencies to the blue, with peak maxima occurring at ω_3 = 24,902 cm^{-1} and ω_3 = 24,813 cm^{-1} for ω_2 = 242 cm^{-1} and ω_2 =386 cm^{-1}respectively. Conversely, peak maxima in the ZZYY experiment show higher correlation to slightly lower probe energies with maxima at ω_3 = 24,813 $cm^{-1}$and ω_3 = 24,752 cm^{-1} for the 242 cm^{-1} and 386 cm^{-1} modes, respectively. Extension of the probe pulse to UV wavelengths could reveal important differences in the anisotropy over the entire $S_1 \leftarrow S_0$ transition and confirm that the direction of the electronic transition dipole moment relative to low-frequency vibrations depends on the frequency of the probed electronic transition.

Table 2.1. Calculated (ω_j) and experimental (ω_2) frequencies of interest with IR intensities and cubic coupling strengths (β_{ijj}) between $i = \nu_{OH}$ and $j = \nu_{low}$, and resonance Raman frequencies.

Vibration	ω_j (cm^{-1}) [a]	IR Int. (a.u.) [a]	β_{ijj} (cm^{-1}) [a]	ω_2 (cm^{-1})	FFT Int.[b]	Raman (cm^{-1}) [c]
Symm. i.p. bend	241.81	3.3802	59.46	242 (ZZYY) 242 (ZZZZ)	0.43 0.46	243
Asymm. i.p. bend	386.90	2.0223	-14.29	386 (ZZYY) 386 (ZZZZ)	0.08 0.16	380

a. From Ref. 10.
b. Relative to the solvent mode at 464 cm^{-1}.
c. From Ref. 13.

The maximum intensities of solvent-subtracted HBQ low-frequency peaks at 242 cm^{-1}

and 386 cm^{-1} relative to the 464 cm^{-1} solvent peak are 0.46:0.16:1 for ZZZZ and 0.43:0.08:1 for ZZYY. Relative intensities of neat solvent peaks differ slightly from previously reported values, and are discussed in Appendix A. Intensity ratios between the 242 cm^{-1} and 386 cm^{-1} peaks are 3:1 and 5:1 for ZZZZ and ZZYY 1D VE signals, respectively, indicating that the 242 cm^{-1} mode is coupled more strongly to the $S_1 \leftarrow S_0$ transition through the ν_{OH} mode in both polarizations, and that the angles of their transition dipoles relative to the electronic transition are different. We can use the integrated relative amplitudes of the polarization-selective 1D VE signal to extract the angle of the low-frequency modes with the $S_1 \leftarrow S_0$ electronic transition. [36, 37] The relative angles between the vibrational transition dipole moments and the electronic transition dipole for the 242 cm^{-1} mode and the 386 cm^{-1} mode are 37 $\pm$ 2° and 29 $\pm$ 1°, respectively. A calculation of the relative angle between the transition dipole moments of the high-frequency ν_{OH} mode and the low-frequency calculated 242 cm^{-1} (386 cm^{-1}) mode was 22.13 ° (176.48°). All three transition dipole moments (electronic and vibrational) are in the same plane as HBQ. Interestingly, the relative intensities of these peaks are opposite to what has been observed in both ground state resonance Raman and transient absorption experiments, which was roughly 2:3. [13] This indicates that the ground electronic state 242 cm^{-1} vibration we observe is much more strongly coupled to the $S_1 \leftarrow S_0$ transition through the ν_{OH} mode than the 386 cm^{-1} mode is. The cubic coupling strength (obtained from anharmonic frequency calculations) calculated for the 242 cm^{-1} mode is significantly higher than that calculated for the 386 cm^{-1} mode (Table 2.1), which helps to explain the higher ratio of vibronic coupling strength seen in our 1D VE experiment.

Here we see that the high-frequency ν_{OH} mode is anharmonically coupled to the low-frequency modes and to the $S_1 \leftarrow S_0$ electronic transition. DFT calculations show the extent of delocalization in the molecular orbitals involved in HBQ's electronic excitation (Fig. A.9). Low-frequency modes such as the 242 cm^{-1} and 386 cm^{-1} vibrations modulate the ν_{OH} mode and the electron density across HBQ's backbone. A more quantitative understanding of the coupling will rely on calculating Franck-Condon and non-Franck Condon factors of the coupled high- and low-frequency modes with the $S_1 \leftarrow S_0$ transition. Structural changes affect

the local electronic environment of the hydrogen bond, contributing to electrical anharmonicity. Ishii and Tahara refer to an observed low-frequency mode as a "hydrogen bond modulating vibration" which appears as modulating the intensity of the electronic absorption following infrared excitation. They determine the role of mechanical versus electrical anharmonicity in quinizarin, another intramolecularly hydrogen bonded system and argue that electrical anharmonicity plays an important role in contributing to mechanical anharmonicity, which facilitates coupling between low- and high-frequency vibrations. [25] Our results agree with their conclusion that intramolecular hydrogen bonding in a π-conjugated system generally increases electronic delocalization; electrical anharmonicity between the ν_{OH} mode and a low-frequency mode (such as our observed 242 cm^{-1} and 386 cm^{-1} modes in HBQ, and their 319 cm^{-1} mode in quinizarin) occurs because the local hydrogen bonding environment is sensitive to structural changes that modulate the donor–acceptor distance and therefore the local electronic environment of the donor–acceptor moeity. We have recently performed computational multicolor X-ray spectroscopy offering a detailed picture of the local electronic environment around both the hydrogen bond donor (O–H) and acceptor (N). Our time-resolved X-ray calculations on HBQ have clearly shown that on the excited electronic state, the electronic environments around the hydrogen bond donor and acceptor experience modulation from low- and high-frequency hydrogen bond modulating vibrations. [19] In the 1D VE spectroscopy of HBQ, both the ground state low-frequency modes that we observe modulate the intramolecular hydrogen bond. We therefore expect that the electrical anharmonicity between each low-frequency mode and the ν_{OH} mode in HBQ plays an important role in the strong coupling to the $S_1 \leftarrow S_0$ transition through the ν_{OH} mode.

2.3.3 2D VE of HBQ

Due to the broad nature of the OH stretching band, 1D VE alone is not enough to determine vibrational contributions to the UV-Vis spectrum of HBQ, and corresponding vibronic coupling strengths. In addition to investigating the coupling of the OH stretch and other coupled low-frequency vibrations to the electronic transition via 1D VE spectroscopy, we also

perform 2D VE spectroscopy in order to gain frequency resolution of the IR pump axis (ω_1). One 2D VE surface with parallel polarizations of the pump and probe pulses is collected at a single τ_2 point, while the delay between the two IR pump pulses is scanned and Fourier transformed. Spectra shown below are normalized by the intensity of the BBnUV probe at each τ_1 time point prior to Fourier transformation.

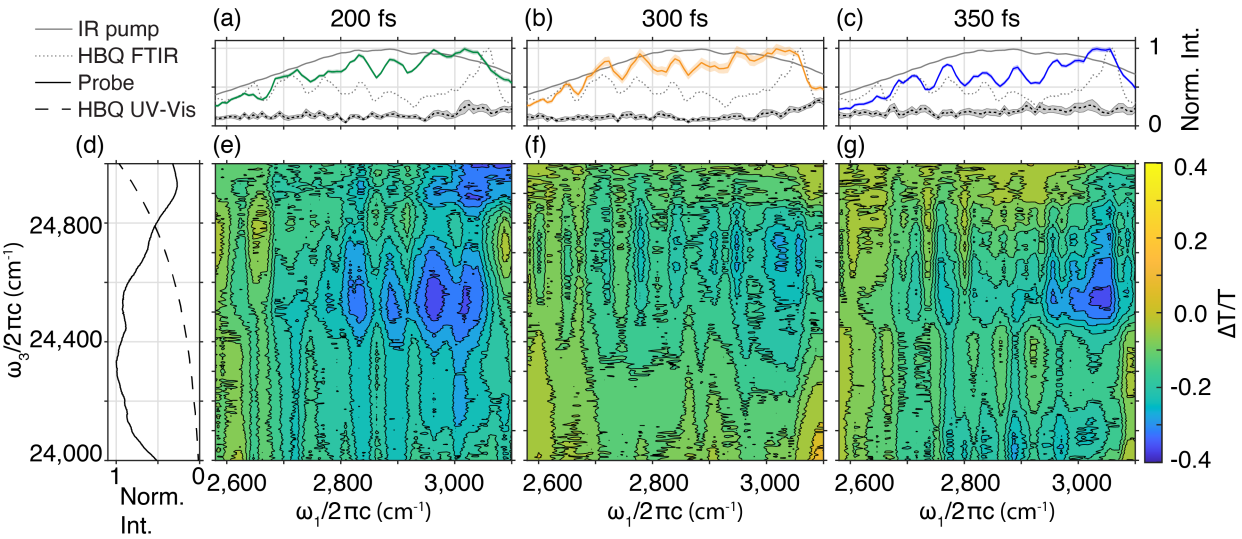

Figure 2.6. 2D VE spectra of HBQ in CCl_4 at τ_2 = 200 fs, 300 fs, and 350 fs, normalized by the probe. The broad feature at ω_1 = 2,650-3,100 cm^{-1} corresponds to excited state absorption (ESA) from the excited ν_{OH} mode. a-c) MIR pump spectrum (solid gray), HBQ FTIR spectrum (dashed gray), and absolute value of ω_1 projections of the 2D VE ESA signal at τ_2 = 200 fs (green), 300 fs (orange), and 350 fs (blue). Projections are normalized to the ν_{CH} feature. Absolute value of solvent 2D VE projections onto ω_1 are shown for each time point in dotted black with gray error bars. d) BBnUV probe (solid black) and ground state UV-Vis spectrum (dashed black). e-g) 2D VE spectra at τ_2 = 200, 300, and 350 fs, corresponding to the projections shown in a-c. Contours are normalized to the maximum signal in (e) and plotted at every 10% in ΔT/T.

Figure 2.6 shows 2D VE spectra of HBQ in CCl_4 at three τ_2 delays: 200 fs, 300 fs, and 350 fs (see Fig. A.7 for solvent 2D VE spectra). The spectral features at each τ_2 point are complex and structured. There is a broad negative signal at each τ_2 delay, indicating an excited state absorption that we assign as a transition from $\nu_{OH} = 1$ to the excited electronic

state ($\nu_{OH} = 0$') as observed in the 1D VE spectra. The top panel (Figs. 2.6(a)-2.6(c)) shows the IR pump spectrum (solid gray), the ground state FTIR spectrum (dotted gray), and the absolute value of the projection of the 2D VE signal onto ω_1 (green, orange, and blue). The absolute value of the projections of solvent spectra are shown in dotted black lines with gray error bars calculated from averages over different scans. The structure of the observed spectral features in each 2D VE spectrum closely matches the structure of the ν_{OH} mode in the ground state FTIR spectrum.

Figure 2.6(d) shows the BBnUV probe pulse (solid black) and the UV-Vis spectrum of HBQ (dashed black). The 2D VE experiment probes the very red edge of the electronic absorption in HBQ, which could be one reason that following normalization of the signal by the probe, the signal is still somewhat localized to the blue edge of the spectrum where the electronic transition is stronger, as in the 1D VE spectra. Projections of the ESA onto the excitation axis (Figs. 2.6(a)-2.6(c)) reveal that ground state frequencies between ≈2,900–3,050 cm^{-1} couple more strongly to the electronic transition than other regions under the band. From DFT calculations, the red half of the IR spectrum (≈2,600–2,850 cm^{-1}) has contributions from the ν_{OH} mode and coupling to low-frequency modes, while the blue half (≈ 2,850–3,100 cm^{-1}) is made up of more ν_{CH} modes as well as couplings with other low-frequency modes. As mentioned earlier, IR pump-probe studies have also demonstrated by pumping only the ν_{OH} mode that it is anharmonically coupled to low-frequency vibrations. [10] At $\tau_2 = 300$ fs (Figs. 2.6(b) and 2.6(f)) the projection intensities of the blue half and the red half are nearly equal. Conversely, at $\tau_2 = 350$ fs the projection intensity of the red half is roughly 70% of the blue. Figure A.8 directly compares the ω_1 projection for each τ_2 delay, normalized to the highest peak. Each projection has error bars corresponding to the standard error of the observed difference signal.

The intensities of the signal under the red half of the ν_{OH} band appear to change as a function of τ_2 relative to the blue half in both the ω_1 and ω_3 dimensions. Recent studies have investigated vibronic coherence transfer and evolution in excited electronic states with 2D electronic-vibrational spectroscopy (2D EV) and 2D electronic spectroscopy (2D

ES). [36, 39, 46] Further study will be required to fully understand the evolution of vibronic coherences from the electronic ground state, but initial results and analysis suggest that the intensity of different ESA peak areas corresponding to structure in the FTIR spectrum oscillate at low frequencies over τ_2. We hypothesize that these frequencies will match the low-frequency backbone motions observed in the 1D VE experiments. Extension of 2D VE to a 3D VE experiment by Fourier transform over τ_2 would resolve coherences between the high-frequency ν_{OH} mode and the associated low-frequency modes as a function of ω_1 and ω_3. Fourier transform of our 1D VE experiments provides the first step in developing an understanding of how low-frequency hydrogen bond modulating vibrations contribute to the electronic absorption spectrum in strongly hydrogen bonded systems such as HBQ. As previously discussed, electronic delocalization in HBQ contributes to the electrical anharmonicity as evidenced by the presence of low frequency modes modulating the electronically-detected signal in 1D VE experiments. The same is true in the 2D experiment, except it provides the ability to pinpoint the excitation frequencies in ω_1 that are coupled most strongly to both the hydrogen bond modulating low-frequency modes, and ω_3, or the electronic absorption spectrum. Connecting both high- and low-frequency vibrations to areas of the electronic absoprtion spectrum allows for a more complete description and understanding of the electronic transition in HBQ, and will further inform our understanding of excited state proton transfer processes in essential chemical and biological functions.

2.4 Summary and Outlook

We observe direct coupling of the ground state ν_{OH} mode to the electronic transition in 10-Hydroxybenzo[h]quinoline, and indirect coupling of low-frequency backbone vibrations to the electronic excitation through the ν_{OH} mode. Polarization-selective 1D VE experiments access the orientation-dependent coupling between low-frequency ground state vibrations (242 cm^{-1} and 386 cm^{-1}) and the $S_1 \leftarrow S_0$ electronic transition. The 242 cm^{-1} mode exhibits the strongest coupling to the electronic transition through the ν_{OH} mode. Using 2D VE spectroscopy, we also determine regions of the ν_{OH} band which couple most strongly

to the electronic excitation, which provides frequency resolution of the broad and complexly structured ν_{OH} stretching region across the excitation axis (ω_1). Preliminary analysis of 2D VE data at three τ_2 delays suggests that specific areas of the observed vibronic signal oscillate at low frequencies and are localized to certain ω_3 frequencies; 2D data will require further experimentation and study to resolve any associated low-frequency vibrations and to fully understand their role in the electronic spectrum of HBQ. By combining the structurally sensitive vibrational spectroscopy with electronic excitation, we are able to gain direct insight to the impact of the ground state nuclear fluctuations on electronic excited state processes such as ESIPT. Furthermore, future fifth order experiments may link ground electronic state vibrations to excited state vibrations and help to elucidate the role of the ground state vibrations in the ESIPT of HBQ and other proton-transfer systems.

BIBLIOGRAPHY

[1] T. Kumpulainen, B. Lang, A. Rosspeintner, and E. Vauthey, "Ultrafast Elementary Photochemical Processes of Organic Molecules in Liquid Solution," *Chemical Reviews*, vol. 117, pp. 10826–10939, Aug. 2017.

[2] H. Ishikita and K. Saito, "Proton transfer reactions and hydrogen-bond networks in protein environments," *Journal of The Royal Society Interface*, vol. 11, p. 20130518, Feb. 2014.

[3] J. E. Kwon and S. Y. Park, "Advanced Organic Optoelectronic Materials: Harnessing Excited-State Intramolecular Proton Transfer (ESIPT) Process," *Advanced Materials*, vol. 23, pp. 3615–3642, 2011.

[4] J. Zhao, S. Ji, Y. Chen, H. Guo, and P. Yang, "Excited State Intramolecular Proton Transfer (ESIPT): From Principal Photophysics to the Development of New Chromophores and Applications in Fluorescent Molecular Probes and Luminescent Materials," *Physical Chemistry Chemical Physics*, vol. 14, pp. 8803–8817, 2012.

[5] M. L. Martinez, W. C. Cooper, and P.-T. Chou, "A Novel Excited-State Intramolecular Proton Transfer Molecule, 10-Hydroxybenzo[*h*]quinoline," *Chemical Physics Letters*, vol. 193, no. 1-3, pp. 151–154, 1992.

[6] P.-T. Chou and M. L. Martinez, "Photooxygenation of 3-hydroxyflavone and molecular design of the radiation-hard scintillator based on the excited-state proton transfer," *Radiation Physics and Chemistry*, vol. 41, no. 1/2, pp. 373–378, 1993.

[7] P.-T. Chou, Y.-C. Chen, W.-S. Yu, Y.-H. Chou, C.-Y. Wei, and Y.-M. Cheng, "Excited-State Intramolecular Proton Transfer in 10-Hydroxybenzo[*h*]quinoline," *The Journal of Physical Chemistry A*, vol. 105, pp. 1731–1740, Mar. 2001.

[8] C. H. Kim and T. Joo, "Coherent Excited State Intramolecular Proton Transfer Probed by Time-Resolved Fluorescence," *Physical Chemistry Chemical Physics*, vol. 11, no. 44, pp. 10266–10269, 2009.

[9] M. Kubicki, T. Borowiak, and W. Z. Antkowiak, "10-Hydroxybenzo[h]quinoline," *Acta Crystallographica Section C*, vol. 51, pp. 1173–1175, 1995.

[10] M. Balasubramanian, A. Reynolds, T. J. Blair, and M. Khalil, "Probing Ultrafast Vibrational Dynamics of Intramolecular Hydrogen Bonds with Broadband Infrared Pump-Probe Spectroscopy," *Chemical Physics*, vol. 519, pp. 38–44, Mar. 2019.

[11] M. Zhou, J. Zhao, Y. Cui, Q. Wang, Y. Dai, P. Song, and L. Xia, "Theoretical Study on the Excited-State Intramolecular Proton-Transfer Reaction of 10-Hydroxybenzo[*h*]quinoline in Methanol and Cyclohexane," *Journal of Luminescence*, vol. 161, pp. 1–6, May 2015.

[12] E. T. J. Nibbering and T. Elsaesser, "Ultrafast Vibrational Dynamics of Hydrogen Bonds in the Condensed Phase," *Chemical Reviews*, vol. 104, pp. 1887–1914, Apr. 2004.

[13] S. Takeuchi and T. Tahara, "Coherent Nuclear Wavepacket Motions in Ultrafast Excited-State Intramolecular Proton Transfer: Sub-30-fs Resolved Pump–Probe Absorption Spectroscopy of 10-Hydroxybenzo[*h*]quinoline in Solution," *The Journal of Physical Chemistry A*, vol. 109, pp. 10199–10207, Nov. 2005.

[14] J. Lee, C. H. Kim, and T. Joo, "Active Role of Proton in Excited State Intramolecular Proton Transfer Reaction," *The Journal of Physical Chemistry A*, vol. 117, pp. 1400–1405, 2013.

[15] M. Higashi and S. Saito, "Direct Simulation of Excited-State Intramolecular Proton Transfer and Vibrational Coherence of 10-Hydroxybenzo[*h*]quinoline in Solution," *The Journal of Physical Chemistry Letters*, vol. 2, pp. 2366–2371, 2011.

[16] J. W. Kim, C. H. Kim, C. Burger, M. Park, M. F. Kling, D. E. Kim, and T. Joo, "Non-Born–Oppenheimer Molecular Dynamics Observed by Coherent Nuclear Wave Packets," *The Journal of Physical Chemistry Letters*, vol. 11, pp. 755–761, 2020.

[17] C. Schriever, M. Barbatti, K. Stock, A. J. Aquino, D. Tunega, S. Lochbrunner, E. Riedle, R. de Vivie-Riedle, and H. Lischka, "The Interplay of Skeletal Deformations and Ultrafast Excited-State Intramolecular Proton Transfer: Experimental and Theoretical Investigation of 10-Hydroxybenzo[*h*]quinoline," *Chemical Physics*, vol. 347, pp. 446–461, 2008.

[18] W. Chansen, R. Salaeh, C. Prommin, K. Kerdpol, R. Daengngern, and N. Kungwan, "Theoretical Study on Influence of Geometry Controlling Over the Excited-State Intramolecular Proton Transfer of 10-Hydroxybenzo[*h*]quinoline and its Derivatives," *Computational and Theoretical Chemistry*, vol. 1113, pp. 42–51, 2017.

[19] C. M. Loe, C. Liekhus-Schmaltz, N. Govind, and M. Khalil, "Spectral signatures of ultrafast excited-state intramolecular proton transfer from computational multi-edge

transient x-ray absorption spectroscopy," *The Journal of Physical Chemistry Letters*, vol. 12, pp. 9840–9847, Oct. 2021.

[20] L. Zhang, F. Fassioli, B. Fu, Z.-S. She, and G. D. Scholes, "Modeling Excited-State Proton Transfer Using the Lindblad Equation: Quantification of Time-Resolved Spectroscopy with Mechanistic Insights," *ACS Physical Chemistry Au*, vol. 3, pp. 107–118, Jan. 2023.

[21] D. Picconi, "Nonadiabatic quantum dynamics of the coherent excited state intramolecular proton transfer of 10-hydroxybenzo[h]quinoline," *Photochemical & Photobiological Sciences*, vol. 20, pp. 1455–1473, Nov. 2021.

[22] J. D. Gaynor, *Correlated Electronic and Vibrational Motion: A Direct Perspective Through Multidimensional Electronic-Vibrational Spectroscopy*. PhD thesis, University of Washington, 2019.

[23] S. Hristova, G. Dobrikov, F. S. Kamounah, S. Kawauchi, P. E. Hansen, V. Deneva, D. Nedeltcheva, and L. Antonov, "10-Hydroxybenzo[*h*]quinoline: Switching Between Single- and Double-Well Proton Transfer Through Structural Modifications," *RSC Advances*, vol. 5, pp. 102495–102507, 2015.

[24] H. Marciniak, S. Hristova, V. Deneva, F. S. Kamounah, P. E. Hansen, S. Lochbrunner, and L. Antonov, "Dynamics of Excited State Proton Transfer in Nitro Substituted 10-Hydroxybenzo[*h*]quinolines," *Physical Chemistry Chemical Physics*, vol. 19, no. 39, pp. 26621–26629, 2017.

[25] K. Ishii, S. Takeuchi, and T. Tahara, "Infrared-induced coherent vibration of a hydrogen-bonded system: Effects of mechanical and electrical anharmonic couplings," *The Journal of Chemical Physics*, vol. 131, p. 044512, Jul. 2009.

[26] C. M. Cheatum, M. M. Hecksher, D. Bingemann, and F. F. Crim, "CH2I2 fundamental vibrational relaxation in solution studied by transient electronic absorption spectroscopy," *The Journal of Chemical Physics*, vol. 115, no. 15, 2001.

[27] J. N. Mastron and A. Tokmakoff, "Fourier Transform Fluorescence - Encoded Infrared Spectroscopy," *The Journal of Physical Chemistry A*, vol. 122, pp. 554–562, Jan. 2018.

[28] M. Grechko, T. Hasegawa, F. D'Angelo, H. Ito, D. Turchinovich, Y. Nagata, and M. Bonn, "Coupling between intra- and intermolecular motions in liquid water revealed by two-dimensional terahertz-infrared-visible spectroscopy," *Nature Communications*, vol. 9, pp. 1–8, Feb. 2018.

[29] L. J. van Wilderen, A. T. Messmer, and J. Bredenbeck, "Mixed IR/Vis two-dimensional spectroscopy: Chemical exchange beyond the vibrational lifetime and sub-ensemble selective photochemistry," *Angewandte Chemie International Edition*, vol. 53, pp. 2667–2672, 2014.

[30] N. P. Gallop, D. R. Maslennikov, N. Mondal, K. P. Goetz, Z. Dai, A. M. Schankler, W. Sung, S. Nihonyanagi, T. Tahara, M. I. Bodnarchuk, M. V. Kovalenko, Y. Vaynzof, A. M. Rappe, and A. A. Bakulin, "Ultrafast vibrational control of organohalide perovskite optoelectronic devices using vibrationally promoted electronic resonance," *Nature Materials*, vol. 23, pp. 88–94, Jan. 2024.

[31] T. L. Courtney, Z. W. Fox, L. Estergreen, and M. Khalil, "Measuring Coherently Coupled Intramolecular Vibrational and Charge-Transfer Dynamics with Two-Dimensional Vibrational-Electronic Spectroscopy," *The Journal of Physical Chemistry Letters*, vol. 6, pp. 1286–1292, Apr. 2015.

[32] T. L. Courtney, Z. W. Fox, K. M. Slenkamp, and M. Khalil, "Two-dimensional vibrational-electronic spectroscopy," *The Journal of Chemical Physics*, vol. 143, p. 154201, Oct. 2015.

[33] J. D. Gaynor and M. Khalil, "Signatures of vibronic coupling in two-dimensional electronic-vibrational and vibrational-electronic spectroscopies," *TheJournal of Chemical Physics*, vol. 147, p. 094202, 2017.

[34] Z. W. Fox, T. J. Blair, R. B. Weakly, T. L. Courtney, and M. Khalil, "Implementation of Continuous Fast Scanning Detection in Femtosecond Fourier-Transform Two-Dimensional Vibrational-Electronic Spectroscopy to Decrease Data Acquisition Time," *Review of Scientific Instruments*, vol. 89, pp. 113104–1–7, Nov. 2018.

[35] Z. W. Fox, T. J. Blair, and M. Khalil, "Determining the Orientation and Vibronic Couplings between Electronic and Vibrational Coordinates with Polarization-Selective Two-Dimensional Vibrational-Electronic Spectroscopy," *The Journal of Physical Chemistry Letters*, vol. 11, pp. 1558–1563, 2020.

[36] J. D. Gaynor, R. B. Weakly, and M. Khalil, "Multimode two-dimensional vibronic spectroscopy. I. Orientational response and polarization-selectivity," *The Journal of Chemical Physics*, vol. 154, p. 184201, 2021.

[37] R. B. Weakly, J. D. Gaynor, and M. Khalil, "Multimode two-dimensional vibronic spectroscopy. II. Simulating and extracting vibronic coupling parameters from polarization-selective spectra," *The Journal of Chemical Physics*, vol. 154, p. 184202, 2021.

[38] J. D. Gaynor, A. Petrone, X. Li, and M. Khalil, "Mapping vibronic couplings in a solar cell dye with polarization-selective two-dimensional electronic-vibrational spectroscopy," *The Journal of Physical Chemistry Letters*, vol. 9, pp. 6289–6295, 11 2018.

[39] J. D. Gaynor, J. Sandwisch, and M. Khalil, "Vibronic coherence evolution in multidimensional ultrafast photochemical processes," *Nature Communications*, vol. 10, pp. 1–9, 2019.

[40] P. He, Y. Liu, K. Zhao, H. Teng, X. He, P. Huang, H. Huang, S. Zhong, Y. Jiang, S. Fang, X. Hou, and Z. Wei, "High-efficiency supercontinuum generation in solid thin plates at 0.1 TW level," *Optics Letters*, vol. 42, no. 3, p. 474, 2017.

[41] C. H. Lu, Y. J. Tsou, H. Y. Chen, B. H. Chen, Y. C. Cheng, S. D. Yang, M. C. Chen, C. C. Hsu, and A. H. Kung, "Generation of intense supercontinuum in condensed media," *Optica*, vol. 1, no. 6, pp. 400–406, 2014.

[42] S. Yeremenko, A. Baltuška, F. de Haan, M. S. Pshenichnikov, and D. A. Wiersma, "Frequency-resolved pump–probe characterization of femtosecond infrared pulses," *Optics Letters*, vol. 27, no. 13, p. 1171, 2002.

[43] D. McMorrow and W. T. Lotshaw, "The frequency response of condensed-phase media to femtosecond optical pulses: spectral-filter effects," *Chemical Physics Letters*, vol. 174, pp. 85–94, Oct. 1990.

[44] M. Khalil, O. Golonzka, N. Demirdöven, C. J. Fecko, and A. Tokmakoff, "Polarization-selective femtosecond Raman spectroscopy of isotropic and anisotropic vibrational dynamics in liquids," *Chemical Physics Letters*, vol. 321, pp. 231–237, Apr. 2000.

[45] D. Heiman, R. W. Hellwarth, M. D. Levenson, and G. Martin, "Raman-Induced Kerr Effect," *Physical Review Letters*, vol. 36, pp. 189–192, Jan. 1976.

[46] V. R. Policht, A. Niedringhaus, R. Willow, P. D. Laible, D. F. Bocian, C. Kirmaier, D. Holten, T. Mančal, and J. P. Ogilvie, "Hidden Vibronic and Excitonic Structure and Vibronic Coherence Transfer in the Bacterial Reaction Center," *Science Advances*, vol. 8, pp. 1–10, 2022.

Chapter 3

SPECTRAL SIGNATURES OF ULTRAFAST EXCITED STATE INTRAMOLECULAR PROTON TRANSFER FROM COMPUTATIONAL MULTI-EDGE TRANSIENT X-RAY ABSORPTION SPECTROSCOPY

 The supporting information for this chapter is included in Appendix B.

Excited state intramolecular proton transfer (ESIPT) is a fundamental chemical process with several applications. Ultrafast ESIPT involves coupled electronic and atomic motions and has been primarily studied using femtosecond optical spectroscopy. X-ray spectroscopy is particularly useful because it is element-specific and enables direct, individual probes of the proton donating and accepting atoms. In this chapter, I describe a computational study to resolve the ESIPT in 10-Hydroxybenzo[*h*]quinoline (HBQ), an intramolecularly hydrogen bonded compound. Linear-response time-dependent density functional theory LR-TDDFT combined with *ab initio* molecular dynamics (AIMD) and time-resolved X-ray absorption spectroscopy (XAS) computations are used to track the ultrafast excited-state dynamics. These results reveal clear X-ray spectral signatures of coupled electronic and atomic motions during and following ESIPT at the oxygen and nitrogen K-edge paving the way for future experiments at X-ray free electron lasers.

3.1 Introduction

Many technologies and biological functions such as stable white light generation, enzymatic reactions, and several cellular processes rely on efficient energy transfer mediated by ESIPT. [2–9] Ultrafast ESIPT processes occurring on the sub-100 femtosecond (fs) timescale often involve coupled motions of electrons and atoms. The efficiency and speed of an ES-

IPT is dependent on a number of different factors, including the coupling between atomic and electronic degrees of freedom, and the extent of electronic delocalization on the excited state. Model systems serve as important platforms to study the effect of microscopic interactions on ESIPT with experiments and theory. Several model ESIPT systems incorporate intramolecular hydrogen bonding to assist ultrafast isomerization or tautomerization, which can in turn strongly affect the electronic structure of the molecule. The resulting dynamics therefore involve multiple atomic degrees of freedom as well as strong changes in electronic character.

One such model ESIPT system, HBQ, exhibits strong intramolecular hydrogen bonding and undergoes tautomerization following near UV excitation, and has been widely studied by experiments and theory. [10–25] In the electronic ground state, HBQ is energetically stable only in the enol form when dissolved in non-polar solvents. [21, 23] Upon photoexcitation ($S_0 \rightarrow S_1$) in the near UV, [11] the molecule is excited to an enol* state and the proton moves from the oxygen to the nitrogen atom to form the keto* state as shown in Figure 3.1a. The timescale of the barrierless ESIPT on the S_1 state in HBQ has been experimentally determined to be 13 ± 5 fs. [14] Ultrafast transient absorption and fluorescence upconversion experiments have measured coherent vibrational wavepackets in the keto* state which has lifetime of >200 ps. [12–14, 18, 25] Calculations simulating transient absorption experiments reveal a complicated multidimensional potential energy surface with coupled electronic and atomic motions, where vibrational modes are coherently excited by the ESIPT process. [16, 25] While the ultrafast optical experiments provide valuable insights into the ESIPT process in HBQ, they lack the ability to track local electronic changes with atom specificity.

X-ray spectroscopy is ideally suited to track the reorganization of electrons and atoms in condensed media in an atom specific manner. The K-edges of lighter elements like oxygen and nitrogen have been used to study intermolecular hydrogen bonding in liquids and in molecules at equilibrium. [26–29] With the advent of X-ray free electron lasers (XFELs), ultrafast X-ray absorption and emission spectroscopy at transition metal K-edges has become a valuable experimental tool to understand how coupled electronic and atomic motions enable ultrafast

(sub-100 fs) photochemical processes in the condensed phase. In several reports, fs X-ray pulses from XFELs probe time-evolving hydrogen bonding environments following optical excitation. [30, 31] These studies highlight the enormous potential of using ultrafast XAS as a probe of coupled electronic and atomic motion in excited state proton transfer reactions.

In this chapter, I report a computational XAS study coupled with AIMD to predict how transient electronic changes will manifest in a fs XAS measurement of photoinduced ESIPT in HBQ dissolved in a non-polar solvent. Excited state dynamics in HBQ based on LR-TDDFT show how molecular orbital changes around the proton donor (oxygen) and proton acceptor (nitrogen) during and after ESIPT generate distinct time-dependent spectral features in the pre-edge region of the O and N K-edge X-ray spectra. Fourier analysis of the calculated X-ray spectra following ESIPT reveals evidence of backbone vibrations coupled to the changing electronic structure around the proton donor and acceptor sites. This computational work identifies the time-evolving spectral signatures for following ultrafast ESIPT processes using experimental dual-edge O and N K-edge X-ray absorption studies at XFELs following valence excitation.

3.2 Results and Discussion

The LR-TDDFT-based pre-edge regions of the oxygen and nitrogen K-edge XAS spectra are calculated using optimized ground state geometries of the enol and keto tautomers of HBQ and are shown in Figure 3.1 along with the ground state molecular orbitals. Our calculated hydrogen bond and proton donor/acceptor distances of the optimized geometries (see Table B.1 in Appendix B) are consistent with previously published work. [22] The details of the computations are listed in the methods section and in the accompanying Supporting Information (Appendix B). The distinct pre-edge features labeled as B and C result from transitions of the 1s core electrons at the N and O sites and are discussed in detail below. We do not consider higher-lying transitions in the present work as they involve large numbers of molecular orbital pairs, making these transitions challenging to associate with specific molecular parameters. This work uses a mean-field solvent model to simulate the ultrafast

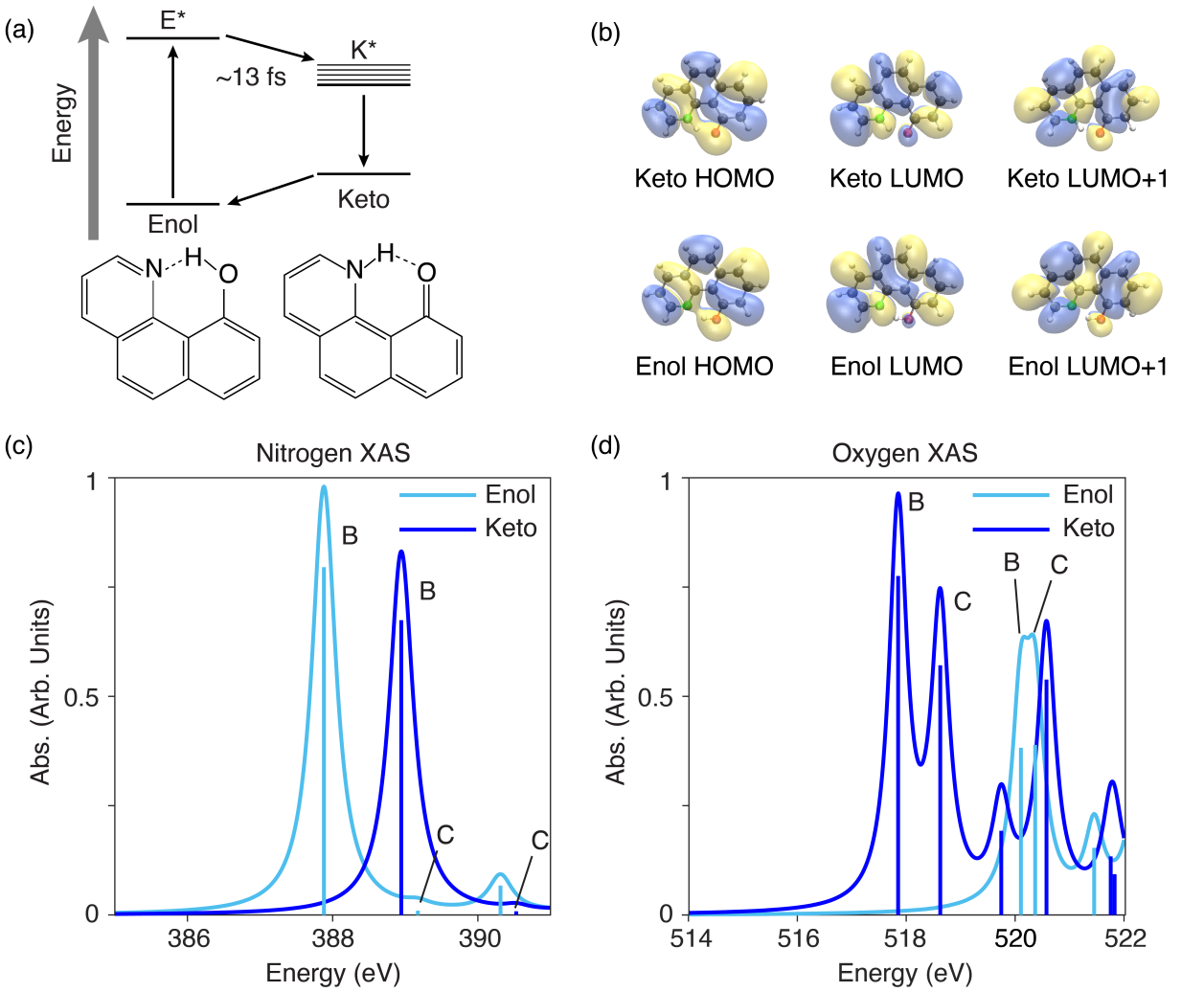

Figure 3.1. (a) Photochemical scheme showing the ultrafast tautomerization of HBQ from the enol* to the keto* form following photoexcitation to the first excited state. (b) Ground state molecular orbitals in HBQ of the HOMO, LUMO, and LUMO+1 showing clear changes around proton donor and acceptor in the different tautomers. All orbitals are plotted with isovalues of $\pm$ 0.008. Nitrogen atom in green, oxygen atom in red. Simulations of ground state nitrogen (c) and oxygen (d) K-edge X-ray absorption spectra. The B and C peaks represent $1s$ to LUMO and LUMO+1 transitions, respectively.

ESIPT process in HBQ dissolved in non-polar solvents. Previous simulations of ultrafast IR spectroscopy have shown that the implicit solvent model is adequate in describing the structure and dynamics of HBQ dissolved in non-polar solvents. [24]

The ground state nitrogen K-edge XAS calculations (Figure 3.1c), show an overall 1.1-1.4 eV blue shift of the spectral features in going from the enol to keto form of HBQ. The most intense feature for both tautomers, labeled B, corresponds to a $1s$ to LUMO transition. The next highest energy peak, labeled peak C, represents a transition from the $1s$ to the LUMO+1 orbital. Higher lying peaks follow as expected, representing transitions from $1s$ to LUMO+2, LUMO+3, etc. There is a large intensity difference between the B and C peaks in Figure 3.1c. A comparison between the LUMO and LUMO+1 orbitals (Figure 3.1b) for both tautomers reveals that the node is closer to the N atom in the LUMO+1 than in the LUMO, decreasing the $1s$ to LUMO+1 transition intensity of the C peak and accounting for the difference in intensities of the B and C peaks. The overall blue shift of 1.1 and 1.4 eV for the B and C features, respectively, between the enol and keto tautomers can also be understood by inspecting the molecular orbitals. Between the enol and keto form, the electron density increases around the nitrogen in the HOMO (see Figure 3.1b) resulting in an increase of the ionization potential of a nitrogen $1s$ electron, and causing the overall blue shift. The calculated spectra in Figure 3.1c compare favorably with the N K-edge spectra of 2-Mercaptopyridine, which has a similar local bonding environment around the N; deprotonation at the N site resulted in a 1.5 eV red shift of peak B and 1.6 eV red shift of peak C. [32]

The calculated O K-edge spectra (Figure 3.1d) also exhibit two strong pre-edge features labeled B and C, that are split by 0.3 eV and 0.8 eV for the enol and keto forms, respectively. As in the nitrogen K-edge XAS, the keto B peak primarily represents a $1s$ to LUMO transition, and the C peak mainly represents a $1s$ to LUMO+1 transition. In contrast, in the enol oxygen K-edge XAS, the B and C features include multiple transitions. The B peak represents a transition of 2/3 $1s$ to LUMO and 1/3 $1s$ to LUMO+1. The C peak represents 2/3 $1s$ to LUMO+1 and 1/3 $1s$ to LUMO. The higher energy peaks for both geometries correspond to transitions into higher energy virtual orbitals (LUMO+2, LUMO+3, etc) and are not the focus of this study. The overall red shift of 2.3 eV for the B peak and 1.7 eV for the C peak in going from the enol to the keto spectrum can be understood in the same

way as the blue shift for the nitrogen K-edge spectra. As the molecular orbitals change between the two tautomers, so does the ionization potential of an oxygen 1s electron. Our calculated spectra in Figure 3.1d compare well to ground state O K-edge calculations of a similar system, malonaldehyde, in which the C=O peak was 2.7 eV red shifted relative to the O–H peak. [33]

A comparison of the calculated N and O K-edge spectra of enol and keto tautomers of HBQ reveals that the position and amplitude of peaks B and C will serve as important spectroscopic observables for monitoring ultrafast ESIPT. As shown above, the blue (red) shifting of the nitrogen (oxygen) K-edge in going from enol to keto measures the overall electron density around the nitrogen (oxygen) atom, and the amplitudes of the B and C peaks are sensitive to the the electronic structure of the unfilled or partially filled molecular orbitals, providing us handles to monitor the coupling of electronic and atomic degrees of freedom during and after ESIPT.

We next calculate time-evolving X-ray spectra at the N and O K-edge following ESIPT. Our excited state molecular dynamics simulations on the S_1 state, which is dominated by the HOMO to LUMO excitation, yield a proton transfer of 14 $\pm$ 6 fs, consistent with previous experimental studies. [14, 18] The average hydrogen bond and proton donor/acceptor distances in the K* MD excited state geometries are consistent with the same distances in the optimized excited state geometries (K*, see Table B.1). The E* geometry (at time 0) matches that of the ground state, with r_{OH} = 1.0 Å. The trajectories of the O$\cdots$H, N$\cdots$H, and N$\cdots$O distances show oscillatory motion in the keto* state demonstrating coherent atomic motion following ESIPT (see Figure B.2 in Appendix B).

To simulate a time-resolved XAS measurement, transient X-ray spectra at the N and O K-edge were computed every $\sim$2.4 fs following HOMO to LUMO excitation for one representative excited state MD trajectory. Further details can be found in the Computational Methods Section. Figure 3.2a shows the excited state molecular geometries prior (0 fs), during (8 fs and 14 fs) and after (84.7 fs) the ultrafast ESIPT, displaying the atomic rearrangement between the proton acceptor and donor sites. Excited state molecular orbitals for

geometries at 0 fs and 84.7 fs demonstrate the electronic rearrangement in the ring backbone as the bond conjugation evolves (see Figure B.3 in Appendix B). The transient N and O K-edge spectra, calculated using the above-mentioned excited state geometries, are shown in Figures 3.2b and 3.2c, respectively.

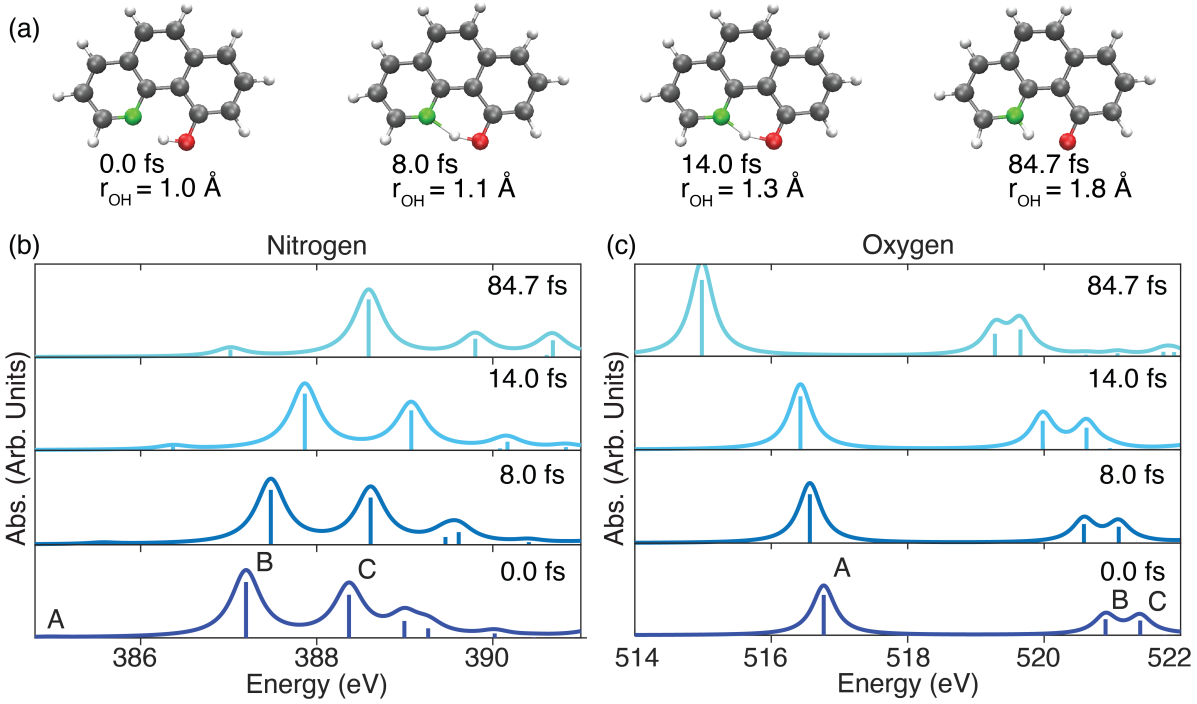

Figure 3.2. (a) Evolution of molecular geometries from an excited state trajectory of HBQ on the S_1 excited state following HOMO to LUMO excitation at 0 fs. Computed excited state nitrogen (b) and oxygen (c) K-edge spectra at the time points shown in (a). The calculated roots are broadened by a 0.4 eV Lorentzian to account for the lifetime broadening at the respective edges.

In the excited state spectra at both N and O K-edges (Figure 3.2b,c), there is a new feature labeled A in addition to the B and C features that were present in the ground state. The 0 fs B (C) feature in Figure 3.2b is red shifted by 0.7 (0.8) eV relative to the ground state enol B (C) feature (Figure 3.1c). The 84.7 fs keto* spectrum shows the B (C) feature is red shifted by 0.3 (0.7) eV with respect to the ground state keto spectrum. In the excited state, there is a blue shift from 0 fs to 84.7 fs for the A, B and C features by 2.0 eV, 1.4 eV,

and 1.4 eV, respectively, compared to the ground state blue shifts from enol to keto of 1.1 eV and 1.4 eV for the B and C features, respectively.

In the nitrogen excited state XAS, the A peak grows in during the proton transfer, increasing by a factor of 15 following ESIPT, and the keto* C peak at 84.7 fs is half as intense as at early times. Figure B.3 in Appendix B shows the excited state molecular orbitals at 0 fs and 84.7 fs for each spectral feature. Due to a node next to the nitrogen in the dominant final state orbital of the A peak transition, there is a low transition intensity for the A peak at 0 fs. At 84.7 fs, the K* dominant final state orbital of the A peak shows greater electron density around the nitrogen. Similarly, the presence of a node closer to the nitrogen in the dominant final state orbital of the C peak at 84.7 fs than at 0 fs contributes to its decrease in transition intensity. The time-evolving electronic structure at the N atom in HBQ during ESIPT is reported on by the A and C peak intensities and overall blue shift in the nitrogen transient XAS spectrum.

In the oxygen excited state XAS (Figure 3.2c), the 0 fs enol* B (C) peak is blue shifted by 0.8 (1.0) eV with respect to the ground state oxygen enol spectrum. The 84.7 fs keto* B (C) peak is blue shifted by 1.4 (1.0) eV with respect to the ground state keto spectrum. In the oxygen excited state spectrum from 0 to 84.7 fs, the A, B, and C peaks red shift by 1.8 eV, 1.6 eV, and 1.7 eV compared to the ground state red shifts from enol to keto of 2.3 eV and 1.7 eV for the B and C peaks, respectively. As in the nitrogen spectra, the electronic dynamics as a result of the ESIPT are reported on by the position and intensity of the A peak in particular. The stronger relative intensity of the oxygen A peak compared to the nitrogen A peak correlates with the greater electron density surrounding the oxygen atom compared to the nitrogen in the excited state molecular orbitals.

Figure 3.3a plots the time evolution of the N K-edge X-ray spectrum on the excited state following HOMO to LUMO excitation in HBQ. Large spectral changes in the peaks A, B, and C occur in the first $\sim$20 fs, while the ultrafast ESIPT takes place. Following the proton transfer, the positions of the A, B and C spectral features continue to oscillate. Figure 3b plots the change in the spectral position of feature B, and the oscillations are

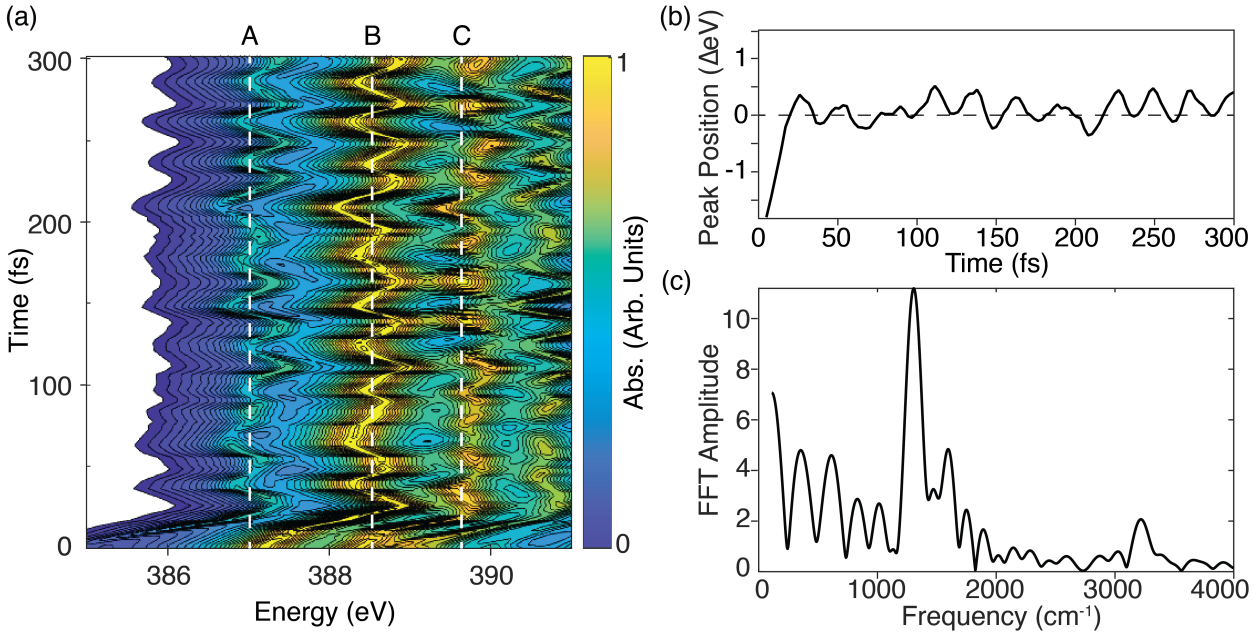

Figure 3.3. (a) Calculated ultrafast transient XAS at the nitrogen K-edge for 300 fs following HOMO to LUMO excitation, plotted on a logarithmic scale and normalized. Contour levels are drawn every 3% after a minimum cutoff value (in white). Dashed vertical lines denote the long-time average of each peak at 387.0 eV, 388.5 eV, and 389.6 eV. (b) The change in frequency of the peak of spectral feature B with reference to 388.5 eV (from contour map in (a)) as a function of time. (c) The amplitude of the Fourier transform of the plot in (b). A hyperbolic tangent windowing function was applied before Fourier transforming (see Figure B.5 in Appendix B).

seen clearly. The results of a Fourier analysis of the oscillations are shown in Figure 3.3c. The Fourier analysis reflects the impact of atomic motions on the local electronic structure around the nitrogen in the excited state. A similar analysis of the spectral feature A is performed and shown in Figures B.5(a,c) in Appendix B. Figure 3.3c reveals that high frequencies at 1306 cm^{-1}, 1597 cm^{-1} and 3217 cm^{-1} and lower frequencies at 354 cm^{-1} and 611 cm^{-1} modulate the spectral position of peak B in the N K-edge spectrum following ESIPT. To understand how these frequencies modulate the electronic structure at the N K-edge, we compare them to normal modes of the K* state, computed from excited state frequency calculations (See Tables B.3 and B.4 in Appendix B). The comparison shows

that the observed frequencies in Figure 3.3c are similar in frequency to K* modes which modulate the O$\cdots$H distance especially. For example, the measured frequency at 354 cm^{-1} corresponds to a ring breathing mode at 375 cm^{-1}, and the frequencies at 1306 cm^{-1} and 1597 cm^{-1} correspond to K* N–H bending and wagging modes, which have similar frequencies and modulate the O$\cdots$H distance. Since the proton in HBQ is shared between the O and the N, the modulation of the O$\cdots$H distance clearly impacts the local electronic structure around the N atom.

The time-evolution of the calculated O K-edge X-ray spectra following HOMO to LUMO excitation in HBQ is shown in Figure 3.4a. The spectral feature A is seen to clearly oscillate following proton transfer (after $\sim$14 fs) when plotting the change in position of the peak as a function of time in Figure 3.4b. We perform a Fourier analysis of the oscillations, as shown in Figure 3.4c, with the most intense feature at 1654 cm^{-1}. To understand how the observed frequencies modulate the electronic structure at the O K-edge, we compare them to normal modes of the K* state computed from excited state frequency calculations. The strongest feature corresponds to the K* carbonyl stretch and N–H bending mode at 1747 cm^{-1}. Lower frequencies resolved in the Fourier spectrum such as at 297 cm^{-1} correspond to an excited state ring breathing mode, perhaps at 250 cm^{-1}. (See Table B.5 in Appendix B for more frequencies and mode descriptions). The splitting distance between the B and C peaks in the time-evolving O K-edge spectrum also oscillates in phase with the A peak, varying from an energy difference of 0.2 eV to 0.6 eV (Figure B.5(b,d) in Appendix B). As HBQ evolves in the excited K* state with coherent atomic motion, close-lying molecular orbitals shift in energy in a periodic manner, which contributes to the differences in peak position. The positions of the B and C peaks communicate that the electronic rearrangement in the involved molecular orbitals is closely related to the atomic rearrangement occurring during ESIPT and in the K* state. As the atoms fluctuate, so does the electronic structure; these fluctuations are reflected in the oscillating peak positions in the transient XAS. Similar to the N K-edge spectra, the frequencies modulating the proton donor-acceptor distance in HBQ impact the local electronic structure around the O atom and are reflected in the spectral oscillations

seen in the O K-edge spectra.

We calculated transient X-ray spectra at the O K-edge using 20 representative trajectories (Figure B.2 in Appendix B) to determine the robustness of the calculated spectral signatures of ESIPT. The long-time average energy of the A peak position for 20 trajectories, at 515.3 eV, compares favorably to the long-time average position for our single trajectory in Figure 3.4, also at 515.3 eV. Furthermore, the energy of the oxygen A peak at 0 fs is 516.8 eV for both the spectrum of a single trajectory and the averaged spectrum. The Fourier transform of the peak position of spectral feature A from the averaged X-ray spectra is plotted in Figure 3.4c (dashed line) and shows frequencies that align well with the frequencies from the single trajectory, although there are some differences in relative amplitudes. Particularly noticeable are the amplitudes of the peaks at 775 cm^{-1} and 1467 cm^{-1} compared to the most intense peak at 1654 cm^{-1}. (See Table B.5 in the Supplementary Information to compare these modes to the harmonic frequencies calculated for the K* form of HBQ). The preservation of oscillations after averaging spectra from many trajectories confirms that the pre-edge features in the K-edge X-ray spectra of the proton donor and acceptor atoms are excellent reporters of coupled electronic and atomic motions during ultrafast ESIPT.

It is worthwhile to compare the observed coherent oscillations and corresponding frequencies in the X-ray spectra shown in Figures 3.3 and 3.4 to those seen previously. Ultrafast transient absorption experiments have measured lower frequencies at 237 cm^{-1}, 392 cm^{-1}, 550 cm^{-1}, 692 cm^{-1}, and 794 cm^{-1}, which correspond to skeletal deformations modulating the O$\cdots$N distance in HBQ. [12, 13, 25] A recent study claims that the observation of the 794 cm^{-1} frequency in a transient absorption spectrum is evidence of non-Born Oppenheimer dynamics during ESIPT in HBQ. [25] Interestingly, our study, which treats the ESIPT as a downhill excited state process, observes the frequency at 775 cm^{-1} in the O K-edge spectrum. Figures 3.3 and 3.4 also display many frequencies below 500 cm^{-1} similar to previous studies. The important distinction between our X-ray calculations and previous studies is the fact that we can conclusively identify coherent atomic motions coupled to local electronic changes around the proton donor and acceptor atoms. We expect the observed vibrational

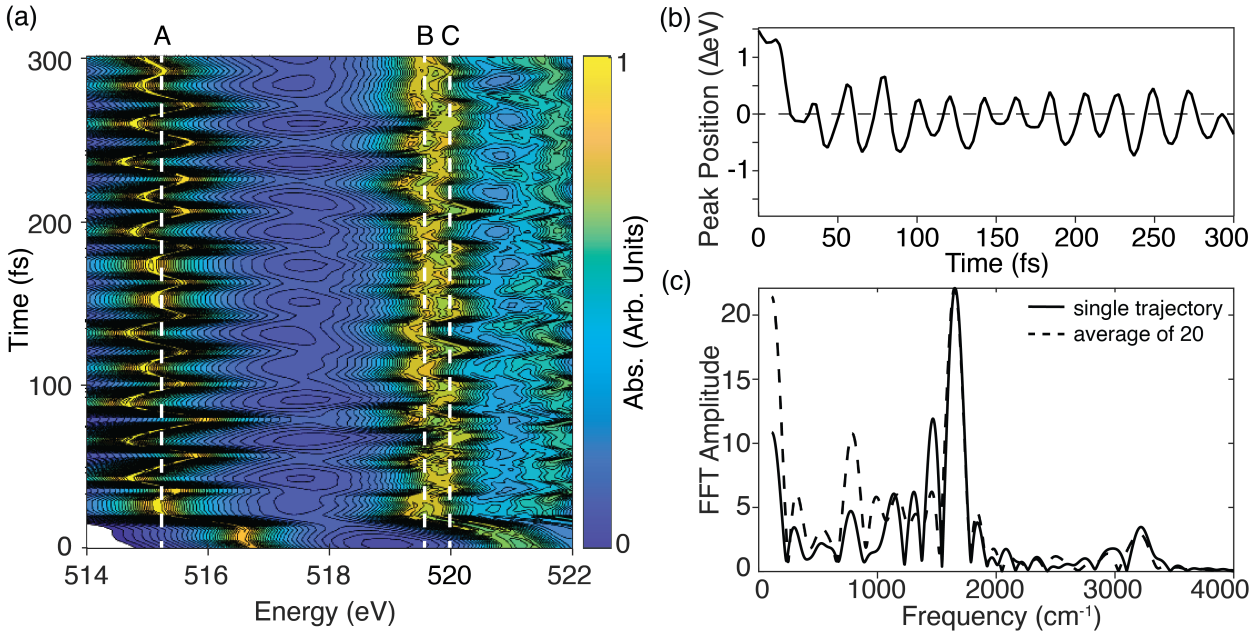

Figure 3.4. (a) Calculated ultrafast transient XAS at the oxygen K-edge for 300 fs following HOMO to LUMO excitation, plotted on a logarithmic scale and normalized. Contour levels are drawn every 3% after a minimum cutoff value (in white). Dashed vertical lines denote the long-time average of each peak at 515.3 eV, 519.6 eV, and 520.0 eV. (b) The change in frequency of the peak of spectral feature A with reference to 515.3 eV (from contour map in (a)) as a function of time. (c) The amplitude of the Fourier transform of the plot in (b), compared to the Fourier transform amplitude of the A feature in an averaged spectrum, which has been scaled by a factor of 2.5 (see Figure B.4 in Appendix B). A hyperbolic tangent windowing function was applied before Fourier transforming (see Figure B.5 in Appendix B).

modes to be coupled to one another in the excited state as they are in the ground electronic state of HBQ, [24] and non-equilibrium vibrational dynamics to play a role in the relaxation of the K* state.

In summary, this computational study reveals time-evolving spectral signatures in the $1s$ core-level spectra of proton donating and accepting atoms providing a unique window into coupled electronic and atomic motions during ultrafast ESIPT. In this study, our model system, HBQ, was dissolved in a non-polar solvent. We expect the solvent will play an important role in proton transfer dynamics for molecular systems dissolved in polar hydrogen-bonding

solvents, and transient XAS calculations will have to take explicit solute-solvent interactions into account as has been shown previously. [34] The calculations described in this chapter are necessary precursors to predict and analyze transient ultrafast X-ray experiments, and nonlinear X-ray experiments such as two color X-ray pump X-ray probe, [35] and resonant stimulated X-ray Raman spectroscopy of ESIPT processes in solution at XFELs. [36–38] We expect that the upcoming upgrades to the Linac Coherent Light Source (LCLS) and corresponding instrumentation will result in the necessary high spectral resolution and the desired signal to noise to measure wavepacket dynamics following ESIPT in HBQ and similar systems.

3.3 Computational Methods

All calculations presented in this paper were performed with the open-source NWChem computational chemistry program. [39, 40]. Ground state enol and keto geometries were optimized using the B3LYP exchange-correlation functional [41, 42] and the all-electron def2-TZVP basis set. [43] The basis sets were obtained from the Environmental Molecular Sciences Laboratory (EMSL) Basis Set Exchange. [44–46] All calculations used the same exchange-correlation functional and basis set. The solvation environment was treated implicitly via the COnductor-like Screening MOdel (COSMO) [47, 48] with a dielectric constant (ϵ) of 2.50 to simulate the effect of the tetrachloroethylene (PCE) solvent.

Although only the enol form of HBQ is stable in the ground state, the potential energy curve along the ground state proton transfer reaction coordinate also has a very shallow minimum at the keto geometry, allowing us to converge the keto form. LR-TDDFT-based nitrogen and oxygen K-edge XAS were computed on both ground state geometries (enol and keto) with the restricted window approach [49] as implemented in NWChem. The resulting spectra are shown in Figures 3.1c and d, where we have used a Lorentzian life-time broadening of 0.4 eV.

Excited state dynamics [50] based on LR-TDDFT [51] were run to simulate ultrafast ESIPT and subsequent dynamics in HBQ on the S_1 excited state (dominated by the HOMO

to LUMO photoexcitation). A nuclear time step of 10 a.u. ($\sim$ 0.24 fs) was used for all the excited-state trajectories. No thermostat was used. In total, we ran 25 trajectories using a starting geometry from a vertical excitation and different initial velocities randomly selected from the Maxwell-Boltzmann distribution at room temperature (298.15 K). Surface hopping methods were not required as the S_1 and S_2 excited states are energetically well separated (by $\geq$ 0.5 eV) and the proton transfer dynamics occurs completely on the S_1 excited state. Neither nuclear quantum effects [52] nor explicit dephasing effects [53] were included in our dynamics simulations. Excited state frequencies were computed numerically based on analytical gradients at the LR-TDDFT level. [51]

Using the excited state geometries from a representative trajectory (Figure B.2b in Appendix B) at selected time points, transient nitrogen and oxygen K-edge XAS were computed using the excited-state molecular orbitals at each point. These were accomplished in three steps for each of the selected time points. First, the self-consistent field (SCF) was converged for each geometry at the selected time points to obtain the ground state molecular orbitals. Second, using the converged molecular orbitals in Step 1, the occupancies of the alpha HOMO and LUMO orbitals were swapped and the SCF re-converged to simulate the HOMO-LUMO photoexcitation. Since the S_1 excited state is dominated by the HOMO to LUMO photoexcitation, our approach captures the reference excited-state determinant sufficiently accurately. Third, XAS spectra, as described earlier, were computed using the excited-state molecular orbitals obtained in Step 2. The resulting broadened spectra are shown in Figures 3.2-3.4.

BIBLIOGRAPHY

[1] C. M. Loe, C. Liekhus-Schmaltz, N. Govind, and M. Khalil, "Spectral signatures of ultrafast excited-state intramolecular proton transfer from computational multi-edge transient x-ray absorption spectroscopy," *The Journal of Physical Chemistry Letters*, vol. 12, pp. 9840–9847, Oct. 2021.

[2] S. Park, E. K. Ji, H. K. Se, J. Seo, K. Chung, S. Y. Park, D. J. Jang, B. M. Medina, J. Gierschner, and Y. P. Soo, "A White-Light-Emitting Molecule: Frustrated Energy Transfer Between Constituent Emitting Centers," *The Journal of the American Chemical Society*, vol. 131, pp. 14043–14049, 2009.

[3] G. R. Han, D. Hwang, S. Lee, J. W. Lee, E. Lim, J. Heo, and S. K. Kim, "Shedding New Light on an Old Molecule: Quinophthalone Displays Uncommon N-to-O Excited State Intramolecular Proton Transfer (ESIPT) Between Photobases," *Scientific Reports - Nature*, vol. 7, p. 3863, 2017.

[4] S. J. Lim, J. Seo, and S. Y. Park, "Photochromic Switching of Excited-State Intramolecular Proton-Transfer (ESIPT) Fluorescence: A Unique Route to High-Contrast Memory Switching and Nondestructive Readout," *The Journal of the American Chemical Society*, vol. 128, pp. 14542–14547, 2006.

[5] J. E. Kwon and S. Y. Park, "Advanced Organic Optoelectronic Materials: Harnessing Excited-State Intramolecular Proton Transfer (ESIPT) Process," *Advanced Materials*, vol. 23, pp. 3615–3642, 2011.

[6] W. H. Chen, Y. Xing, and Y. Pang, "A Highly Selective Pyrophosphate Sensor Based on ESIPT Turn-On in Water," *Organic Letters*, vol. 13, no. 6, pp. 1362–1365, 2011.

[7] A. C. Sedgwick, L. Wu, H. H. Han, S. D. Bull, X. P. He, T. D. James, J. L. Sessler, B. Z. Tang, H. Tian, and J. Yoon, "Excited-State Intramolecular Proton-Transfer (ESIPT) Based Fluorescence Sensors and Imaging Agents," *Chemical Society Reviews*, vol. 47, pp. 8842–8880, 2018.

[8] V. S. Padalkar and S. Seki, "Excited-State Intramolecular Proton-Transfer (ESIPT)-Inspired Solid State Emitters," *Chemical Society Reviews*, vol. 45, pp. 169–202, 2016.

[9] J. Zhao, S. Ji, Y. Chen, H. Guo, and P. Yang, "Excited State Intramolecular Proton Transfer (ESIPT): From Principal Photophysics to the Development of New Chromophores and Applications in Fluorescent Molecular Probes and Luminescent Materials," *Physical Chemistry Chemical Physics*, vol. 14, pp. 8803–8817, 2012.

[10] M. L. Martinez, W. C. Cooper, and P.-T. Chou, "A Novel Excited-State Intramolecular Proton Transfer Molecule, 10-Hydroxybenzo[*h*]quinoline," *Chemical Physics Letters*, vol. 193, no. 1-3, pp. 151–154, 1992.

[11] P.-T. Chou, Y.-C. Chen, W.-S. Yu, Y.-H. Chou, C.-Y. Wei, and Y.-M. Cheng, "Excited-State Intramolecular Proton Transfer in 10-Hydroxybenzo[*h*]quinoline," *The Journal of Physical Chemistry A*, vol. 105, pp. 1731–1740, Mar. 2001.

[12] S. Takeuchi and T. Tahara, "Coherent Nuclear Wavepacket Motions in Ultrafast Excited-State Intramolecular Proton Transfer: Sub-30-fs Resolved Pump–Probe Absorption Spectroscopy of 10-Hydroxybenzo[*h*]quinoline in Solution," *The Journal of Physical Chemistry A*, vol. 109, pp. 10199–10207, Nov. 2005.

[13] C. Schriever, M. Barbatti, K. Stock, A. J. Aquino, D. Tunega, S. Lochbrunner, E. Riedle, R. de Vivie-Riedle, and H. Lischka, "The Interplay of Skeletal Deformations and Ultrafast Excited-State Intramolecular Proton Transfer: Experimental and Theoretical Investigation of 10-Hydroxybenzo[*h*]quinoline," *Chemical Physics*, vol. 347, pp. 446–461, 2008.

[14] C. H. Kim and T. Joo, "Coherent Excited State Intramolecular Proton Transfer Probed by Time-Resolved Fluorescence," *Physical Chemistry Chemical Physics*, vol. 11, no. 44, pp. 10266–10269, 2009.

[15] B. K. Paul and N. Guchhait, "TD-DFT Investigation of the Potential Energy Surface for Excited-State Intramolecular Proton Transfer (ESIPT) Reaction of 10-Hydroxybenzo[*h*]quinoline: Topological (AIM) and Population (NBO) Analysis of the Intramolecular Hydrogen Bonding Interaction," *Journal of Luminescence*, vol. 131, pp. 1918–1926, 2011.

[16] M. Higashi and S. Saito, "Direct Simulation of Excited-State Intramolecular Proton Transfer and Vibrational Coherence of 10-Hydroxybenzo[*h*]quinoline in Solution," *The Journal of Physical Chemistry Letters*, vol. 2, pp. 2366–2371, 2011.

[17] X. Zhao and M. Chen, "A TDDFT Study on the Singlet and Triplet Excited-State Hydrogen Bonding and Proton Transfer of 10-Hydroxybenzo[*h*]quinoline (HBQ) and 7,9-Diiodo-10-hydroxybenzo[*h*]quinoline (DIHBQ)," *Chemical Physics Letters*, vol. 512, pp. 35–39, 2011.

[18] J. Lee, C. H. Kim, and T. Joo, "Active Role of Proton in Excited State Intramolecular Proton Transfer Reaction," *The Journal of Physical Chemistry A*, vol. 117, pp. 1400–1405, 2013.

[19] S. Chai and S.-L. Cong, "Excited State Intramolecular Proton Transfer and Substituent Effect of 10-Hydroxybenzo[*h*]quinoline: A Time-Dependent Density Functional Theory Study," *Computational and Theoretical Chemistry*, vol. 1034, pp. 80–84, 2014.

[20] M. Zhou, J. Zhao, Y. Cui, Q. Wang, Y. Dai, P. Song, and L. Xia, "Theoretical Study on the Excited-State Intramolecular Proton-Transfer Reaction of 10-Hydroxybenzo[*h*]quinoline in Methanol and Cyclohexane," *Journal of Luminescence*, vol. 161, pp. 1–6, May 2015.

[21] S. Hristova, G. Dobrikov, F. S. Kamounah, S. Kawauchi, P. E. Hansen, V. Deneva, D. Nedeltcheva, and L. Antonov, "10-Hydroxybenzo[*h*]quinoline: Switching Between Single- and Double-Well Proton Transfer Through Structural Modifications," *RSC Advances*, vol. 5, pp. 102495–102507, 2015.

[22] W. Chansen, R. Salaeh, C. Prommin, K. Kerdpol, R. Daengngern, and N. Kungwan, "Theoretical Study on Influence of Geometry Controlling Over the Excited-State Intramolecular Proton Transfer of 10-Hydroxybenzo[*h*]quinoline and its Derivatives," *Computational and Theoretical Chemistry*, vol. 1113, pp. 42–51, 2017.

[23] H. Marciniak, S. Hristova, V. Deneva, F. S. Kamounah, P. E. Hansen, S. Lochbrunner, and L. Antonov, "Dynamics of Excited State Proton Transfer in Nitro Substituted 10-Hydroxybenzo[*h*]quinolines," *Physical Chemistry Chemical Physics*, vol. 19, no. 39, pp. 26621–26629, 2017.

[24] M. Balasubramanian, A. Reynolds, T. J. Blair, and M. Khalil, "Probing Ultrafast Vibrational Dynamics of Intramolecular Hydrogen Bonds with Broadband Infrared Pump-Probe Spectroscopy," *Chemical Physics*, vol. 519, pp. 38–44, Mar. 2019.

[25] J. W. Kim, C. H. Kim, C. Burger, M. Park, M. F. Kling, D. E. Kim, and T. Joo, "Non-Born–Oppenheimer Molecular Dynamics Observed by Coherent Nuclear Wave Packets," *The Journal of Physical Chemistry Letters*, vol. 11, pp. 755–761, 2020.

[26] M. Ekimova, W. Quevedo, Ł. Szyc, M. Iannuzzi, P. Wernet, M. Odelius, and E. T. Nibbering, "Aqueous Solvation of Ammonia and Ammonium: Probing Hydrogen Bond Motifs with FT-IR and Soft X-Ray Spectroscopy," *Journal of the American Chemical Society*, vol. 139, pp. 12773–12783, 2017.

[27] M. Ekimova, M. Kubin, M. Ochmann, J. Ludwig, N. Huse, P. Wernet, M. Odelius, and E. T. Nibbering, "Soft X-Ray Spectroscopy of the Amine Group: Hydrogen Bond Motifs in Alkylamine/Alkylammonium Acid–Base Pairs," *The Journal of Physical Chemistry B*, vol. 122, pp. 7737–7746, Aug. 2018.

[28] M. Prémont-Schwarz, S. Schreck, M. Iannuzzi, E. T. Nibbering, M. Odelius, and P. Wernet, "Correlating Infrared and X-Ray Absorption Energies for Molecular-Level Insight into Hydrogen Bond Making and Breaking in Solution," *The Journal of Physical Chemistry B*, vol. 119, pp. 8115–8124, 2015.

[29] A. Pietzsch, F. Hennies, P. S. Miedema, B. Kennedy, J. Schlappa, T. Schmitt, V. N. Strocov, and A. Föhlisch, "Snapshots of the Fluctuating Hydrogen Bond Network in Liquid Water on the Sub-Femtosecond Timescale With Vibrational Resonant Inelastic X-Ray Scattering," *Physical Review Letters*, vol. 114, pp. 088302–1–5, 2015.

[30] S. Eckert, J. Norell, P. S. Miedema, M. Beye, M. Fondell, W. Quevedo, B. Kennedy, M. Hantschmann, A. Pietzsch, B. E. Van Kuiken, *et al.*, "Ultrafast Independent N–H and N–C Bond Deformation Investigated with Resonant Inelastic X-Ray Scattering," *Angewandte Chemie International Edition*, vol. 56, pp. 6088–6092, 2017.

[31] Z.-H. Loh, G. Doumy, C. Arnold, L. Kjellsson, S. H. Southworth, A. Al Haddad, Y. Kumagai, M. F. Tu, P. J. Ho, A. M. March, *et al.*, "Observation of the Fastest Chemical Processes in the Radiolysis of Water," *Science*, vol. 367, pp. 179–182, 2020.

[32] S. Eckert, P. S. Miedema, W. Quevedo, B. O'Cinneide, M. Fondell, M. Beye, A. Pietzsch, M. Ross, M. Khalil, and A. Föhlisch, "Molecular Structures and Protonation State of 2-Mercaptopyridine in Aqueous Solution," *Chemical Physics Letters*, vol. 647, pp. 103–106, 2016.

[33] N. H. List, A. L. Dempwolff, A. Dreuw, P. Norman, and T. J. Martínez, "Probing Competing Relaxation Pathways in Malonaldehyde with Transient X-Ray Absorption Spectroscopy," *Chemical Science*, vol. 11, pp. 4180–4193, 2020.

[34] J. Norell, S. Eckert, B. E. Van Kuiken, A. Föhlisch, and M. Odelius, "*Ab Initio* Simulations of Complementary K-Edges and Solvatization Effects for Detection of Proton Transfer in Aqueous 2-Thiopyridone," *The Journal of Chemical Physics*, vol. 151, p. 114117, 2019.

[35] D. R. Nascimento, Y. Zhang, U. Bergmann, and N. Govind, "Near-edge x-ray absorption fine structure spectroscopy of heteroatomic core-hole states as a probe for nearly indistinguishable chemical environments," *The Journal of Physical Chemistry Letters*, vol. 11, no. 2, pp. 556–561, 2020.

[36] D. Healion, Y. Zhang, J. D. Biggs, N. Govind, and S. Mukamel, "Entangled valence electron–hole dynamics revealed by stimulated attosecond x-ray raman scattering," *The Journal of Physical Chemistry Letters*, vol. 3, no. 17, pp. 2326–2331, 2012.

[37] S. Mukamel, D. Healion, Y. Zhang, and J. D. Biggs, "Multidimensional attosecond resonant x-ray spectroscopy of molecules: Lessons from the optical regime," *Annual Review of Physical Chemistry*, vol. 64, pp. 101–127, 2013.

[38] S. M. Cavaletto, D. R. Nascimento, Y. Zhang, N. Govind, and S. Mukamel, "Resonant Stimulated X-Ray Raman Spectroscopy of Mixed-Valence Manganese Complexes," *The Journal of Physical Chemistry Letters*, vol. 12, pp. 5925–5931, 2021.

[39] M. Valiev, E. J. Bylaska, N. Govind, K. Kowalski, T. P. Straatsma, H. J. Van Dam, D. Wang, J. Nieplocha, E. Apra, T. L. Windus, *et al.*, "Nwchem: A comprehensive and scalable open-source solution for large scale molecular simulations," *Computer Physics Communications*, vol. 181, no. 9, pp. 1477–1489, 2010.

[40] E. Aprà, E. J. Bylaska, W. A. De Jong, N. Govind, K. Kowalski, T. P. Straatsma, M. Valiev, H. J. Van Dam, Y. Alexeev, J. Anchell, *et al.*, "NWChem: Past, Present, and Future," *The Journal of Chemical Physics*, vol. 152, no. 18, pp. 1–26, 2020.

[41] A. D. Becke, "Density-functional exchange-energy approximation with correct asymptotic behavior," *Physical Review A*, vol. 38, pp. 3098–3100, 1988.

[42] C. Lee, W. Yang, and R. G. Parr, "Development of the colle-salvetti correlation-energy formula into a functional of the electron density," *Physical Review B*, vol. 37, pp. 785–789, 1988.

[43] F. Weigend and R. Ahlrichs, "Balanced basis sets of split valence, triple zeta valence and quadruple zeta valence quality for h to rn: Design and assessment of accuracy," *Physical Chemistry Chemical Physics*, vol. 7, pp. 3297–3305, 2005.

[44] D. Feller, "The role of databases in support of computational chemistry calculations," *Journal of Computational Chemistry*, vol. 17, pp. 1571–1586, 1996.

[45] K. L. Schuchardt, B. T. Didier, T. Elsethagen, L. Sun, V. Gurumoorthi, J. Chase, J. Li, and T. L. Windus, "Basis set exchange: A community database for computational sciences," *Journal of Chemical Information and Modeling*, vol. 47, pp. 1045–1052, 2007.

[46] B. P. Pritchard, D. Altarawy, B. Didier, T. D. Gibsom, and T. L. Windus, "A new basis set exchange: An open, up-to-date resource for the molecular sciences community," *Journal of Chemical Information and Modeling*, vol. 59, pp. 4814–4820, 2019.

[47] A. Klamt and G. Schüürmann, "COSMO: A new approach to dielectric screening in solvents with explicit expressions for the screening energy and its gradient," *Journal of the Chemical Society, Perkin Transactions 2*, vol. 0, no. 5, pp. 799–805, 1993.

[48] D. M. York and M. Karplus, "A Smooth Solvation Potential Based on the Conductor-Like Screening Model," *The Journal of Physical Chemistry A*, vol. 103, pp. 11060–11079, Dec. 1999.

[49] K. Lopata, B. E. Van Kuiken, M. Khalil, and N. Govind, "Linear-Response and Real-Time Time-Dependent Density Functional Theory Studies of Core-Level Near-Edge X-Ray Absorption," *Journal of Chemical Theory and Computation*, vol. 8, pp. 3284–3292, Sep. 2012.

[50] S. A. Fischer, T. W. Ueltschi, P. Z. El-Khoury, A. L. Mifflin, W. P. Hess, H.-F. Wang, C. J. Cramer, and N. Govind, "Infrared and Raman spectroscopy from *Ab Initio* molecular dynamics and static normal mode analysis: The CH region of DMSO as a case study," *The Journal of Physical Chemistry B*, vol. 120, pp. 1429–1436, 2016.

[51] D. W. Silverstein, N. Govind, H. J. van Dam, and L. Jensen, "Simulating one-photon absorption and resonance raman scattering spectra using analytical excited state energy gradients within time-dependent density functional theory," *Journal of Chemical Theory and Computation*, vol. 9, no. 12, pp. 5490–5503, 2013.

[52] T. E. Markland and M. Ceriotti, "Nuclear quantum effects enter the mainstream," *Nature Reviews Chemistry*, vol. 2, no. 3, pp. 1–14, 2018.

[53] S. Mukamel, *Principles of Nonlinear Optical Spectroscopy*. Oxford University Press on Demand: Oxford, U.K., 1999.

Chapter 4

DEVELOPMENT AND IMPLEMENTATION OF 2D VE

The purpose of this chapter is to serve as a detailed reference and guide for future users and developers of the 2D VE experiment. It is my aim to both explain the importance of each component in the experiment and to provide a practical guide for setting up and successfully performing 2D VE experiments for someone who is already familiar with a multidimensional or time-resolved spectroscopy lab. This will also aid in the development of new variations and improvements to VE experiments. This chapter will cover general experimental considerations, how to set up for a 2D VE experiment, electronic settings particular to our 2D VE setup, a discussion of solvent effects in 2D VE, and some other troubleshooting challenges that have been encountered. In detailing the quirks and pitfalls of a 2D VE experiment, I hope that future members of the group are able to spend more time using this knowledge to do science rather than re-learning how to make a VE experiment work.

Section 2.2 and Fig. 2.2 cover the general layout and purpose of the VE experiment. This section will provide a more detailed overview of the experiment that is necessary to understand when performing alignment and optimization in the lab. All experiments start with a Ti-Sapphire amplifier from Coherent (Astrella), which is pumped with 532 nm pulses (Coherent Revolution) and seeded with 800 nm pulses from an oscillator (Coherent Vitara). The amplified output pulses are centered at 800 nm with a FWHM bandwidth of $\approx$ 35 nm, are 32 fs long (at the fastest, depending on how recently a technician tuned the Astrella), are pulsed at 1 kHz and have an energy of 7-7.5 mJ per pulse. The output pulses are split with two fused silica beamsplitters after the output to be used in several different lines that generate various wavelengths for use in VE experiments.

A 3 mJ portion is sent to an optical parametric amplifier (OPA, TOPAS-Prime from Light Conversion) which generates two near-infrared pulses. See Appendix D for more details on the function of an OPA. The TOPAS is connected to a difference frequency generation module (DFG, also from Light Conversion) and both are controlled by the same software. The DFG uses a nonlinear crystal such as KTA (Potassium Titanyl Arsenate) or $AgGaS_2$ to take the difference in frequency between overlapped near-infrared pulses to generate mid-infrared (MIR) light. The MIR light is overlapped with a CW HeNe laser to be able to align it to the sample area. It then passes through a Mach-Zehnder interferometer. The "bright" output (one beamsplitter transmission and one reflection for each arm) is used to generate the delay between MIR pump pulses in a 2D VE experiment, because both pulses in the bright output are phase-matched. The "dark" output (two beamsplitter transmissions for one arm, and two reflections for the other) of the interferometer is used to keep track of the delay between MIR pump pulses. The maximum destructive interference of these arms corresponds to the time where there is maximum constructive interference in the bright output, which is the point where both arms are perfectly overlapped in time ($\tau_1 = 0$).

A second arm of the HeNe only (no MIR overlapped with it) is also sent through the interferometer. It traces the same path as the MIR/HeNe line, but vertically offset by roughly one inch. The dark output is blocked after the interferometer, and the bright arm is detected by two photodiodes to precisely track the delay between MIR pump pulses. Reference 1 provides a detailed description of this "fast scanning" method. Briefly, the HeNe beam is polarized to 45° before entering the interferometer. One arm is set to a circular polarization inside of the interferomter. They are recombined and pass through a polarizing beamsplitter cube to separate S and P (vertical and horizontal) polarizations. The S component is detected by one photodiode and the P by the other. As the delay stage is scanned to change the τ_1 delay during an experiment, the oscillating interference of the differently polarized HeNe arms can be fit to a circle in LabVIEW. The half-period of a HeNe wave (632.8 nm / 2 = 316.4 nm = 1.055 fs) dictates the time resolution for tracking τ_1. During an experiment, data are binned according to τ_1 delay. The width of one time bin is 1.055 fs. As the incoming

HeNe tracking data are fit to the circle, if the quadrant changes between II and III or I and IV, the bin changes by ±1.

A second portion (<300 µJ) of the Astrella output is focused with a 1500 mm focal length concave spherical mirror. After the focus, there are five fused silica (FS) plates. The focused 800 nm light is spectrally broadened via self-phase modulation (SPM) and then frequency doubled with a type I beta barium borate (BBO) crystal. It is temporally compressed to ≈100 fs with a prism compressor before being recollimated and sent to the sample area. This is used as the broadband near-UV probe pulse in a VE experiment. It can also be used as the pump in other kinds of time-resolved spectroscopy experiments.

4.1 Experimental Considerations for 2D VE

By nature, a multicolor, third-order experiment such as 2D VE produces a very weak signal since the third order nonlinear response is the signal of interest, and there are small absoprtion cross sections and overlap between electronic and vibrational states. Fortunately, there are some options to consider for improving the 2D VE signal. Choosing a system with similar vibrational and electronic absorption cross sections will make it easier to find a concentration of sample that gives a signal in the thin sample limit, and will generally improve signal strength. Depending on the solvent, it is possible to encounter a long-lived heating response of the solvent. We have found this to be more likely in protic solvents such as formamide and methanol (Section 4.4). In aprotic solvents such as anhydrous CCl_4 a heating signal has not been observed. Transparency of the solvent in the infrared pump region is also important to consider, especially if there is a large mismatch in infrared and visible molar absorptivities. Choose a solvent with as flat and low of a background in the infrared pump region as possible. If there are vibrational overtones or combination bands that are resonant with the infrared pump, they can be amplified in the 2D VE spectrum. [2] It is possible to mitigate the negative effects of strong solvent responses by using a thinner path length, if the solubility of the sample allows for an increased concentration. The Harrick flow cell used in the lab is rated for use down to a 50 µm spacer, although our group has successfully used

a 25 µm spacer. [3]

Several characteristics of the pump and probe pulses will also influence the overall signal strength and success of an experiment. The first and most important criterion is to optimize the overlap of the pump and probe pulses in the sample, so that the entire volume of sample irradiated by the probe pulse will also have been excited by the pump first. Increasing pump and probe fluence, which depend on pulse energies and focused beam sizes, will increase the signal. Signal scales quadratically with the inverse of the beam waist, by a factor of $1/\omega_0^2$, where ω_0 is the $1/e^2$ beam radius at the focus. [4] If increasing the pump energy is an option, doing so in the low fluence limit will cause the signal to scale linearly, according to Robbens and Cheatum. [4] However, with an infrared pump it is important to ensure that heating signals are sufficiently avoided. References 5–7 provide useful and detailed discussion of the photothermal effects in various types of time-resolved infrared spectroscopy.

In addition to pump and probe fluence, the focusing conditions of the probe will have a large impact on the detected signal. The third-order signal is generated at the sample, and will have a separate divergence and mode from the probe, which also serves as the local oscillator (LO) in the pump-probe geometry. If the focus of the probe pulse is not exactly in the center of the sample cell path, then the differences in divergence will prove to be problematic. Equations (9) and (10) in Ref. 2 reveal that the signal strength scales with $1/(1 + z^2/z_0^2)^2$, where z_0 is the Rayleigh length, and z is the displacement from the beam's focus along the path of beam propagation. In other words, as the distance from the focal spot of the probe increases, the detected signal will decrease, and a shorter Rayleigh length will cause the detected signal to decrease further. Rayleigh length increases as beam quality (referred to as M^2) improves. For reference, a perfectly Gaussian beam has an $M^2 = 1$, and that value increases as a beam mode becomes less Gaussian. Even if the focus is not exactly on the sample, having a better quality beam mode will help mitigate the effects of displacement from the beam focus. Assuming that the divergence of the probe and LO are similar to one another, recollimating the beam following the sample area and focusing into the detector will help to optimize the detected signal. This process is discussed in greater

detail in Section 4.2.1 Therefore, it is important to take extra care when finding the focus of the visible probe beam through the pinhole, as this will be an important factor in determining the overall success of an experiment.

4.2 Setting up for a 2D VE Experiment

4.2.1 Visible Probe Alignment

Given the ever-evolving nature of home-built spectroscopy experiments, this section may change over time. However, the general alignment principles will probably apply to future iterations of the setups in the lab. "Broadband near-UV (BBnUV) line" and "visible line" are used interchangeably and refer to the VE probe pulse, which may also be used as a transient IR pump pulse. More detailed descriptions of the development of the BBnUV line can be found in Refs. 8, 9. Unless something upstream changes, it is generally not necessary to change the alignment of anything in this line before the fused silica plates (FS in Fig. 4.1). Translating the plates vertically should not change the pointing downstream, but moving them in and out of the focus will change the focusing conditions and alignment downstream. Referring to Fig. 4.1, do the following:

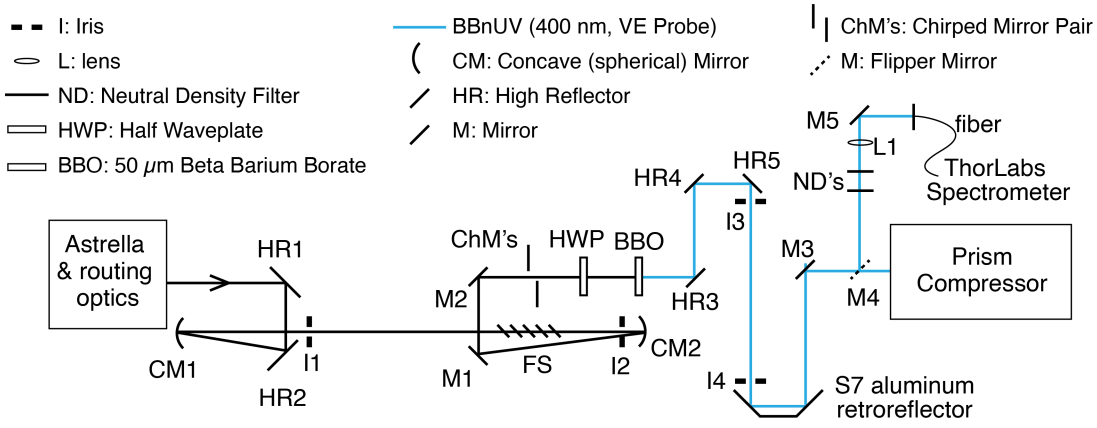

Figure 4.1. Layout of broadband near-UV (BBnUV) line.

1. When aligning with the Astrella output, either decrease the current in the Revolution to the lowest possible value that still produces visible 800 nm light, or decrease the number of round trips through the cavity in the Astrella. If the alignment upstream of the fused silica plates (FS) has changed, use a combination of HR2 and CM1 to guide the 800 nm beam through I1 and I2. Use the 6.3" iris. Do not put a card directly in the focus of the beam (after CM1 and right before FS plates), and remember to remove the iris from position I2 before allowing the beam to reflect off of CM2.

2. Use M1 and M2 to align through I3 and I4, if not using the chirped mirrors. If the chirped mirrors are in use, then insert the second chirped mirror using a translation stage, steer the beam to have the desired number of bounces, and approximately guide the beam to a bolt row after the chirped mirrors.

3. Check the polarization after the BBO. The prisms need to be used in P interactions, so the polarization of the BBnUV should be horizontal in the lab frame. The Astrella output is horizontally polarized, but the BBO flips the polarization to vertical. Instead of using a half waveplate (HWP) and polarizer for the BBnUV light after the BBO, we place an 800 nm HWP in front of the BBO, set the BBO to an angle to frequency double light that is vertically polarized, and use the 800 nm HWP and BBO as a variable attenuator. This avoids the need for an extra optic in the line, which would contribute more dispersion to the pulse. (If the alignment has not changed significantly since the previous experiment, the following steps may be skipped.)

   (a) Remove the half waveplate and place a 400 nm polarizer and a power meter after the I3 position. Set the polarizer to transmit vertically polarized light. It is important to have at least three bounces off of 400 nm high reflectors (HR3, HR4, HR5) to remove most of the transmitted 800 nm light.

   (b) Maximize the power of the BBnUV light by adjusting the angle of the BBO. This will set the BBO to double horizontally polarized 800 nm light to vertically

polarized 400 nm. Then move the BBO angle 90° away, which will set the BBO to double vertically polarized 800 nm light to horizontally polarized 400 nm. The power transmitted through the 400 nm polarizer should drop, but it may not be perfectly minimized depending on the efficiency of the high reflectors.

(c) Lock down the angle of the BBO and replace the 800 nm HWP. Now the angle of the 800 nm HWP may be rotated to attenuate the BBnUV line. Always remember to block all back reflections!

4. Use HR3 to bring the beam onto HR4 if necessary, and HR4 and HR5 to guide the beam through I3 and I4, respectively.

5. Check the spectrum of the BBnUV line with an optical fiber and a portable spectrometer by using the flipper mirror (M4), several ND filters, and a lens (L1). Depending on the quality of the coupling to the fiber, there may be spectral interference which will give the spectrum a jagged structure. Generally this can be corrected by ensuring that the lens and fiber are spaced appropriately for the focal length of the lens and making sure that the beam enters the fiber perfectly straight.

6. Optimize the positions of the fused silica plates while looking at the spectrum. Aim to make the spectrum as broad and even as possible. Try to avoid large dips in the center. After optimization, double check that the beam position through I3 and I4 has not shifted.

7. Adjust the compression of the Astrella to optimize the spectral broadening of the BBnUV. It is helpful to look at the power output of the DFG at the same time, since both rely on the Astrella output's compression. Try to find a happy medium between BBnUV spectrum quality and MIR power and stability.

8. Align the prism compressor.

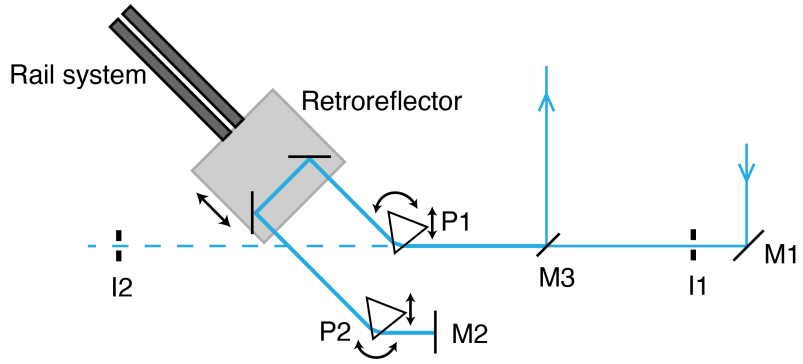

Figure 4.2. Layout of the prism compressor used in the BBnUV line.

Prism Compressor Alignment

Figure 4.2 shows the layout of the prism compressor. Once a prism compressor has been set, it should require very little re-alignment. If the alignment prior to the prism compressor changes, simply record the position of the first prism (P1) and then move P1 on its translation stage out of the beam path. Record the position of the retroreflector stage on the rail system and move it toward the other end of the rail system. Use the S7 retroreflector (Fig. 4.1) or an appropriate near-field mirror to steer the beam through I1 and M1 to guide the beam through the far field iris (I2). Iterate as needed until the beam passes through both iris positions (dashed blue line). Be sure to use the appropriate height of iris for on the breadboard versus off of the breadboard. (**Note:** The beam height before the prism compressor is 6.3 inches from the table. Its height trails down slightly through the compressor and a different iris is used following the compressor.) Reinsert P1 and move the retroreflector back to its initial position. M3 should just pick off the beam underneath the incoming beam to the prism compressor. Be aware of reflections and clipping from all the surfaces of the prisms and make sure they are all blocked. There will be several per prism since the beam passes through each prism twice. The beam will also clip slightly at the tip of each prism. This is normal. If no changes have been made to the amount or type of material that the beam passes through, both prisms may be kept in their initial positions and compression of the beam can

be confirmed with a cross correlation in CaF_2 (see Section 4.2.4) with the MIR following alignment to the sample area. If more alignment of the prism compressor is necessary, or it needs to be moved and reset (ideally avoidable as it is built on a breadboard), then refer to Ref. 10 for more details. Only touch the rotation mounts if a significant amount of realigning is needed (i.e. a prism is bumped from its mounted position). The prisms are held in place by double sided tape and pressure mounts on the top.

Aligning in the Sample Area and to the CCD

After the prism compressor, remove the lenses L1 and L2 and steer the beam with the final prism compressor mirror and M1 (Fig. 4.3) with the "probe post-compression" iris (shorter than the 6.3" iris) at I1 and I2. Then replace the lenses in the collimating telescope (L1 and L2). Use M2 and M3 to steer the beam through I3 and I4 (or I5, depending on which focusing lens is in use at the sample area). Align the beam through I6 using M4, align L3, and find the focus of the BBnUV beam using the pinhole in the sample area. Always do this for the probe before the pump. After the sample area, it is important to recollimate the beam to approximately 5-6 mm diameter, which is the diameter of the aperture for the microscope objective lens used to focus the beam into an optical fiber. Use the same height of iris as prior to the sample area (post-compression probe iris) at I7 and I8, and set the telescope with L4 and L5 to collimate the beam.

At this point, either the optical fiber detection scheme or free space coupling to the spectrometer with a flipper mirror inserted may be chosen. Use M7 and M8 (or the flipper mirror) to guide the beam through I9 and I10 (or I11 and I12). Note that iris positions I9 and I10 are **not** on bolt rows. The rail system for the optical fiber coupling is slightly crooked. These iris positions are set by shining a flashlight through the back of a fiber and out through the objective lens to mark the angle of the lens and rail system, which is not parallel to a bolt row since the rail system is slightly twisted. Make sure the beam is attenuated with ND2 and any other variable attenuators or ND filters necessary before sending it into a fiber and spectrometer. Look at the spectrum of the BBnUV line on the

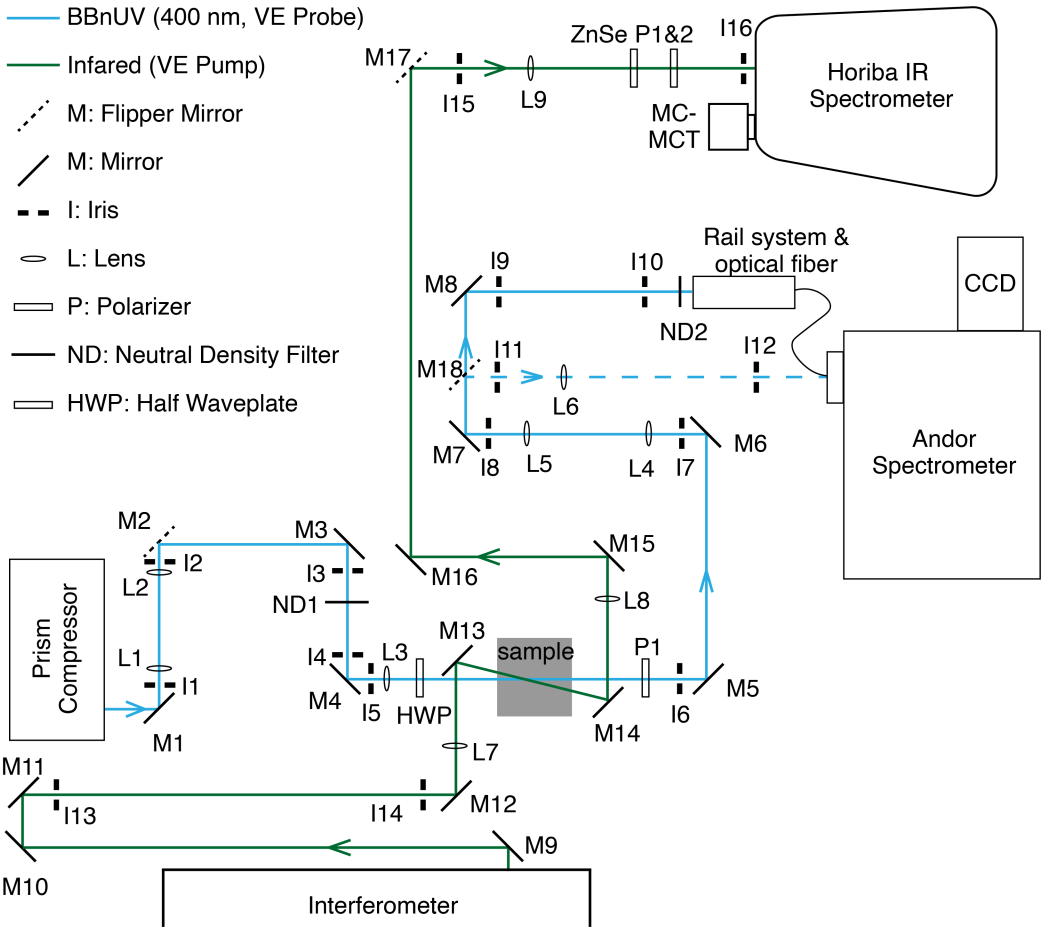

Figure 4.3. Detailed diagram of the sample area, post-prism compressor and post-interferometer. Not to scale, and subject to change.

CCD and optimize the coupling into the fiber by iterating through the pointing with M8 and the z-position of the fiber with respect to the objective lens to maximize the intensity of the spectrum. A poorly coupled spectrum will have fine modulation structure on top of it from scattering/interference. Adjust the ND filter as needed to avoid saturating the detector. This will be fairly easy with a multimode fiber and much more sensitive to beam position, coupling angle, and beam focus with a single mode fiber. (The core of a single mode fiber is generally only a couple microns, compared to 25 µm or several hundred µm in a multimode fiber.) The top and side knobs on the rail system should not be used to optimize coupling

to the fiber. These positions are set by optimizing the circular shape of a flashlight beam coming backwards through the fiber and objective lens (looking at the beam in the very far field). Fiber coupling into the spectrometer may also need to be adjusted by moving the horizontal position and the z-position relative to the slit. Moving the vertical position of the fiber into the spectrometer will change the channel 8 timing (see Section 4.3 for more explanation). Use the Andor Solis software and/or CCD_image_acquire_v_01.vi to view the entire image of the CCD pixels in real time.

Figure 4.4 shows the entire CCD image with two focusing conditions. In (a), the focusing conditions of visible beam are poor, and the image is smeared out. The shot (laser pulse) of interest is in the bottom ≈30 rows, while the other shots are stored in the top rows. See Section 4.3 and Ref. 11 for more detail on how the CCD works. In (b), the focusing conditions are ideal. The shot of interest is in rows ≈10-15 and the separation in the stored shots at the top of the image is more clear. Both of these images were taken with free space coupling. When using a fiber to couple to the CCD and spectrometer, the numerical aperture (NA) of the optical fiber will affect the quality and size of the image. It will likely end up somewhere between (a) and (b) in Fig. 4.4. It is important to optimize the focusing condition because the CCD averages only the bottom 20 rows of pixels. If part of the shot is cropped out, the resulting S/N will be poor. This may also cause problems with the channel 8 delay, which is discussed in Section 4.3. Not that here is a slight tilt to the shot in both images in Fig. 4.4. This has always been present, and is caused by a slight tilt of the grating in the Andor and/or the CCD mounted to the Andor spectrometer. Finally, the images in Fig. 4.4 show a shot in the bottom 20 rows of pixels. This will only be the case when the channel 8 timing is incorrect. Furthermore, be aware that if you look at the CCD image using the Andor software, the vertical position of the shot will be different from the position shown in the LabVIEW vi. This is because the electronic settings in each are slightly different.

To calibrate the CCD, start the Andor Solis software. Choose a grating position that will have at least three emission wavelengths from the small atomic emission lamp on the pixel array. This lamp should cover UV through near-IR wavelengths and has the emission lines

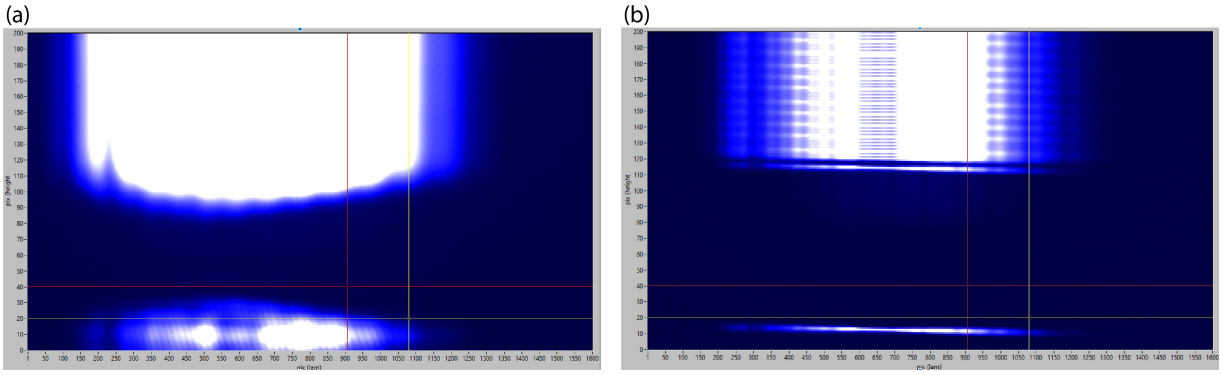

Figure 4.4. Images of the full CCD pixel array with two focusing conditions. a) Poorly focused probe beam into spectrometer and CCD. b) Well-focused probe beam into spectrometer and CCD.

listed on the side of the lamp. Direct the lamp's output into the CCD using a multimode fiber. Save the spectrum and create a calibration axis from it to apply to spectra.

4.2.2 Infrared Pump Alignment

Follow the manual to change the center wavelength output by the TOPAS and (N)DFG. The current configuration uses the DFG in a collinear geometry because the beam asymmetry was significant in the far-field when the non-collinear geometry was used. Additionally, although the manual says that angles of the signal and idler in the non-collinear geometry will compensate for the correct phase matching angle to always output the DFG infrared beam without changing its height between center wavelengths, I noticed some changes. The beam also comes out at an angle which needs to be compensated for with fairly severe angles of M1 and M2 (Fig. 4.5). These angles could be decreased if the height of the HeNe optics were raised. Currently they are set for a 6.3" high beam, which is the height listed by the TOPAS/DFG manuals. Finally, if the non-collinear geometry is ever used, the collimating telescopes will need to be rearranged so that the HeNe and IR beams are overlapped before passing through a telescope. Otherwise, it will be very difficult (impossible) to align the transmissive telescope with only the IR beam.

When changing the center wavelength of the DFG, some realignment may need to be done. Follow the steps below and refer to Fig. 4.5:

1. Find the NIR/MIR safety glasses and wear them while doing alignment greater than fine-tuning. They don't block visible wavelengths very well, so you will still be able to see the HeNe and some 800 nm.

2. With the DFG output blocked, remove the long pass filter (LPF) between M1 and M2. Double check that the angle of the NDFG mirror in the TOPAS software is set to 0° (collinear geometry).

3. Insert a beam block between M3 and M4. Remove L1 and L2. Use the DFG alignment iris (6.3") in positions I1 and I2 with M1 and M2 as the near- and far-field optics.

4. Align the telescope with L1 and L2. Place the power meter (Ophir) after L2.

5. Replace the LPF, adjusting the angle to maximize power through the telescope. The reflection from the filter should hit a block or card on the side of the DFG.

6. Check that no signal or idler is leaked by moving the DFG stage by a large amount (1000 steps should work) in the software. The intensity on a power meter should drop to nearly 0 if both signal and idler are fully blocked by the long pass filter. If there is a significant amount of leaked signal or idler, the filter may need to be replaced or moved from a burn spot.

7. Perform HeNe/IR overlap.

   (a) The iris at I3 should be centered on the HeNe reflected off of the germanium (Ge). If it is not centered, move the iris, NOT the HeNe. If it is off-center by a lot, double check that the HeNe is aligned prior to the Ge.

(b) Flip up M8 and check that the HeNe is centered at I4. If it's a little bit off, adjust the pointing of M8. Sometimes the small flipper mirrors are a bit unstable and need to be corrected. If the alignment is very off, realign on the bolt row after M9 using M8 and M9 as near- and far-field.

(c) Place the Coherent power meter (attached to the lock-in) between I3 and M5, centered on the HeNe. Close down I3 partway, unblock the DFG, and use M3 to maximize power on the Coherent.

(d) Place the Coherent after I4, centered on the HeNe. Use M4 to maximize IR power on the Coherent.

(e) Repeat steps (c) and (d) until the IR and HeNe are well overlapped. Then check a more far-field alignment by placing the Coherent on its "sled" (mount with a 75 mm lens attached in front) after I11 in Fig. 4.6 and do a final adjustment of M4 (Fig. 4.5). It may be helpful to block one arm of the interferometer to avoid potential interference of the arms.

8. Check the spectrum of the IR with a step scan, using XPS_Time_Scan_v6.vi. Setting a step size of 1 fs in the LabVIEW vi (0.299 µm) is generally sufficient for good resolution of the interference fringes. Refer to Fig. 4.7(a-c) for examples of step scans, and remember to use the correct delay stage (S2 for τ_1 scans).

Note: If the HeNe source ever needs to be moved, be careful of the rotation. The polarization of the HeNe beam relative to the table will affect the HeNe tracking in the interferometer and the amount of light reflected from the Ge, which is at Brewster's angle for MIR.

Aligning the Interferometer

Before realigning the interferometer, consider the reasons that you may need to realign. Once you touch an optic inside of the interferometer (BS1 to BS2 in Fig. 4.6), it will be difficult

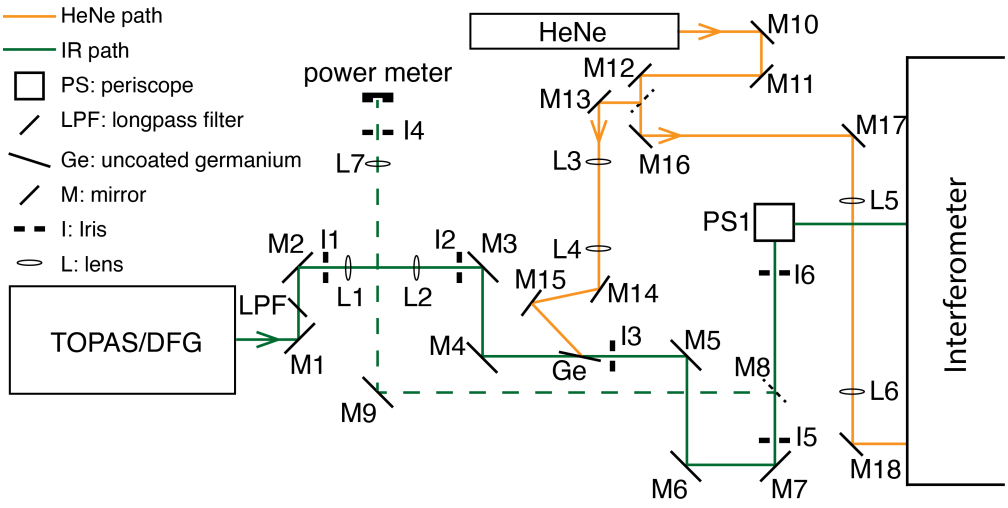

Figure 4.5. Infrared and HeNe overlap layout.

to achieve the initial alignment without going back and re-aligning most optics again. First make sure that the MIR output is blocked, and then use the following checklist to think through whether you need to realign the entire interferometer:

1. Did you bump a specific optic inside of the interferometer? This sometimes happens if you needed to move the chopper or something else in the box. (Be sure to think through the rest of this list before moving an optic.)

2. Check if both arms of the HeNe are overlapped at I12 and all the way to the sample area. If they are still overlapped all the way to the sample area, then the inside of the interferometer is likely still aligned.

    - If both arms are no longer overlapped in the far field (outside the interferometer box and all the way to the sample area) and are diverging from one another, check if one arm is still on the irises you expect the HeNe to be on. If so, you might be able to use the final beam splitter or mirror to correct it.

3. Check if the alignment of the HeNe entering the interferometer has changed using the

two iris positions on the bolt row before periscope 1 (I1 and I2).

- If the alignment is not correct going into the periscope, return the HeNe beam to I1 with M1 (near field) and to I2 with M2 (far field). Iterate as much as necessary and then check the alignment on iris positions I10 and I12. Be sure to use the correct irises for inside the interferometer box (5.5") versus outside (6.3").

4. Check if the pointing of the HeNe has changed after the interferometer. If the HeNe is still on the irises prior to the interferometer and both arms are still overlapped very far downfield, then this could be the problem.

   - Check the alignment of both the bright and dark outputs after BS2 to the sample area and MCT, respectively. If only one arm is misaligned, then the problem is likely only in one arm after the interferometer.

5. Check the final alignment by taking a step scan on the coherent power meter through the lock-in detector. Be sure to double check the overlap of the HeNe and MIR if necessary before taking the scan. If the scan is symmetric and has good interference at $\tau_1 = 0$ fs, then the interferometer is well aligned.

If you are unable to correct the alignment with any of the above suggestions and/or the pointing of a single optic, it may be necessary to realign from the start of the interferometer. This can typically be done without removing any optics. However, if the alignment is extremely off it is also a good idea to ensure the beam enters the interferometer on a bolt row.

1. Use M1 and M2 as near-field and far-field to steer the beam onto I1 and I2.

2. Carefully remove the M3 mirror from its mount to send the HeNe straight through onto I4. Alternatively, remove the entire mount, but leave the post screwed into the

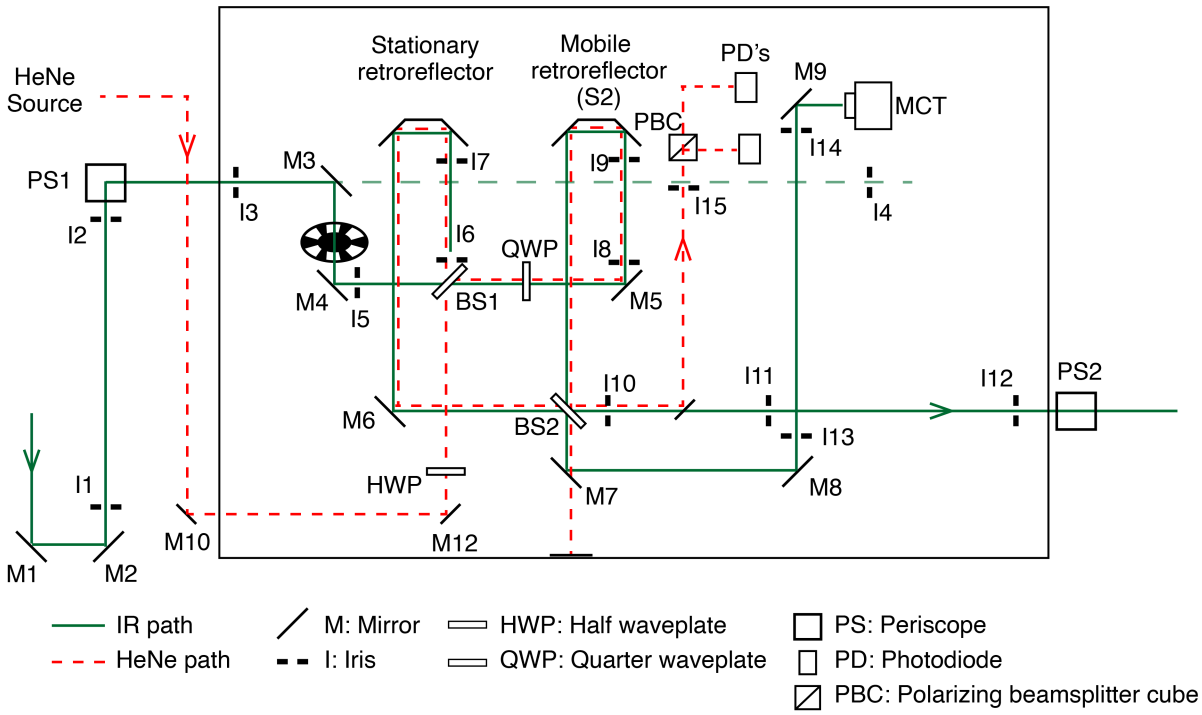

Figure 4.6. Layout of the MIR interferometer and HeNe tracking arm with labels.

breadboard. Use the bottom mirror and the top mirror of the periscope to steer the beam onto I3 and I4. Replace M3.

3. Use I5 to correct M3 steering.

4. Check beam positions on I6 and I7. If the position on I6 is fine, use BS1 to steer the beam through I7. If the position on I6 is very far off, use M4 to correct it while keeping an eye on the position of the beam through I8. The beam does not need to pass perfectly through I6 and I7, especially since this is the stationary arm. As long as it's not clipping anywhere the alignment should be fine for the most part.

5. Use M4 and M5 to steer the beam roughly through I8 and I9. The retroreflector for the mobile arm (on motorized delay stage S2) is not perfectly normal to the bolt row, so the beam will not end up being perfectly aligned through I8 and I9.

(a) Block the stationary arm —– the interference from the beams makes it difficult to see the alignment. In the XPS user interface, disable S2. Place a card with a grid or some markings on it as far-field as possible, ideally right before the lens in the sample area. This card will be used to monitor whether the HeNe pointing changes as the stage moves.

(b) Use only M5 as the far-field optic. Push S2 all the way forward and look at the position of the HeNe on the card you placed near the sample area. This is your near-field "iris." Push S2 back all the way and use the markings on the card to see if the beam moved. This is your far-field "iris." If the beam stays in the same spot on the card for both ends of the stage, it is well aligned into the retroreflector. If the beam moves in the far-field, adjust the pointing of M5 to bring it back to its near-field position. Continue to iterate between stage near-field and far-field positions until the beam no longer changes between stage positions.

6. Use the vertical and horizontal micrometers on the S2 retroreflector to steer the mobile arm through I10. Use BS2 to steer the mobile arm through I12. Iterate as needed to align the beam to the bolt row.

7. Block the mobile arm and unblock the stationary arm. Use the vertical and horizontal micrometers on the stationary retroreflector to steer the stationary arm through I10. Use M6 to steer the mobile arm through I12. Iterate as needed to align the beam through both irises on the bolt row.

   Note: If each arm of the interferometer is aligned through I10 and I12, ideally not much more alignment will be required. However, the interferometer can be finicky, especially with shorter pulses, and the last couple steps (8-10) can take anywhere from ten minutes to several hours.

8. These last steps (8-9) have the goal of bringing the stationary arm to be exactly overlapped with the mobile arm. (It's fine to do it the other way around, but I usually find

it easier to adjust the stationary arm pointing rather than the mobile arm pointing.) Place a beam block with a white card on it in the beam path shortly after I10. This is your near-field "iris." It may be helpful to use a card with markings or a grid. Unblock both arms, and while looking at the beam on the card do either of two things (or both):

- Block and unblock either the mobile or stationary arm and correct the pointing of the stationary arm relative to the mobile arm using the micrometers on the stationary retroreflector.
- Take one card in each hand and alternate blocking each arm to see if the beam on the cards shifts. Correct the pointing of the stationary arm as above.

9. Place a card or beam block with a card on it just before the sample area to act as the far-field "iris." Repeat the above steps, but this time using M6 to adjust the pointing of the stationary arm relative to the mobile arm.

10. Repeat steps 8 and 9 until you are satisfied with the overlap of both arms in the near- and far-field. When the beams are aligned, there should be a grid-like interference pattern over the entire HeNe beam mode. If the lines slant one way or the other, the arms may not be perfectly aligned. The final test to check alignment is to run a step scan. See Fig. 4.7 (a,b) for an example of the interferogram from a well-aligned interferometer. Remember to reintialize S2 if you haven't already and keep in mind that $\tau_1 = 0$ may have shifted.

    Note: If the step scan looks like the interferogram in Fig. 4.7(c), in which the point of maximum interference is destructive rather than constructive for the bright output, then return to steps 8-10 until it looks like Fig. 4.7(a) or (b). This is not terribly important for day-to-day tests but is very, very important for running a 2D VE experiment since the fast scanning (described in Chapter 2 and Ref. 1) assigns $\tau_1 = 0$ based on the point of maximum destructive interference in the dark output of the interferometer.

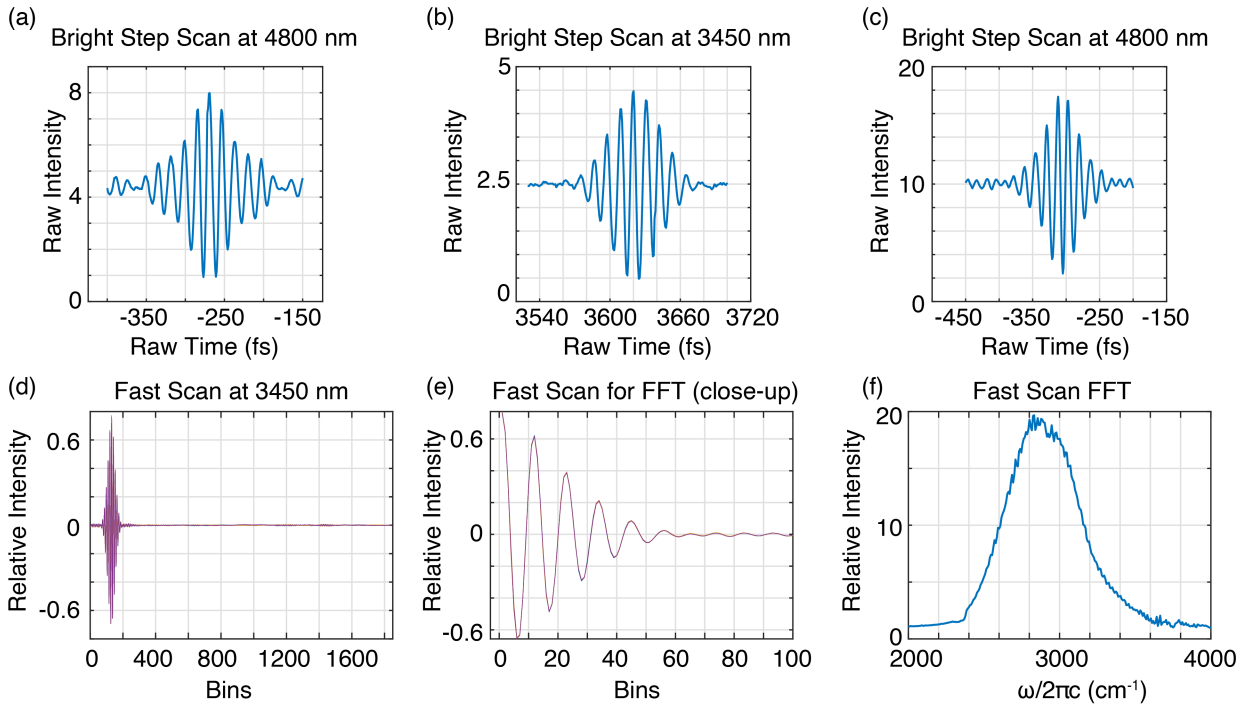

Figure 4.7. Step and fast scan examples. The S2 delay stage is stepped by discrete distances in a step scan. It is continually scanned at a rate of 0.06 mm/s or a fast scan. a) Step scan of well-aligned interferometer bright output with DFG centered at 4800 nm. b) Step scan of well-aligned interferometer bright output with DFG centered at 3450 nm. c) Step scan of almost-aligned interferometer bright output with DFG output centered at 4800 nm. d)Full fast scan time domain with DFG centered at 3450 nm. e) Cropped (at $\tau_1 = 0$ fs) fast scan in the time domain, zoomed in. d) Averaged Fourier transform of the fast scan time domain (from four scans in (d) and (e)).

The interferogram from a step scan should be symmetric. The point of maximum interference should be close to double the intensity of the average intensity, and the points of maximum deconstructive intereference should be as close to 0 as possible. Remember to set the speed of the S2 stage back to 300 mm/s. If a step scan on the coherent detector through the lock-in looks good, move on to a fast scan. See included figures for examples of fast and step scans from a well-aligned interferometer. After realigning the interferometer, it is likely that the HeNe tracking arm will also need some adjusting. At this point, if the interferometer is well-aligned, it is extremely important to not touch any optics that route

the MIR. It should be possible to only use M10 and M12 to steer the HeNe tracking beam to be vertically offset from the MIR/HeNe beam throughout the entire interferometer, as long as the beamsplitters have excellent surface quality and parallelism.

Check the alignment of the HeNe tracking beam using an oscilloscope. Before doing this, make sure the half and quarter wave plates are in the line and the HeNe is hitting both photodiodes. Set the S2 stage to cycle at 0.06 mm/s over a small, arbitrary range (for example, 0.3 - 0.6). Connect the PD 1 and PD 2 BNC cables (normally in the DAQ) to the oscilloscope in channels 1 and 2. Look only at channel 2. Set the scale for each channel to the same value; 20 mV is usually fine, and adjust the timescale until you see a rounded triangle on the oscilloscope. It will blip each time the stage changes directions. The goal is to make the rounded triangle as round and large as possible. Optimize the HeNe tracking using the pickoff mirror before the polarizing beamsplitter cube, the pointing of the PBS cube, and the pointing of the mirror after the PBS cube to optimize tracking. The light entering the beamsplitter cube should be roughly on a bolt row. Iterate as needed.

4.2.3 Aligning to the IR Spectrometer (Horiba)

Refer to Fig. 4.3 for the steps listed in this section. The IR spectrometer should be used for any experiment that requires both IR detection and spectral dispersion of the probe. These experiments could be infrared pump - infrared probe, transient IR, or 2D IR.

1. Slowly fill the multichannel MCT (MC-MCT) with liquid nitrogen. As it cools, do the alignment below.

2. Depending on whether the z-position changed, the position and alignment of L8 may need to be adjusted. Try to use only M14 to steer the HeNe beam to be as straight and level as possible between M14 and M15.

3. Adjust the position of L8 so that the HeNe focuses just before M17. (The different indices of refraction for mid-IR and visible light in the CaF_2 lens cause the overlapped

beams to have different effective focal lengths.)

4. Remove L9 and the ZnSe polarizers. Use M16 and M17 to guide the beam through iris positions I15 and I16. Use the IR spectrometer iris.

5. Replace and align L9 with the HeNe. Place one or both polarizers and remember to block the back reflection from the HeNe.

6. Initialize the spectrometer with the Horiba software, turn on the FPAS (femtosecond pulse acquisition spectrometer), and open the FPAS2acqmainMX_UltrafastTIR.vi to view IR spectra. The MC-MCT has two rows of 32 pixels each (1-64). Check that the range of pixels displayed in the vi matches whichever of the top or bottom row the MCT is aligned to. If you're not sure, change the range to 1-64.

7. Set the spectrometer to the 0^{th} order reflection and look for intensity on a pixel.

8. Adjust the pointing of M17 to bring the reflection to the center of a pixel row and minimize the width of the 0^{th} order reflection by moving the L9 translation stage. Iterate as needed and adjust the polarizer(s) to avoid saturating the detector.

9. Sometimes there is a weird software glitch that causes the 0^{th} order reflection to appear insensitive to the L9 position. If that seems to be the case, adjust one of the polarizers to see if the detector can be saturated. If it doesn't saturate (5 V), then power cycle the FPAS. Sometimes the vi also needs to be stopped and started or closed and reopened.

10. Calibrate the IR spectrometer using a polystyrene film or other sample with well-defined absorption features. Water lines can also work well, depending on the wavelength region.

4.2.4 Finding Timings and Compression Settings

To set the compression of the visible line, it is convenient to use a cross-correlation of the IR with the visible line in CaF_2 at the sample area. Start by finding spatial overlap of the BBnUV and IR with a pinhole. For a VE experiment, bring the pinhole to the focus of the BBnUV line first. The BBnUV should already be aligned on a bolt row through the sample area. Record the power before and after the pinhole at the focus to check the spot size using spot_size_calculator.vi or Read_lockin.vi (Appendix E), and record the sample stage position. This will be the "pinhole z-position." In a VE experiment, aim for a spot size of ≈130–160 µm. If the spot size at the focus is far from this range, change the probe focusing lens (L3 in Fig. 4.3) for a lens of a different focal length, and/or adjust the collimation with L1 and L2. The beam may be set to slightly diverging or slightly converging after the telescope in order to change the focused spot size at the sample area. Remember that if you adjust the collimation, the focus at the sample area will move. Once the focus of the BBnUV probe is set at the sample area, block the BBnUV line and bring the focus of the IR line to the pinhole at the pinhole z-position. Use L7 and M13 to adjust the focusing condition and pointing through the fiber, respectively, to maximize the power through the pinhole. Aim for a spot size of ≈150–200 µm in a VE experiment. If the spot size is far from this range, refer to Fig. 4.5 to adjust the IR collimating telescope with L1 and L2, and check HeNe/IR overlap again.

Once the pump and probe beams are spatially overlapped, find the temporal overlap (τ_2 timing). Replace the pinhole with a thin piece of silicon. Increase the power of the visible line to ≈0.4 µJ and set the τ_2 delay stage so that the visible arrives earlier than the IR. If you don't know where exactly, set the τ_2 delay stage as far forward as possible. Block the mobile arm in the interferometer, and detect the stationary arm on the Coherent power meter through the piece of silicon. Turn on the visible chopper and trigger the lock-in off of the visible chopper (it should now read 0 mV). Looking at Read_lockin.vi, translate the sample stage until you see a difference signal (≈0.1 mV). The strength of the difference signal

will depend on the quality of the vis/IR overlap, how far the timing is from $\tau_2 = 0$ fs, the spot sizes, and the power of both beams. Step the τ_2 stage 1–2 mm at a time until the difference signal goes away, then run a step scan using XPS_Time_Scan_v6.vi over a 1–2 ps range to find exactly where $\tau_2 = 0$ fs. To fine-tune the overlap, you can return the τ_2 stage to just before the difference signal starts to drop, and adjust the pointing of the IR beam with M13 (Fig. 4.3) to maximize the difference signal. Record the mid-point of the scan.

Lastly, check the compression of the BBnUV line with a CaF_2 trace, which is a cross-correlation of the IR and the visible line. [12] Although CaF_2 is transparent to visible wavelengths, the visible pulse mixed with IR in CaF_2 produces a non-resonant response that corresponds to pulse lengths. To take a CaF_2 trace, decrease the power of the BBnUV to ≈15–30 nJ using the half waveplate before the BBO (Fig. 4.1) and/or ND1 (Fig. 4.3). Check the alignment to the CCD, if necessary. It is optional to unblock the mobile arm of the interferometer at this point and move S2 to $\tau_1 = 0$ fs. The delay stages have a small amount of hysteresis; combined with some laser drift, it means that the position of $\tau_1 = 0$ fs will shift, so move the stage to the recorded position and then step S2 in very small increments (0.00005 mm) to find the point of maximum interference on the Coherent power meter. Then, replace the Si in the sample area with a thin CaF_2 window (≤1 mm, ideally even thinner than 1 mm.) Move the τ_2 stage to $\tau_2 = 0$ fs and change to chopping the IR instead of the visible line. Look at CCDacquire_vTrial8.vi on the "single chopping" setting and scan the z-position of the sample area stage to find the non-resonant response. The correct position may be several mm away from the pinhole z-position and/or the Si z-position. Use CCDTime Scan_v5_rbw.vi to collect the scan, and plot it with ve_1d_t2_scan_workup_rbw.m. The shape of the non-resonant response from CaF_2 will report on the compression of the visible pulse, as long as the IR pulse has been characterized.

Figure 4.8 shows three examples of these traces. The first trace in (a) has a lot of spectral interference along the ω_3 axis, which is a result of the channel 8 delay being incorrect (see Section 4.3). The second example in (b) shows the same prism compressor settings as in (a), but with the correct channel 8 delay. The non-resonant response is tilted, indicating that the

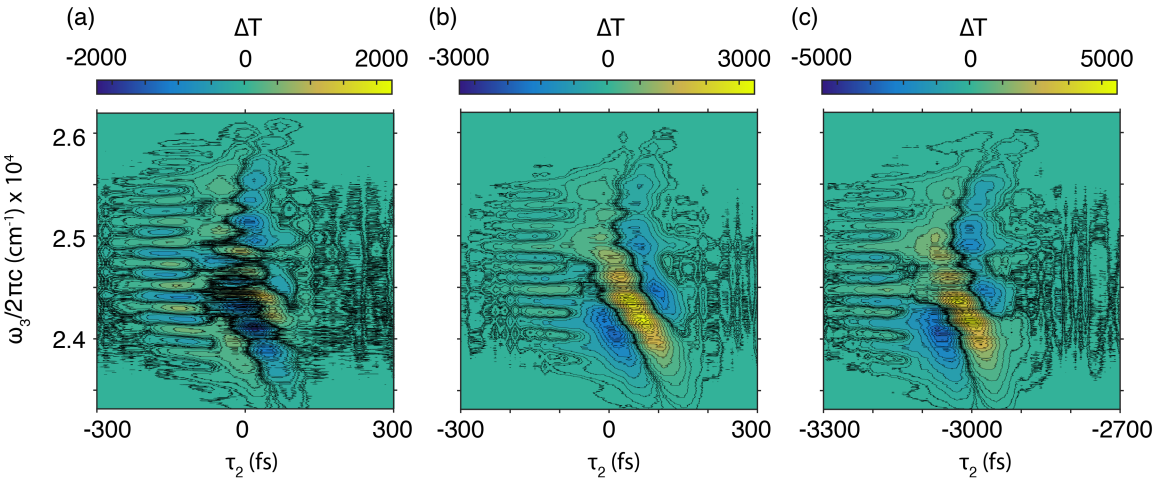

Figure 4.8. Examples of CaF_2 traces. a) Uncompressed BBnUV crossed with MIR in CaF_2 at the incorrect channel 8 timing/delay. b) Uncompressed BBnUV crossed with MIR in CaF_2 at the correct channel 8 timing. c) Compressed (as much as possible) BBnUV crossed with MIR in CaF_2 at the correct channel 8 timing. τ_2 times are set with the same $\tau_2 = 0$ stage position for all three scans shown. Prism compressor was moved so that the beam transmitted through less material in (c) than in (b).

BBnUV pulse has some second order dispersion (assuming the MIR pulse is compressed). The third example in (c) shows a BBnUV pulse with minimized second order dispersion after moving the prisms out of the beam path (decreasing amount of material); the non-resonant response is more upright, although the curve indicates residual third-order dispersion in the pulse. This is very hard to correct for, as the prism compressor imparts both second and third order dispersion to the pulse. Chirped mirrors and grating (or "grism") compressors can do a better job of compressing a pulse, but are usually more costly and difficult to implement. To adjust the compression of the BBnUV, move the prisms in the compressor in or out of the beam path. Doing so should not significantly change the overlap at the sample area, but it will change the τ_2 timing. **Inserting one fused silica prism into the beam path by 1 mm on the translation stage will delay the BBnUV pulse by an additional ≈5300 fs relative to the MIR.** In Fig. 4.8, each prism was moved out of the beam path by ≈ 0.3 mm after (b) to achieve the compression in (c). Once the BBnUV compression is

optimized, realign from the prism compressor to the sample area and CCD if necessary.

4.2.5 Aligning in the Sample Area: An Experimental Checklist

Use this checklist with brief explanations to keep track of the steps when setting up for an experiment. More details and explanation are provided in the preceeding and following sections.

1. **Place polarizers, ND filters, etc.** Add any transmissive optics before the sample area that you will need to do an experiment, such as polarizing optics, neutral density filters, compensation plates, windows, etc. since they will slightly change the pointing and focusing conditions of any beam that passes through them. Remember not to touch the angle of these optics during the experiment, or your overlap conditions will also change.

2. **Check stage alignment.** Before spending the time to find spatial and temporal overlap, do one last check to be sure that the alignment of the probe into the delay stage is very straight and level. If not, take the time to go back and fix it, otherwise the overlap at the sample area will change each time the τ_2 delay changes.

3. **Pinhole overlap and adjust focal points.** Find overlap between the pump and probe pulses using a pinhole. A pinhole with a diameter of 100 or 150 µm generally works well, as long as you keep track of what the inner diameter is when calculating laser spot size. Aim to find the probe focus as exactly as possible. Recall that birefringent (non-resonant, i.e. solvent) response becomes dominant away from the probe's focus.

4. **Silicon trace.** Find τ_2 delay with a thin piece of silicon. This can be sandwiched between two windows or free. Be sure to increase the probe (BBnUV or other visible pulse) power to pump the silicon. Around 1 mV on the coherent, or ≈0.4 µJ is generally sufficient, depending on the focus size.

5. **Set channel (delay) 8 timing.** The only time you will need to change the channel 8 timing is when the alignment of the second end of the fiber into the CCD has changed, or if the table and BNC cable layout have changed a significant amount. The channel 8 timing is on the order of 10's to 100's of µs, and one foot of path length traveled by pump or probe on the table is 1 ns, so typical realignment won't change the timing.

6. **Set CCD offset.** If the channel 8 timing changed, chances are the CCD offset has changed. If not, and the table layout is largely the same as the last experiment then there is no need to change the CCD offset.

7. **CaF_2 scan to set prism compressor.** Switch the pulse ordering and use a CaF_2 window to check the prism compressor settings. Decrease the BBnUV/visible probe power to ≈10–30 nJ to avoid self phase modulation in the CaF_2 window.

8. **Realign after prism compressor.** If you needed to adjust the prism compressor settings at all, you may need to realign after the prism compressor (or whatever is used to compress the probe pulse) to maintain optimal overlap of the pump and probe focal points at the sample area.

9. **Check relative polarizations of the pump and probe at the sample area.** This step can be done any time after the alignment into the sample area is set and before an experiment starts. Place the polarizer in the sample area so that it sees the same polarization as the sample cell will. Remember that the polarization of the MIR may not be exactly vertical, so set the polarization of the BBnUV/visible line relative to the MIR. Some polarizers are marked along the axis of transmitted light, and some are marked along the axis of the wires blocking light. The visible and IR polarizers are marked opposite from one another, but double check which is which before using.

10. **Silicon trace inside sample cell.** Because the z-position will shift for each item placed in the sample area, it is helpful to place a piece of silicon in the sample cell to

get an idea of where the sample cell z-position will be.

11. **Assemble sample cell and check for leaks.** Check the sample cell for leaks by flowing neat solvent. If the solvent for your experiment is expensive or particularly hazardous, choose a safer, miscible solvent to flow while checking for leaks in the wet lab.

12. **Transient IR.** Increase the BBnUV/visible pulse power to be used as a pump. Block the mobile arm of the interferometer. Use a tIR experiment to find the z-position of the sample cell. Collect tIR data if desired. If the VE signal is sufficiently strong to view a 1D VE signal in real time and you don't need to collect any tIR data, you can skip this step.

13. **1D VE.** Decrease the BBnUV/visible pulse power to be used as a probe. Leave one arm of the interferometer blocked or overlap the two MIR pulses in time. Take a short 1D scan to double check prism compressor settings and $\tau_2 = 0$. While looking at the chopped signal in real time at $\tau_2 \approx 300$–500 fs, iterate between adusting the z-position, the pointing of the MIR, and the coupling into the fiber to maximize 1D VE signal. Check that the 1D signal disappears when the pump is blocked and when the delay stage is set to negative τ_2 VE delays (visible pulse arrives before IR).

14. **2D VE z-scans (optional).** If the 1D VE signal is too weak to optimize z-position and overlap, it may be necessary to take 2D VE z-scans to find the z-position. This is particularly true for systems like $K_3[Fe^{III}(CN)_6]$ and SNP, which have weaker vibronic coupling than a highly electronically delocalized compound like HBQ, with its conjugated backbone. Take 3-7 2D VE scans at various z-positions in the range where you saw maximum tIR signal, every 5 µm or so. Choose the z-position with the best 2D VE signal strength.

15. **Pump power linearity check.** Use a polarizer, ND filters, and combinations of a

single or double interferometer arm to vary the IR pump power and check that the signal scales linearly with pump power. Record signals and pulse energies with error bars. The same may be done for probe power, but is less important. Be careful not to change the polarization of any pulses when attenuating the beam intensity.

16. **Fine step IRF scan (optional).** Take a finely stepped ($\leq$10 fs) 1D VE scan of neat solvent or ideally a thin piece of CaF_2 for the cross-correlation of pump and probe. See Refs. 13, 14, Chapter 2, and Appendix A for details regarding scan division by the IRF.

17. **Collect 1D and/or 2D VE scans.** Remember to record pump and probe powers at the start and end of each day. The 2D VE collection vi and processing code will save transmitted probe spectra, but it's a good idea to collect a simple probe spectra too.

4.3 Electronic Settings

For visible light detection, we use a CCD with silcon pixels. The CCD is comprised of 200 rows of 1600 pixels each. The semiconducting material of the pixels is excited by the incoming photons and converts the signal to a charge, which is transmitted to the computer. There are various settings that may be used, depending on the type of experiment you would like to run. For most experiments, two types of settings should be considered: the region of interest in the pixel array, and the length of time spent integrating the signal detected by the pixels. For example, in a microscopy experiment it may be desirable to look at the entire image of the 200 x 1600 pixel array, and integrate for several milliseconds or seconds. Conversely, for a spectroscopy experiment it may be beneficial to choose a smaller region of interest and shorten the integration time. If, for example, a pulsed laser system operates on a 1 kHz clock, it will be important to collect data (one shot) each 1 ms rather than averaging many shots over many milliseconds or seconds. The charge on the pixels from one data collection interval (or shot) must be cleared before the next shot can be detected. Charge on a CCD is read one pixel at a time, and the CCD must shift and clear charge both horizontally and

vertically. Shifting charges takes a finite amount of time, and must be completed between successive laser shots in order to not waste any shots. It takes approximately 9.7 µs to shift vertically, and less time to shift charge horizontally. Pages 28-29 of the Andor Newton manual (Ref. 11) explain this process in more detail. The signal integration time may be set in the Andor software, or in the collection vi for most VE experiments.

4.3.1 Channel 8 Delay

The timing of the when the charge clears from the pixel array is referred to as the "channel 8 timing/delay" or "delay 8." The channel 8 delay is the difference in time between the main trigger (or "clock") in the laser system and when the CCD starts to collect data. This timing depends on several things: 1) The vertical positioning of the beam on the CCD and 2) The length of beam paths on the table and the BNC cables. An incorrect channel 8 timing means that the CCD clears charge in the middle of a laser shot. If the channel 8 timing is incorrect, shots that are supposed to be "pump off" (IR pump is blocked by the chopper) will have some pixels that detect intensity from the wrong shot (a "pump on" shot). When the processing code runs to subtract pump on – pump off, the sign will be incorrect for part of the signal and you may end up with a derivative-shaped signal in a 1D VE spectrum, or extra oscillations and sign changes in a 2D VE spectrum. In order to determine if the CCD clears charge at the correct time, looking at a 250 Hz signal instead of a 1 kHz signal is useful. If we know that the CCD should only "see" light every 4 ms, then the other 3 ms should be empty. Figure 4.9 demonstrates the difference between three channel 8 timings. The intensity on three pixels spanning the entire spectrum is plotted as a function of laser shot. In this example, Ch. 8 = 500 µs is the correct timing. Every pixel has intensity on it exactly every fourth shot. During the other three shots, none of the pixels show any intensity. Conversely, at Ch. 8 = 0 µs it is clear that pixel 1000 detects some intensity on a shot before pixels 250 and 400 do. At Ch. 8 = 100 µs, pixel 250 detects some intensity on a shot after pixels 400 and 1000 detect the light.

If no changes to the table have occurred other than routine realignment, and if the

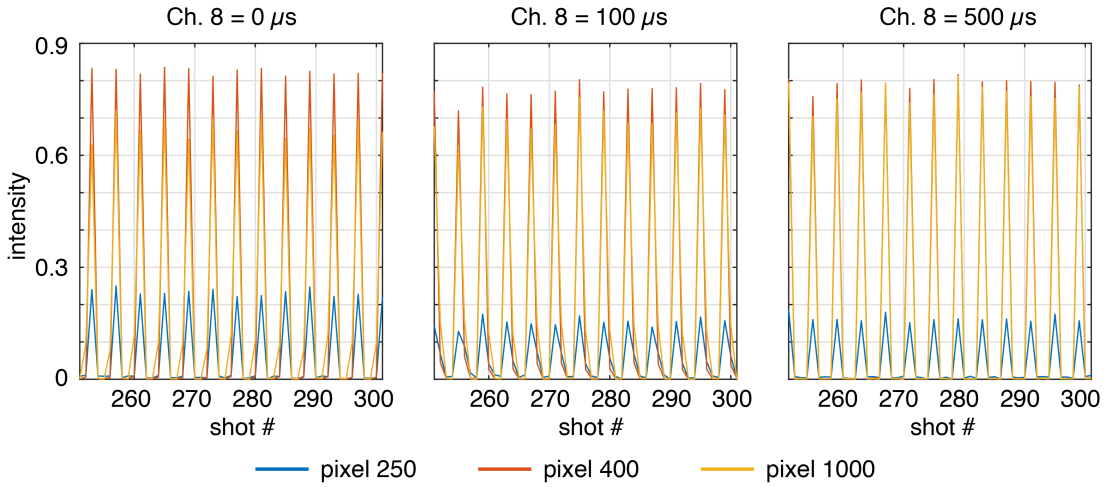

Figure 4.9. Three settings for the channel 8 timing (delay 8) at three pixels (250, 400, and 1000). Ch. 8 = 500 μs (right) is the correct timing in this scenario.

coupling of the fiber into the Andor has not changed, then the channel 8 timing should not change from the previous experiment. (The coupling of the beam into the fiber can change and will not have an effect on the channel 8 timing.) To check the channel 8 timing, do the following:

1. Align the visible probe through the sample area and couple into the fiber as normal.

2. Carefully move the IR chopper to the visible line. Change the height if necessary, and phase it to chop at 250 Hz instead of 500 Hz. To do this, simply change the subharmonic option from 2 to 4. Use a photodiode or the coherent power meter connected to the oscilloscope to find the phase where one shot is fully transmitted, the two shots on either side are half-blocked, and the last shot is fully blocked. Then move the phase 45° away. Turn on the visible chopper and check that only every fourth shot passes through the choppers.

3. Adjust ND2 (Fig. 4.3) as needed and check the spectrum of the visible probe light on the CCD. Since every fourth shot makes it through, the total counts should not exceed

15,000.

4. Using the 2D VE collection vi (Appendix E), collect one scan with ≈1,000 shots at a range of channel 8 timings. Generally, it works to check every 100 µs (from 0 µs to 800 µs) and go back to check every 50 µs if the correct timing is not obvious after that. Be sure to select the "save raw data" option in the vi.

5. Use the ch8_timing.m script to plot and compare all timings tested. There is usually a range of times that look correct, so pick one roughly in the middle.

6. Return the IR chopper to its place in the interferometer, return the subharmonic to 2, and rephase it correctly.

7. Most importantly, remember to change the channel 8 timing to the delay you determined to be correct.

4.3.2 CCD Offset

During a 2D VE experiment, there is some lag between when the CCD says to start collecting data and when the DAQ also starts collecting data. This is a potential problem because the signal in our experiment is detected by the CCD and sent directly to the computer, but the τ_1 tracking is sent from the SC-MCT to the DAQ. Shots collected from the CCD and the DAQ must match up with one another. If not, the τ_1 assignments will be incorrect and a phase error will be introduced to the Fourier transformed 2D VE data. This can show up as extra oscillations in ω_1 and/or a sign change. To avoid this, the first shot(s) from the CCD are ignored so that DAQ and CCD shots match one another. To find the correct CCD offset, we need to look at the same thing detected two different ways. We can chop the visible probe, split it up, and detect in both through the CCD and the DAQ to compare the two. With the correct offset, the CCD and the DAQ should report intensity on the same shots. Figure 4.10 shows three offsets. Normalized and de-trended intensities (centered around 0)

are plotted as a function of shot number for the photodiode (blue, collected through the DAQ) and the CCD (orange, collected by the computer). Offset = 1 (center) is the correct offset. The same shots on the photodiode and CCD either both have no intensity or full intensity. In other words, the intensities must match as closely as possible for the same shot numbers between the photodiode and CCD. Offset = 0 is clearly incorrect; the photodiode and CCD are reporting intensity on different shots. Offset = 2 is also incorrect, but looks less obvious.

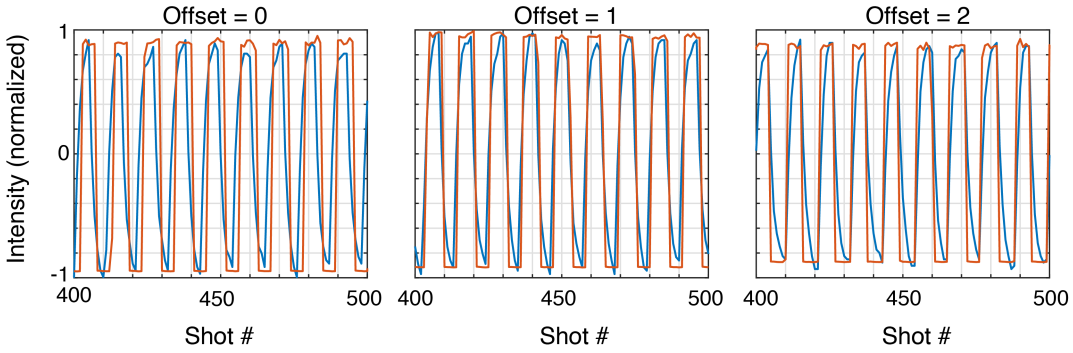

Figure 4.10. Three settings for the CCD offset, collected with the chopper internally triggered and set to 181 Hz (subharmonic = 2). Photodiode signal collected through the MCT slot in the DAQ plotted in blue, CCD signal plotted in orange. Offset = 0 (left) and offset = 2 (right) are incorrect. Offset = 1 is correct in this scenario. -1 on the y-axis means no intensity is on the pixel.

1. Always set the channel 8 timing before the CCD offset. If the channel 8 timing is wrong, the CCD offset might also be wrong. Do this if it hasn't already been checked.

2. Increase the power of the visible probe to tIR levels and use a higher optical density ND filter (ND1 in Fig. 4.3). Train the back reflection of the ND filter onto a white card. Keep the fiber input to the CCD blocked for now.

3. Place a photodiode (for the appropriate wavelength detection range, likely a silicon photodiode) to the right of M3 in Fig. 4.3. Keep the switch in the "off" position (no

need for a bias voltage) and connect it to an oscilloscope with a BNC cable.

4. Adjust the angle of the photodiode and the card with the ND filter's reflection on it, and the distance between the two until the photodiode picks up the diffuse reflection from the white card. Photodiodes are extremely sensitive, so it is important not to put a beam directly onto its pixel to avoid burning it. It may be necessary to increase the scale on the oscilloscope.

5. Connect the photodiode to the MCT input on the DAQ.

6. Trigger the visible chopper internally and change the frequency to some prime number. A lower frequency of the chopper, like 181 Hz, will give a more consistent result.

7. Adjust ND2 (Fig. 4.3) as needed and check the spectrum of the visible probe light on the CCD. Since every other shot makes it through, the total counts should not exceed 30,000.

8. Use the 2D VE collection vi (Appendix E) to collect one scan with ≈1,000 shots at a range of CCD offsets. Checking from 0–10 should be more than sufficient. The offset is almost always between 0–4, but it's fine to be safe and check extra offsets. Be sure to select the "save raw data" option in the vi.

9. Use the ch8_timing.m script to plot and compare all offsets tested. Some offsets may look very similar to one another. If that is the case, it is usually the smaller offset but you can pick another internally triggered chopper frequency to test again and compare results.

10. Return the CCD offset in the vi to the value determined to be correct, then reconnect the single channel MCT to the DAQ. Trigger the visible chopper externally and double check that it is still phased correctly.

4.3.3 Data Acquisition (DAQ) Settings

The DAQ board acquires multiple signals during an experiment. It reads the single channel MCT voltage, a "fire" signal from the CCD, two photodiode voltages, the chopper voltages, and a trigger (TTL signal). At some point, you may need to check that the MCT is properly triggered. The DAQ reads an instantaneous voltage from the MCT, which at this time is triggered off of the **falling** edge. Whether it is the falling vs. rising edge of the trigger signal can be found in the LabVIEW vi's. If the signal from the MCT read through the DAQ seems low and noisy compared to what is shown from the MCT on the lock-in, the triggering is probably off. This can be viewed on an oscilloscope, and the timing of the trigger can be adjusted by changing whichever delay is used on the synchronization and delay generator (SDG). Currently, that is delay 6.

4.4 Solvent Effects in 2D VE Spectroscopy

4.4.1 Introduction

Solvent effects in 2D VE spectroscopy are important to consider; as a third order coherent spectroscopy, 2D VE can amplify overtone and combination modes. [2] Sodium nitroprusside (SNP, $Na_2[Fe^{II}(CN)_5NO]\cdot 2H_2O$) is an iron-centered complex with two different types of IR-active ligands, as shown in Fig. 4.11(a). The ground state ν_{NO} and ν_{CN} vibrations have been studied with 2D IR spectroscopy in a series of solvents; although no cross peaks were found between the two vibrations (indicating no ground state coupling between the two vibrations), the vibrational dephasing time of the nitrosyl stretch was found to depend strongly on solvent polarity. [15] SNP is solvatochromic, but the frequency of the ground state nitrosyl stretch has a stronger dependence on the solvent than the cyano stretching frequency. π-back-bonding between the CN^- ligands and the Fe center increases with solvent polarity and increases the frequency of ν_{NO}. The excited state vibrational dynamics of SNP have been studied by tIR spectroscopy in solution, which has provided insight to the photoinduced metal-nitrosyl linkage isomer and the dynamics of the photodissociation products in both the ν_{NO} and ν_{CN}

stretching regions. [16] Little is known about the relationship between the two ground state vibrations and the excited state metal-to-ligand charge transfer (MLCT). Although the two ground state vibrations may not necessarily be coupled to one another, it is still unknown how each contributes to the MLCT and whether the two vibrations are coupled through the MLCT. Furthermore, relatively little is known about the effect of solvent on vibronic coupling in SNP.

2D VE has been demonstrated as a useful method for investigating the vibronic coupling in molecules that undergo charge transfer, such as an MLCT. [2, 17] The cross peaks accessed by 2D VE report on dipole orientations and vibronic coupling strength. A 2D VE experiment generally results in two types of spectral features. The first is a ground state bleach (GSB) shown by the double-sided Feynman diagram in Figure 4.12(b) and the positive spectral feature shown in Figure 4.12(c). In the double-sided Feynman diagrams, the time axis is vertical from bottom to top. "g,0" represents the vibronic eigenstate $|g,0\rangle$, which is the 0th level vibration (0) in the ground electronic state (g). Arrows represent electric field interactions. After the first interaction in both the GSB and ESA signals, there is a coherence between the $|g,0\rangle$ and $\langle g,1|$ vibronic eigenstates, which oscillates at the frequency difference between the two eigenstates. The coherence is allowed to propagate over τ_1 before the second electric field interaction (second pump pulse), which can either collapse the coherence back to a population over τ_2, or create a new coherence with another vibration. The third arrow represents the interaction with the probe pulse electric field, and creates a new coherence which is then detected as the signal (purple arrow). The GSB depicted in Figure 4.12 occurs at the ω_1 frequency corresponding to the ground state vibration and is detected at the fundamental electronic excitation frequency, ω_{eg}. The second spectral feature is a negative excited state absorption (ESA), which is shown in Figures 4.12(b,c). The ESA is detected at ω_{eg} minus the difference in frequency between the ground and excited state vibrations. More vibronic pathways than the two shown in Figure 4.12 are possible, however, and the peaks from each pathway frequently overlap in ω_3 due to broad electronic transitions.

One method to help deconvolute congested spectra is polarization-selective 2D VE.

Polarization-selective experiments can be performed to suppress or enhance pathways and aid in vibronic pathway identification. [18, 19] In particular, polarization-selective 2D VE has been used to extract relative orientations of cyanide stretches and a metal-to-metal charge transfer (MMCT) in a mixed-valence iron-ruthenium dimer. [20] In the 2D VE spectrum of a molecule with multiple IR-active vibrations within the bandwidth of the pump pulse, many pathways are possible; both vibrations can couple to the electronic transition and can potentially couple to one another through the electronic transition. Peaks often lie close to one another and overlap in the detection frequency axis (ω_3).

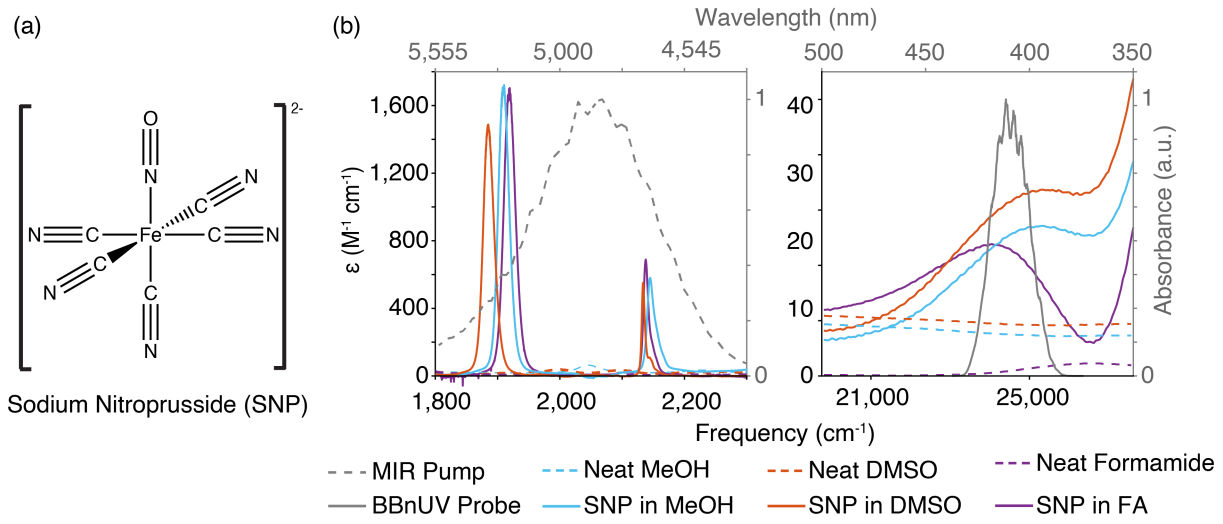

Figure 4.11. a) Sodium nitroprusside structure. The iron center has a charge of +2. b) FTIR and UV-Vis spectra of SNP in methanol (MeOH, blue), dimethyl sulfoxide (DMSO, orange), and formamide (FA, purple). Solvent-subtracted spectra and neat solvent spectra are shown by solid and dashed lines, respectively.

2D VE experiments on SNP in a series of three solvents — methanol (MeOH), dimethyl sulfoxide (DMSO), and formamide (FA) — show that different solvents and experimental conditions cause complicated spectral effects. For SNP in each solvent, the observed spectral features shift in ω_1 and exhibit different line shapes and intensities. Following further analysis, the detected signals could have the potential to reveal valuable information about the vibronic landscape of SNP and will elucidate the role that ground state vibrations play

in the MLCT, but may require cleaner data and some modeling work.

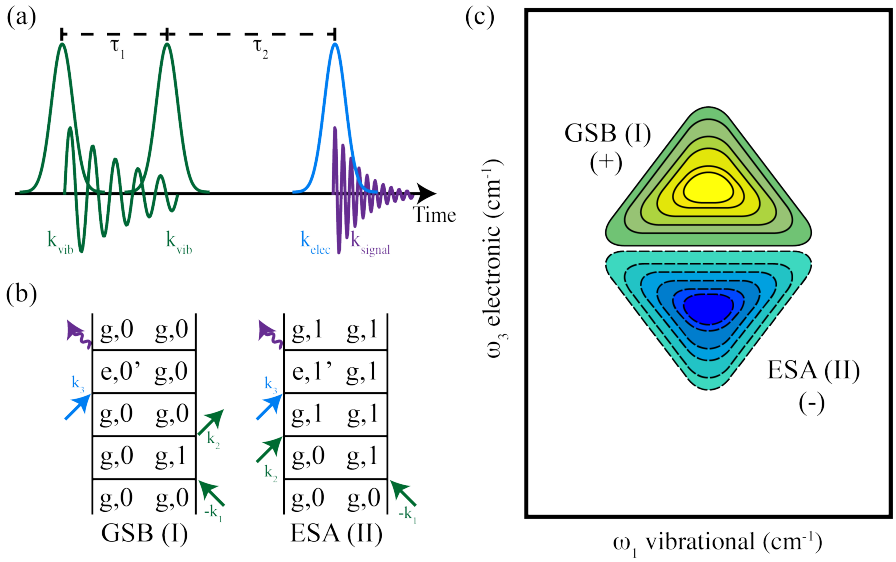

Figure 4.12. a) 2D VE pulse sequence. Two vibrationally resonant MIR pump pulses are separated by time delay, τ_1, and are followed by an electronically resonant probe pulse after time delay, τ_2. b) Double-sided Feynman diagrams (explained in the main text) for two rephasing pathways. Green corresponds to vibrational pump pulses, blue to the electronic probe pulse, and purple to the vibronic signal detected with the electronically resonant probe. c) Cartoon 2D VE spectrum with signals corresponding to pathways shown in (b).

4.4.2 Methods

The cyanide and nitrosyl stretches in SNP were resonantly excited with a pair of mid-infrared (MIR) pump pulses centered at 4800 nm, separated by a time delay, τ_1 (Figure 4.12(a)). The metal-to-ligand charge transfer (MLCT) transition in SNP was resonantly probed by a broadband near-UV (BBnUV) pulse centered around 405 nm, following a waiting period, τ_2. The resulting vibronic signal was detected with the BBnUV probe and Fourier transformed over the τ_1 time delay between the two MIR pump pulses to construct a 2D plot with x- and y-axes corresponding to excitation (ω_1) and detection (ω_3) frequencies, respectively. Polarization-selective spectra were collected by rotating the polarization of the BBnUV probe

pulse 0° or 90° relative to the MIR pump pulses using a half waveplate. The ZZZZ (parallel pumps and probe/signal) or ZZYY (perpendicular pumps and probe/signal) component of the signal was selected using an ultrabroadband linear polarizer (ThorLabs) immediately following the sample area for the polarization-selective experiments. Solutions of SNP in spectrophotometric grade formamide, methanol, and dimethylsulfoxide were prepared at 233 mM, 235 mM, and 225 mM, respectively, for each experiment. Sample was continually refreshed by flowing in the Harrick sample cell with a 50 µm thick teflon spacer.

The current table layout (Coherent and Light Conversion) is described in great detail in earlier sections of this chapter and in Chapter 2. For the previous layout (Spectra-Physics), a 1 kHz regenerative amplifier (Spitfire Pro) was pumped by an Empower laser and seeded with the output of the MaiTai oscillator to produce ≈50 fs pulses centered at 800 nm. The amplified output was split and one arm entered the visible probe line generation, which is the same in both the old and new schemes. For the pump line, the second arm entered a double-pass near-infrared optical parametric amplifier (NIR OPA) on a breadboard. The output signal and idler pulses entered a home-built difference frequency generator (DFG) to create tunable infrared pulses centered around 4800 nm. See Appendix D for details regarding the layout and alignment of the NIR OPA and MIR DFG.

The MIR pump pulses were focused to a $1/e^2$ diameter of 250 µm and spatially overlapped with the BBnUV probe pulse at the sample area. The BBnUV probe was focused to a $1/e^2$ diameter of 160 µm, and delayed by τ_2 with respect to the second MIR pump pulse. The probe and signal co-propagate following the sample area and were coupled to a multimode optical fiber using a 10X magnification objective lens for all experiments described here.

4.4.3 Results and Discussion

2D VE responses for SNP vary among the three solvents. All spectra (Figures 4.13, 4.14, and 4.15) display a positive feature in ΔT/T (percent change in transmission) between ω_1= 1880 cm^{-1} and 1925 cm^{-1}, which is a GSB at ν_{NO}. There is also a pair of features around ω_1= 2130 cm^{-1}– 2150 cm^{-1}, that arise from a negative ESA and a positive GSB at ν_{CN}. The

ESA in the low energy half of ω_3 and the GSB in the high energy half of ω_3 show different relative intensities for the ZZZZ and ZZYY experiments. The tilt and lineshape of each feature vary and are discussed below.

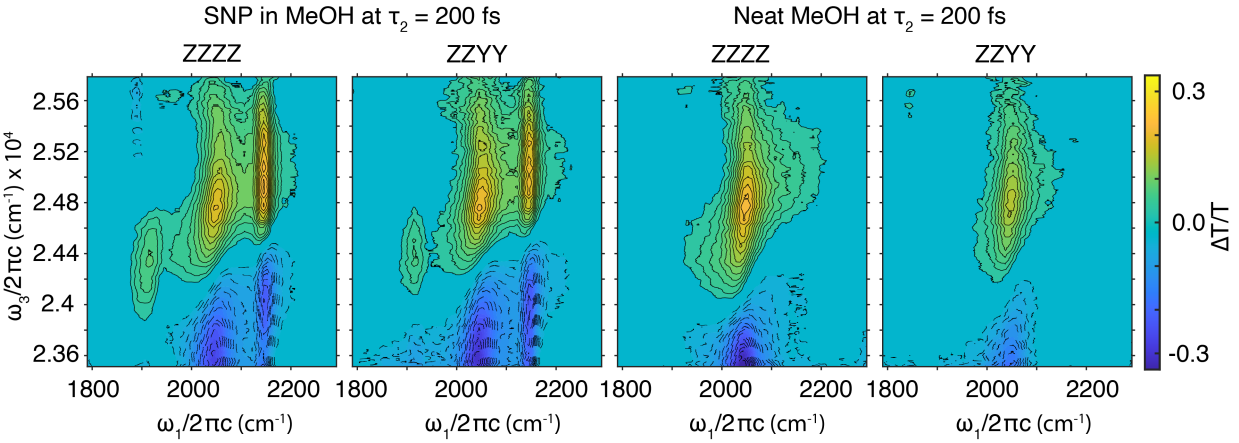

Figure 4.13. Polarization selective 2D VE spectra of SNP in methanol at τ_2= 200 fs. Neat solvent spectra are shown on the right hand side. All spectra are plotted with the same color bar scale and are normalized by the probe. Contours drawn every 5%, from 10–100%, with 100% being the maximum of the SNP ZZZZ spectrum (far left). Solvent and sample spectra were collected under the same experimental conditions, and can be directly compared.

Solvent effects on the behavior of SNP are clearly visible, even in the ground state vibrational spectra, as seen in the frequencies of the NO stretch in the linear FTIR spectra shown in Figure 4.11(b). This solvent dependence becomes even more noticeable in the 2D VE responses of SNP between solvents. At ω_1 = 2050 cm^{-1} in the MeOH 2D VE spectra, a positive and negative feature arise (Fig. 4.13). The 2D VE spectra of DMSO (Fig. 4.14) show a pair of two positive features and one or two negative features in the center of the ω_1 axis. Note that the responses of both MeOH and DMSO are surprisingly strong given the low intensity of their FTIR spectra in the region of interest. The feature in the MeOH FTIR spectrum (Figure 4.11(b)) at 2053 cm^{-1} has been identified as an overtone of the C—O stretching band. [21] The features in the DMSO FTIR spectrum around 1950 cm^{-1} – 2100 cm^{-1} have been attributed to overtones of the S=O symmetric stretching mode and CH_3

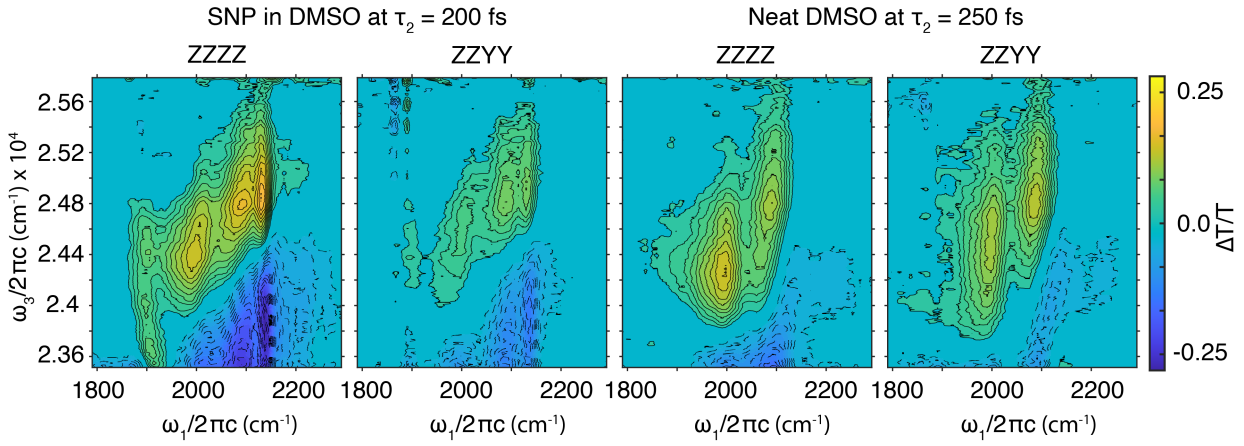

Figure 4.14. Polarization selective 2D VE spectra of SNP in dimethylsulfoxide at τ_2= 200 fs. Neat solvent spectra are shown on the right hand side. All spectra are plotted with the same color bar scale and are normalized by the probe. Contours drawn every 5%, from 10–100%, with 100% being the maximum of the SNP ZZZZ spectrum (far left). Solvent and sample spectra were collected under the same experimental conditions, and can be directly compared.

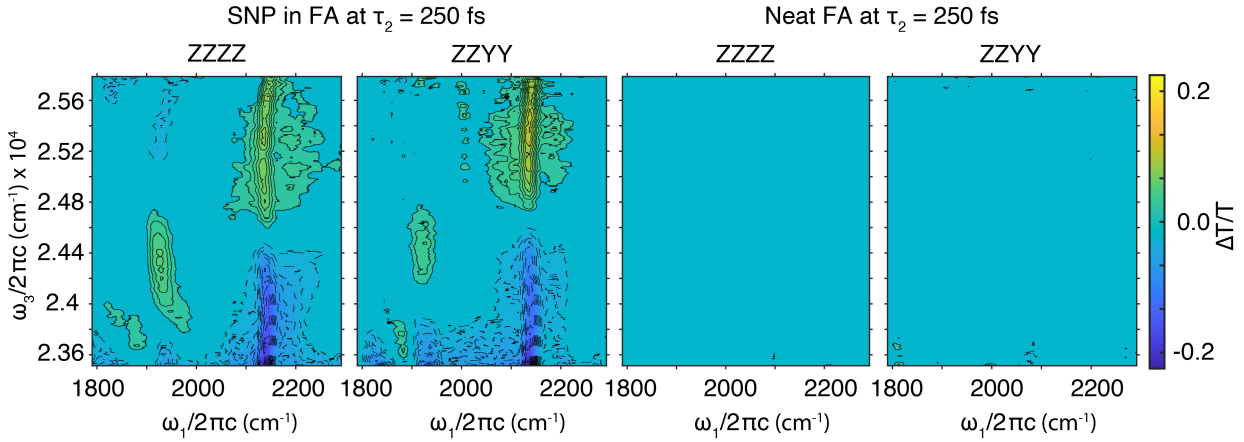

Figure 4.15. Polarization selective 2D VE spectra of SNP in formamide at τ_2= 250 fs. Neat solvent spectra are shown on the right hand side. All spectra are plotted with the same color bar scale and are normalized by the probe. Contours drawn every 5%, from 10–100%, with 100% being the maximum of the SNP ZZZZ spectrum (far left). Solvent and sample spectra were collected under the same experimental conditions, and can be directly compared.

rocking modes. [22] All three solvents absorb very little at 400 nm, yet display distinctive features in the 2D VE spectrum. Formamide has a very small nonresonant response after $\tau_2 = 250$ fs, which quickly decays. The frequencies of three spectral features from SNP shift in ω_1 depending on solvent, and the ω_3 position of the node between the ν_{CN} GSB and ESA features also appears to vary with solvent. These results suggest that coupling may occur between SNP and the solvent, depending on the solvent polarity.

The maximum signal intensity with respect to the pump frequency is observed to vary at different detection frequencies. The line shape appears to depend on solvent, delay time, and peak identity. For example, the ν_{NO} GSB peak generally has a constant slope, while the shape of the ν_{CN} ESA appears to be quadratic or even cubic. The slope of most features (looking at tilt in ω_3 over ω_1) tends to be steeper at earlier times, but may depend on the solvent as well. These lineshapes indicate that peaks could have unequal contributions from rephasing and non-rephasing vibronic pathways and are likely related to the system's vibronic dephasing. The tilt and curvature of the 2D VE features could also be caused by solvent effects or competing ESA and GSB pathways that overlap in ω_3. Further analysis and fitting of the line shapes will help elucidate the factors influencing each each peak shape.

Identifying the pathways that give rise to the observed features in each set of spectra is complicated by the broad electronic transition in ω_3. The analysis done by Gaynor et al. for determining which peaks correspond to which transitions in single mode vibronic spectroscopy can also provide a starting point for identifying transitions in a 2D vibronic spectrum. [23] However, there are many more potential features which can arise in a multi-mode 2D VE spectrum. [18, 19] Spectral features can occur at the frequency of either ground state vibration in ω_1, and are detected at ω_{eg} plus or minus combinations of ground and excited state vibrational energy differences between one or both modes, resulting in tens of different possible features. Future analysis could incorporate fitting line shapes to estimate peak splittings and identify the vibronic pathways accessed in each spectrum.

Solvent dependence in 2D VE remains a challenging experimental consideration and will require a non-negligible amount of study in the future to fully understand. The 2D VE

signal of SNP is clearly dependent on both solvent identity and experimental polarization, although the preliminary data shown here as an example lacks the resolution to discuss the exact effects of solvent identity and polarity. The 2D line shapes may report on vibronic dephasing, solvent effects, and overlapping vibronic pathways in the detection frequency axis. Solvent responses for methanol and dimethyl sulfoxide are not only stronger than expected, but gain intensity between neat solvent spectra and solution spectra. One cause for this could be overlapping solute and solvent peaks, giving the appearance of increased intensity in the 2D VE solvent features. Further analysis will be required to conclusively determine the vibronic information accessed by the solvent-dependent two-dimensional vibrational-electronic spectroscopy experiments on SNP.

4.5 Other Troubleshooting

Some 2D VE experimental attempts have yielded strange results, and during others, we have encountered unexpected challenges related to data collection and processing codes and the tabletop laser system. They are described below, and several common problem-scenarios are addressed as well.

4.5.1 Solvent Heating

Using the new laser system and the KTA crystal with the DFG centered at ≈2100 cm^{-1}, we encountered some strange effects in the 2D VE spectra. Currently, our best guess is that the solvent was heating. Over all τ_2 times, there is a positively signed 2D VE signal. Figures 4.16(a-c) and (d-e) show 2D VE spectra of 60 mM $K_3[Fe^{III}(CN)_6]$ in formamide and neat methanol, respectively, at τ_2 = -500, 0 and 500 fs. The signals at positive and negative times are very similar for each. In the $K_3[Fe^{III}(CN)_6]$ spectra, the positive feature appears in ω_1 where there is a ground state cyanide stretching mode (≈2107 cm^{-1}). In the neat MeOH spectra, there is a positve feature slightly to the red, at around 2050 cm^{-1}, which corresponds to an overtone in the ground state vibrational spectrum of MeOH. However, the sign of this signal does not match previous experiments. From earlier experiments, where

there was no signal at negative τ_2 delays (described in Section 4.4), we expect a positively and a negatively signed feature. This only appeared to be a problem in protic solvents like MeOH and formamide. There was no effect in anhydrous CCl_4 under the same experimental conditions. The pump and probe spot sizes and sample thickness were the same as those described in Chapter 2. The pump energy was ≈470 nJ per IR pulse, which is not terribly high compared to the pump energies used in other VE experiments. It is possible that the narrow bandwidth of the IR spectrum produced by the KTA crystal at 2100 cm^{-1} increased the peak power more than we estimated, causing this effect.

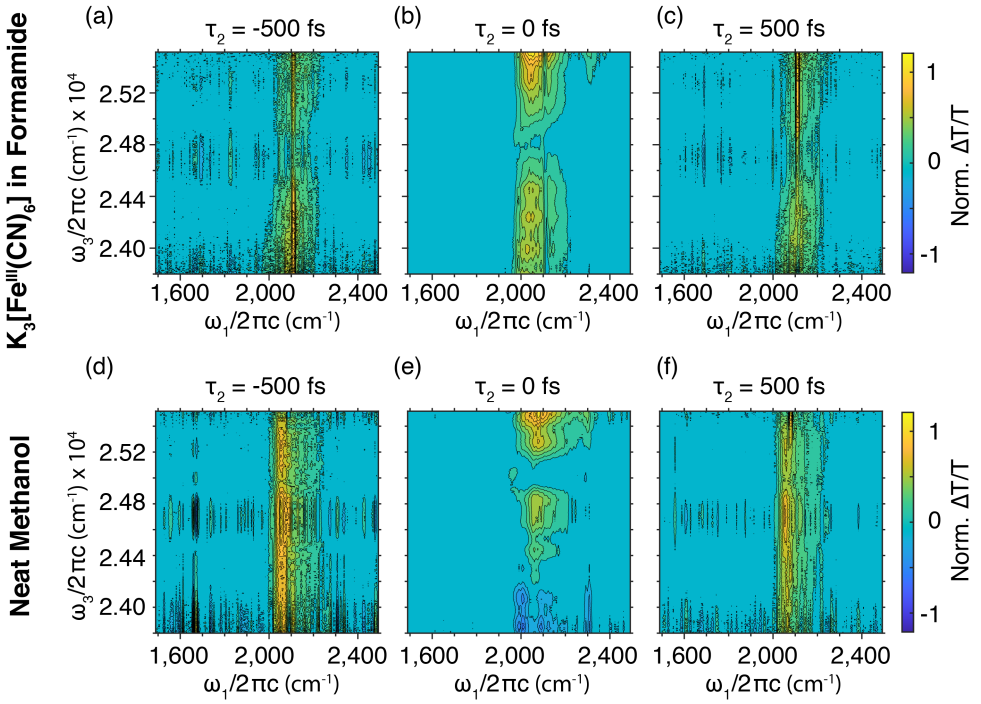

Figure 4.16. 2D VE spectra of $K_3[Fe^{III}(CN)_6]$ in formamide and neat MeOH. (a-c) 60 mM $K_3[Fe^{III}(CN)_6]$ in formamide at τ_2 = -500, 0, and 500 fs. (d-f) Neat MeOH at τ_2 = -500, 0, and 500 fs.

4.5.2 Double Pulsing

The new (N)DFG was installed with two crystals (outlined in the manual). They were made of KTA (potassium titanyl arsenate) for IR wavelengths shorter than ≈4,500 nm and GaSe (gallium selenide) for wavelengths from ≈4,500–10,000 nm. GaSe is a particularly difficult material to work with; it is too delicate to apply an anti-reflective coating and the crystal structure makes it difficult to cut with the two surfaces wedged. This means that GaSe crystals with decent parallelism will create an internal reflection of the IR that is generated in the crystal. In a time-resolved spectroscopy experiment that uses the IR as a pump, such as 2D VE, this (unsurprisingly) is a massive problem. We found a 25% ghost pulse in the IR line at 2.3 ps after the main pulse. When attempting to take 2D VE data, this caused a confusing oscillatory effect in the Fourier transformed spectrum at $\tau_2 = 500$ fs. Fig. 4.17(a) shows the 2D VE spectrum of 60 mM $K_3[Fe^{III}(CN)_6]$ in spectrophotometric grade formamide at $\tau_2 = 500$ fs. There are oscillations across the bandwidth of the pump caused by interference from the ghost pulses. Fig. 4.17(b) shows a step scan interferogram of the IR pulse, clearly demonstrating a 25% ghost pulse in the IR. A second harmonic generation (SHG) autocorrelation of the amplifier output (Coherent Astrella) showed that the double pulse appeared only after the TOPAS and DFG. There was no double pulse in the IR when using the KTA crystal, confirming that the GaSe crystal was the source of the double pulsing.

4.5.3 Beam Instability or Low Power

If any output becomes unstable, or is very challenging to bring to a benchmark power, check the line for burned optics. If the MIR becomes unstable, it is very likely that a crystal in the TOPAS or DFG is burned. Figure 4.18 (right) shows an example of white light generated through a burned sapphire. Poor white light generation contributes to instability and noise in the pulse, and will decrease the overall output of the TOPAS and DFG. The $AgGaS_2$ (AGS) crystal used to generate longer IR wavelengths in the DFG has a lower damage threshold than KTA or GaSe, so it will eventually need to be replaced after a certain number of hours

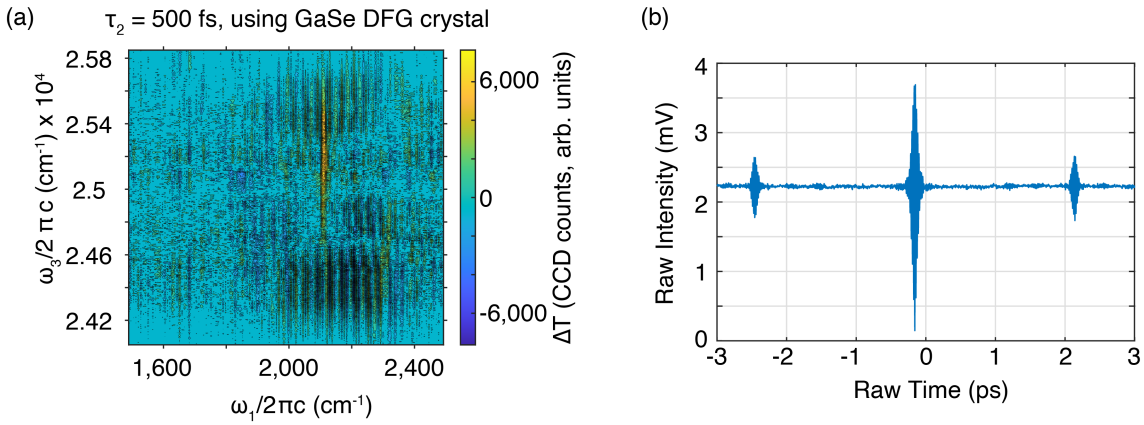

Figure 4.17. 2D VE spectrum and step scan time domain with IR double pulse. a) 2D VE spectrum of 60 mM $K_3[Fe^{III}(CN)_6]$ in formamide at $\tau_2 = 500$ fs with a double pulse in the IR pumps. b) Step scan time domain on the single channel MCT detector showing a 25% ghost pulse in the IR.

of exposure to the intense signal and idler beams. Fused silica plates and protected silver mirrors in the BBnUV line also burn frequently. Translate or rotate these optics as needed to avoid burn spots.

Figure 4.18. Left: Example of good white light generation through a sapphire. (The camera has slightly amplified the red ring around the white core from what the human eye can see.) Right: Example of white light generation through a burned sapphire.

4.5.4 Low Voltage Reading from SC-MCT

Double check that the MCT is well-cooled with liquid nitrogen. Check that the BNC's and their connectors are all functioning properly. (Sometimes it takes some jiggling to get them to work.) Check that the wires on the power supply and pre-amp for the MCT are not missing connections, and make sure that it is insulated from the laser table by some foam and is not touching other cords or electronics. See Section 4.3.3 for details regarding the electronic settings on the single channel MCT. If the electronic settings are correct, and none of the above helps, check the HeNe/IR overlap and try realigning into the MCT from scratch. This means block the IR, remove all the polarizers and ND filters, realign the HeNe on a bolt row and through the focusing lens, and check that it hits the window of the MCT squarely. Sometimes the pixel picks up stray reflections which are weak and noisy compared to the main beam. Replace the beam-attenuating optics, taking care to block their back-reflections, and try again. When aligning the SC-MCT, always look at the signal triggered on an oscilloscope. It is much easier to tell when the pixel is saturated versus looking at the signal on the lock-in.

4.5.5 Collection vi Problems

While collecting 2D VE data in the hopes of replicating previous experiments on $K_3[Fe^{III}(CN)_6]$ in formamide to finish setting up the new laser system (March 2024), we found that the sign of the signal on individual scans flipped arbitrarily. However, the first scan was always the correct sign. To fix this, I rewired the collection vi in LabVIEW to reinitialize the CCD after each minute of data is collected. Our best guess was that slightly different electronic settings with the new laser system combined with a newer and faster data collection computer caused a shot or two to drop which affected the τ_1 binning and the phase of the Fourier transform in the processed data. If something in your data looks odd, plot scans individually instead of averaged together to make sure that data are consistent scan to scan.

4.6 Summary

Hopefully, any potential problems can be avoided by following the guidance in the rest of this chapter. Realistically, that won't be possible. In that case, I can offer several pieces of advice. First, look at the references in this chapter. Second, read old lab notebooks. Trevor Courtney's are particularly useful and especially detailed, and mine (paper and electronic) are more up to date and will fill in the gaps. Last, and most importantly, don't be afraid to try something new. Even if it doesn't work, changing something in the experiment might help you figure out what was wrong in the first place. It could even lead to better results. Just be sure to document the changes you make and describe how well they worked so that the next person can come along and try.

BIBLIOGRAPHY

[1] Z. W. Fox, T. J. Blair, R. B. Weakly, T. L. Courtney, and M. Khalil, "Implementation of Continuous Fast Scanning Detection in Femtosecond Fourier-Transform Two-Dimensional Vibrational-Electronic Spectroscopy to Decrease Data Acquisition Time," *Review of Scientific Instruments*, vol. 89, pp. 113104–1–7, Nov. 2018.

[2] T. L. Courtney, Z. W. Fox, K. M. Slenkamp, and M. Khalil, "Two-dimensional vibrational-electronic spectroscopy," *The Journal of Chemical Physics*, vol. 143, p. 154201, Oct. 2015.

[3] J. D. Gaynor, A. Petrone, X. Li, and M. Khalil, "Mapping vibronic couplings in a solar cell dye with polarization-selective two-dimensional electronic-vibrational spectroscopy," *The Journal of Physical Chemistry Letters*, vol. 9, pp. 6289–6295, 11 2018.

[4] K. C. Robben and C. M. Cheatum, "Increasing Pump–Probe Signal toward Asymptotic Limits," *The Journal of Physical Chemistry B*, vol. 127, pp. 4694–4707, Jun. 2023.

[5] M. Cho, "Molecular photothermal effects on time-resolved IR spectroscopy," *The Journal of Chemical Physics*, vol. 157, p. 124201, Sep. 2022.

[6] M. Cho, "Molecular Photothermal Effects on Time-Resolved IR Spectroscopy: Solute-Solvent Intermolecular Energy Transfer," *Journal of Physical Chemistry B*, vol. 127, pp. 300–307, Jan. 2023.

[7] M. Cho, "Molecular photothermal effects, diffusion, and sample flow in time-resolved spectroscopy and microscopy," *The Journal of Chemical Physics*, vol. 159, p. 224104, Dec. 2023.

[8] J. D. Gaynor, *Correlated Electronic and Vibrational Motion: A Direct Perspective Through Multidimensional Electronic-Vibrational Spectroscopy.* PhD thesis, University of Washington, 2019.

[9] J. W. Sandwisch, *Investigation of the Role Nonadiabatic Energy Relaxation Plays in Excited State Intramolecular Proton Transfer using Multidimensional Electronic-Vibrational Spectroscopy.* PhD thesis, University of Washington, 2023.

[10] Newport, "Application Note: Prism Compressor for Ultrashort Laser Pulses," *Newport*, vol. 29, no. 1, pp. 1–4, 2006. ISBN: 1044-0305 (Print).

[11] *Newton Hardware Guide*, 2022.

[12] S. Yeremenko, A. Baltuška, F. de Haan, M. S. Pshenichnikov, and D. A. Wiersma, "Frequency-resolved pump–probe characterization of femtosecond infrared pulses," *Optics Letters*, vol. 27, no. 13, p. 1171, 2002.

[13] D. McMorrow and W. T. Lotshaw, "The frequency response of condensed-phase media to femtosecond optical pulses: spectral-filter effects," *Chemical Physics Letters*, vol. 174, pp. 85–94, Oct. 1990.

[14] M. Khalil, O. Golonzka, N. Demirdöven, C. J. Fecko, and A. Tokmakoff, "Polarization-selective femtosecond Raman spectroscopy of isotropic and anisotropic vibrational dynamics in liquids," *Chemical Physics Letters*, vol. 321, pp. 231–237, Apr. 2000.

[15] J. F. Brookes, K. M. Slenkamp, M. S. Lynch, and M. Khalil, "Effect of solvent polarity on the vibrational dephasing dynamics of the nitrosyl stretch in an Fe^{II} complex revealed by 2D IR spectroscopy," *The Journal of Physical Chemistry A*, vol. 117, pp. 6234–6243, 7 2013.

[16] M. S. Lynch, M. Cheng, B. E. Van Kuiken, and M. Khalil, "Probing the Photoinduced Metal–Nitrosyl Linkage Isomerism of Sodium Nitroprusside in Solution Using Transient Infrared Spectroscopy," *The Journal of the American Chemical Society*, vol. 133, pp. 5255–5262, Apr. 2011.

[17] T. L. Courtney, Z. W. Fox, L. Estergreen, and M. Khalil, "Measuring Coherently Coupled Intramolecular Vibrational and Charge-Transfer Dynamics with Two-Dimensional Vibrational-Electronic Spectroscopy," *The Journal of Physical Chemistry Letters*, vol. 6, pp. 1286–1292, Apr. 2015.

[18] J. D. Gaynor, R. B. Weakly, and M. Khalil, "Multimode two-dimensional vibronic spectroscopy. I. Orientational response and polarization-selectivity," *The Journal of Chemical Physics*, vol. 154, p. 184201, 2021.

[19] R. B. Weakly, J. D. Gaynor, and M. Khalil, "Multimode two-dimensional vibronic spectroscopy. II. Simulating and extracting vibronic coupling parameters from polarization-selective spectra," *The Journal of Chemical Physics*, vol. 154, p. 184202, 2021.

[20] Z. W. Fox, T. J. Blair, and M. Khalil, "Determining the Orientation and Vibronic Couplings between Electronic and Vibrational Coordinates with Polarization-Selective

Two-Dimensional Vibrational-Electronic Spectroscopy," *The Journal of Physical Chemistry Letters*, vol. 11, pp. 1558–1563, 2020.

[21] L.-H. Xu, A. M. Andrews, and G. T. Fraser, "Study of the overtone C—O stretching band of methanol by multiple resonance spectroscopy," *The Journal of Chemical Physics*, vol. 103, pp. 14–19, 1995.

[22] S. Chakrabarty, S. H. Deshmukh, A. Barman, S. Bagchi, and A. Ghosh, "On-off infrared absorption of the S=O vibrational probe of dimethyl sulfoxide," *The Journal of Physical Chemistry B*, vol. 126, pp. 4501–4508, 2022.

[23] J. D. Gaynor and M. Khalil, "Signatures of vibronic coupling in two-dimensional electronic-vibrational and vibrational-electronic spectroscopies," *TheJournal of Chemical Physics*, vol. 147, p. 094202, 2017.

Chapter 5

CONCLUSIONS, OUTLOOK, AND FUTURE DIRECTIONS

The field of ultrafast multidimensional spectroscopy has many possible future directions. Ongoing improvements to theoretical techniques, experimental techniques, and ultrafast optics are interwoven with one another, and they all impact our ability to extract novel and meaningful information from chemical reactions. Theory and experiment inform one another; calculations are necessary to interpret experimental results, and experiments can support or discredit theoretical and computational methods. Without the ongoing improvements to the field of ultrafast nonlinear optics, performing experiments with increasingly high pulse energy, broad bandwidth, and stability would not be possible. The experiments detailed in this thesis would have been infeasible several decades ago simply because the necessary optics, equipment, and theoretical frameworks did not yet exist. My contribution to the experimental side of ultrafast multidimensional spectroscopy will push the field towards a deeper understanding of intramolecular hydrogen bonding and proton transfer. It will also help 2D VE spectroscopy become a more common and accessible technique to probe vibronic coupling in solution. The observation of coherent low-frequency vibrations coupled to the high-frequency OH stretch and electronic transition in HBQ opens further questions about what, if any, effect those low frequency modes have on the ultrafast ESIPT. It is critical to consider nuclear motion in the context of being coupled to electronic motion, and vice versa. The results of the studies on HBQ in this dissertation emphasize that importance.

The work described in Section 4.4 leaves many open questions for the development of 2D VE spectroscopy. Is there a significant difference in the effect of different solvents on the vibronic dephasing times for each ground state vibration coupled to the electronic transition in SNP? What is the difference for each vibration and the difference in vibronic coupling

strength? A deeper understanding of solvent responses in 2D VE spectroscopy will be required to understand these signals. Simply performing a solvent subtraction is not sufficient to disentangle overlapping solvent and solute spectral features, especially if the solvent features gain or lose intensity through interaction with the solute.

One of the most exciting frontiers of VE spectroscopy is its extension to three dimensions. 2D experiments allow the observation of coupling between ground state vibrations and the electronic transition, but lack information on any low-frequency coherences simultaneously excited by the pump pulse. 3D VE experiments gain frequency resolution of τ_2 to ω_2, which can reveal the low-frequency modes that are also coupled to the electronic transition. 3D EV experiments have shown vibronic coherences in a solar cell dye [1] and 3D ES experiments have been used to observe vibronic coherence transfer in the bacterial reaction center [2], but no successful VE analog has been reported. The promising preliminary 2D VE spectra of HBQ discussed in Chapter 2 indicate signs of low-frequency coherences in τ_2, likely matching those seen in the 1D VE spectra. Connecting the vibronic coupling under different areas of the resonantly excited high-frequency ν_{OH} mode to both the electronic excitation and the coherently excited low frequencies will reveal where the relevant low- and high-frequency modes couple to the electronic excitation. In this way, we could view exactly which low- and high-frequency modes couple to the electronic absorption spectrum. Of course, this experiment is limited by time-resolution, probe bandwidth, and relatively weak 2D signal levels. Continued development of the 2D VE experiment will be necessary to successfully collect 3D VE data, and further calculations and modeling will be required to understand the data. Transient 2D IR experiments, developed by Bredenbeck and Hamm [3, 4], could also be used to reveal which ground state vibrational modes couple to excited state vibrations in HBQ, thereby connecting ground and excited state vibrations coupled through the $S_1 \leftarrow S_0$ transition.

Another exciting area of investigation on HBQ would involve synthetically tuning the molecule [5–7] with electron donating or withdrawing groups on the conjugated backbone to observe their effects on hydrogen bonding and proton transfer. Performing the VE and

X-ray experiments described in this dissertation with polar solvents that would interfere with the intramolecular hydrogen bond would also prove to be an illuminating study. As an intramolecular hydrogen bond is weakened, how is the vibronic coupling affected, and does the coupling of low-frequency modes change? What are the changes to the local electronic environments of the proton donor and acceptor? I look forward to learning the answers to these questions as the field of ultrafast spectroscopy continues to progress.

BIBLIOGRAPHY

[1] J. D. Gaynor, J. Sandwisch, and M. Khalil, "Vibronic coherence evolution in multidimensional ultrafast photochemical processes," *Nature Communications*, vol. 10, pp. 1–9, 2019.

[2] V. R. Policht, A. Niedringhaus, R. Willow, P. D. Laible, D. F. Bocian, C. Kirmaier, D. Holten, T. Mančal, and J. P. Ogilvie, "Hidden Vibronic and Excitonic Structure and Vibronic Coherence Transfer in the Bacterial Reaction Center," *Science Advances*, vol. 8, pp. 1–10, 2022.

[3] J. Bredenbeck, J. Helbing, and P. Hamm, "Labeling Vibrations by Light: Ultrafast Transient 2D-IR Spectroscopy Tracks Vibrational Modes during Photoinduced Charge Transfer," *The Journal of the American Chemical Society*, vol. 126, no. 4, pp. 990–991, 2004.

[4] P. Hamm, J. Helbing, and J. Bredenbeck, "Two-Dimensional Infrared Spectroscopy of Photoswitchable Peptides," *Annual Review of Physical Chemistry*, vol. 59, pp. 291–317, 2008.

[5] S. Hristova, G. Dobrikov, F. S. Kamounah, S. Kawauchi, P. E. Hansen, V. Deneva, D. Nedeltcheva, and L. Antonov, "10-Hydroxybenzo[*h*]quinoline: Switching Between Single- and Double-Well Proton Transfer Through Structural Modifications," *RSC Advances*, vol. 5, pp. 102495–102507, 2015.

[6] H. Marciniak, S. Hristova, V. Deneva, F. S. Kamounah, P. E. Hansen, S. Lochbrunner, and L. Antonov, "Dynamics of Excited State Proton Transfer in Nitro Substituted 10-Hydroxybenzo[*h*]quinolines," *Physical Chemistry Chemical Physics*, vol. 19, no. 39, pp. 26621–26629, 2017.

[7] S. Chai and S.-L. Cong, "Excited State Intramolecular Proton Transfer and Substituent Effect of 10-Hydroxybenzo[*h*]quinoline: A Time-Dependent Density Functional Theory Study," *Computational and Theoretical Chemistry*, vol. 1034, pp. 80–84, 2014.

Appendix A

SUPPORTING INFORMATION: OBSERVING VIBRONIC COUPLING IN A STRONGLY HYDROGEN BONDED COMPLEX WITH COHERENT MULTIDIMENSIONAL VIBRATIONAL-ELECTRONIC SPECTROSCOPY

Relevant publications, with the permission of ACS publishing:

- Caroline M. Loe, Srijan Chatterjee, Robert B. Weakly, and Munira Khalil, "Observing Vibronic Coupling in a Strongly Hydrogen Bonded Complex with Coherent Multidimensional Vibrational-Electronic Spectroscopy".

A.1 Experimental Details

Signal linearity with the IR pump power was confirmed for both 1D and 2D VE experiments by integrating the 1D VE signal at $\tau_2 = 300$ fs (outside of the solvent response), across all probe wavelengths. Error bars are shown for recorded pump power for each measurement. Figure A.1 shows the linear relationship between integrated 1D VE signal for HBQ in CCl_4 versus IR pump power. IR spot sizes at the sample area were focused to a $1/e^2$ diameter of 150 µm.

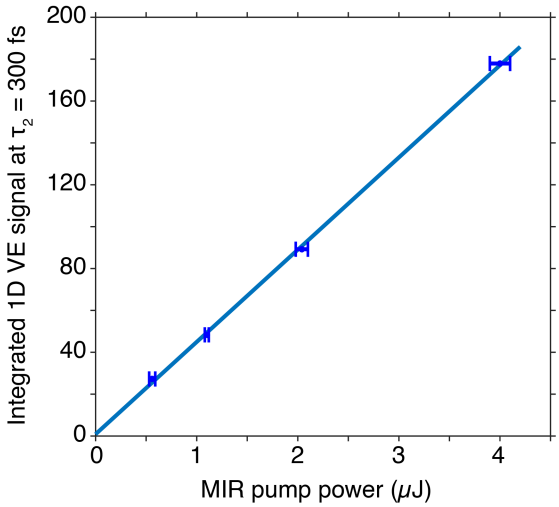

Figure A.1. 1D VE signal of HBQ in CCl_4 versus pump power in µJ.

A.2 1D VE

There are clear oscillations from both solute and solvent in the 1D VE spectra. Cuts at five different frequencies, shown in Fig. A.2, are plotted on the same scale across polarizations and samples, and offset from one another with the corresponding biexponential fit. As shown in main text Fig. 5, the solvent oscillations dominate the 1D VE spectra and a Fourier transform is necessary to determine the signal from HBQ alone. Figure A.3 shows the 1D VE spectra for neat CCl_4 in the time domain and after Fourier transform. The instrument response first

dominates each spectrum and is followed by oscillations. The Fourier transform spectra in ZZZZ and ZZYY (Figs. A.3(c) and A.3(d)) show the three frequencies observed in addition to the 242 and 386 cm^{-1} modes from HBQ. Figure A.4 compares projections of solvent (black and gray, offset by 1) and solution (dark and light blue) spectra over all probe frequencies onto the ω_2 axis. The relative intensities for the absolute values of the three solvent peaks (taken from neat solvent spectra) are 0.28:0.47:1 for ZZZZ and 0.12:0.24:1 for ZZYY. We note that while most of these relative intensities are in close agreement with previously reported values for CCl_4, several are not. Previous experiments reported that relative intensities of Raman active modes in CCl_4 were 0.34:0.47:1 for the ZZZZ spectrum, and -0.18:-0.27:1 for the ZZYY. [1] While the absolute values of the peak intensity at 320 cm^{-1} are close, there are differences for ratios of the 216 cm^{-1} Raman mode in both ZZZZ and ZZYY spectra to the 464 cm^{-1} mode. We attribute the differences to phase shifts in the Fourier transformed surfaces, caused by residual second and third order dispersion in our BBnUV probe pulse and leading to phase flips in the Fourier transformed spectra.

Following Fourier transformation, frequency domain 1D VE spectra are divided by the Fourier transform of the instrument response. Ref. [2] details this method for extracting the contribution of the observed signal that is proportional to the third-order nonlinear response in a pump-probe spectroscopy experiment. Plots of the Fourier transformed instrument response are shown in Fig. A.6 for both ZZZZ and ZZYY.

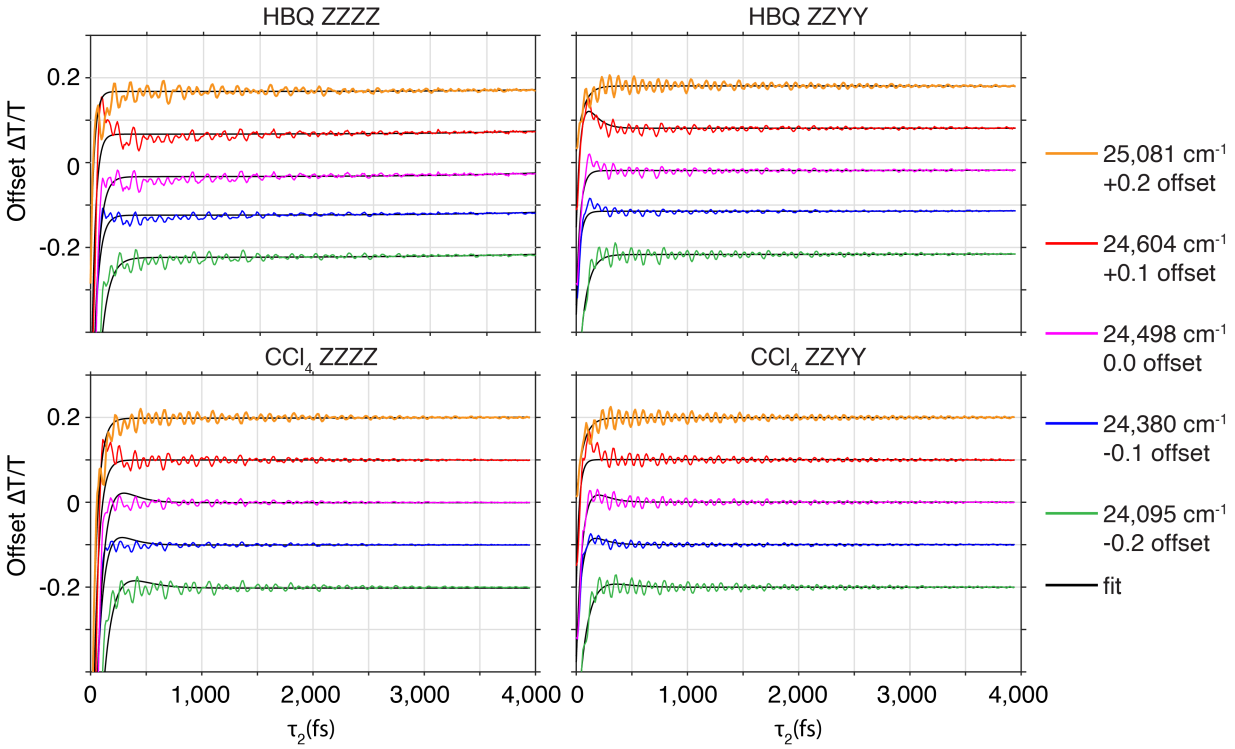

Figure A.2. Biexponential fits to five frequencies over the 1D VE detection range for ZZZZ and ZZYY spectra of HBQ in CCl_4 and neat CCl_4. Frequencies are listed in order of highest to lowest and offset in $\Delta T/T$ for clarity.

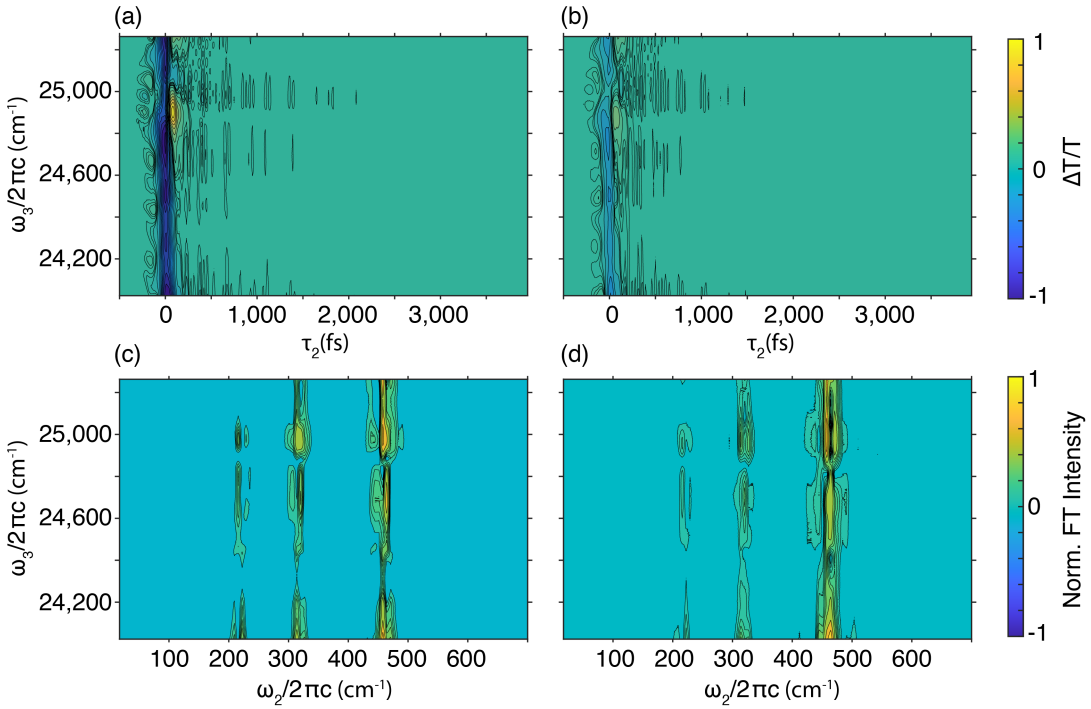

Figure A.3. 1D VE spectra of neat CCl_4 with Fourier transformed correlation maps. a) ZZZZ 1D VE spectrum and b) ZZYY 1D VE spectrum. c) FFT of (a) and d) FFT of (b). Fourier transformed spectra are divided by the Fourier transform of the IRF to yield only the contribution to the observed signal that is proportional to the third order nonlinear response. [2]

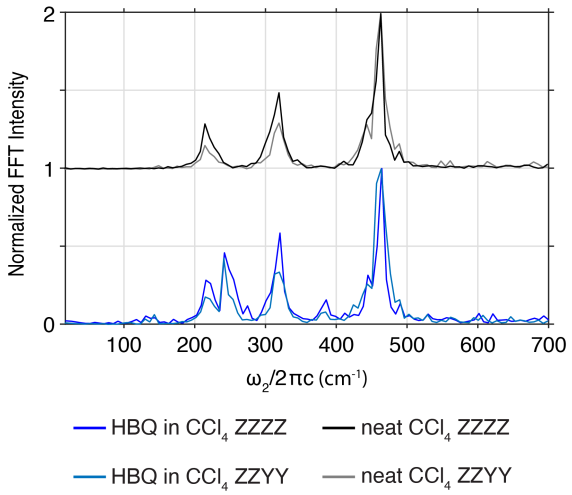

Figure A.4. Projections of 1D VE Fourier transform of neat CCl_4 (black and gray, top, offset by 1) and HBQ in CCl_4 (dark and light blue, bottom). ZZZZ spectra are shown in black and dark blue, while ZZYY spectra are shown in gray and light blue.

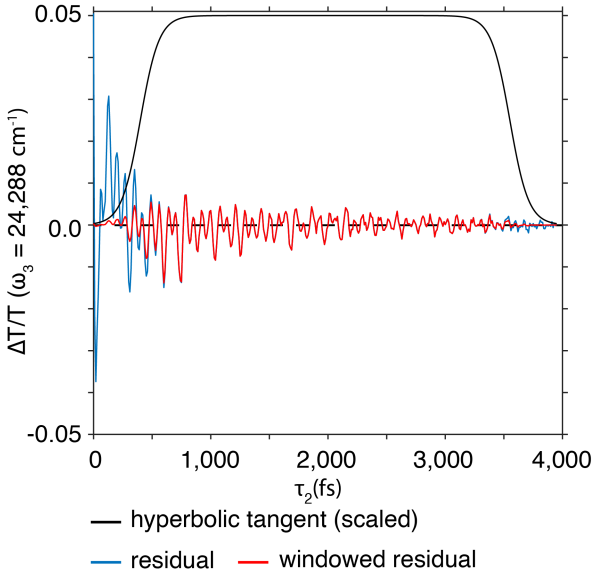

Figure A.5. Hyperbolic tangent windowing function used in 1D VE Fourier analysis (black). The residual at $\omega_3 = 24{,}288$ cm^{-1} for HBQ in the ZZZZ experiment (blue) and the windowed residual used for Fourier transform (red).

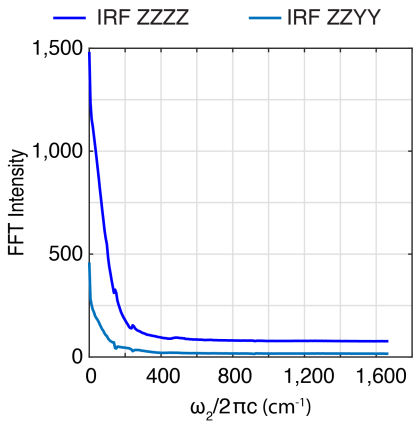

Figure A.6. Fourier transforms of the IRF in ZZZZ (light blue) and ZZYY (dark blue) which were used to normalize FFT spectra. See references [1], [2] for details.

A.3 2D VE

There is some solvent response present in the 2D VE spectra at $\tau_2 = 200$ fs. Figure A.7 shows the neat solvent response at $\tau_2 = 200$, 300, and 350 fs. Spectra were averaged for 10, 9, and 18 minutes respectively. Figure A.8 shows a comparison of the 2D VE projections for HBQ spectra shown in Fig. 2.6 with the ground state FTIR spectrum and the calculated DFT vibrational frequencies with the anharmonic correction (gray sticks). The calculated ν_{OH} mode is at 2717 cm^{-1}. Many of the other calculated frequencies shown are CH stretches, combination modes of low frequencies with the ν_{OH} mode, and combinations of CH and OH modes at lower frequencies.

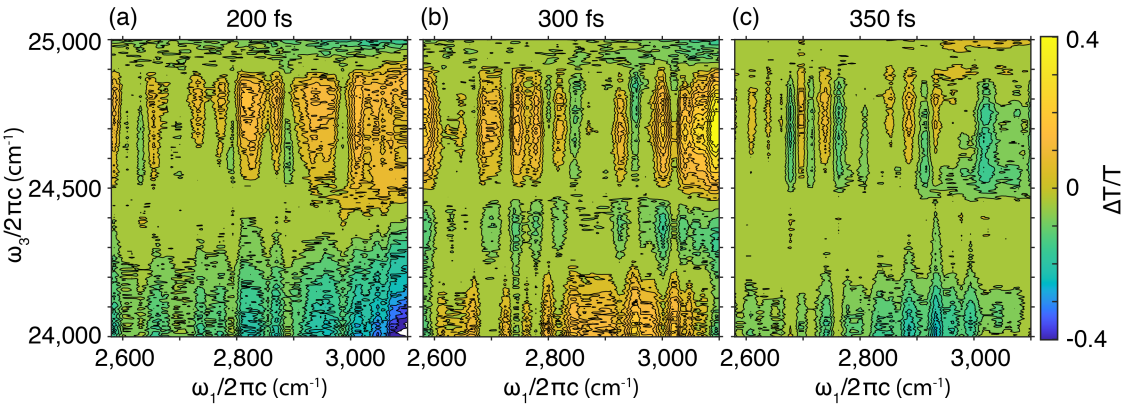

Figure A.7. 2D VE spectra of neat CCl_4 at $\tau_2 = 200$, 300, and 350 fs. Contours are plotted every 10%.

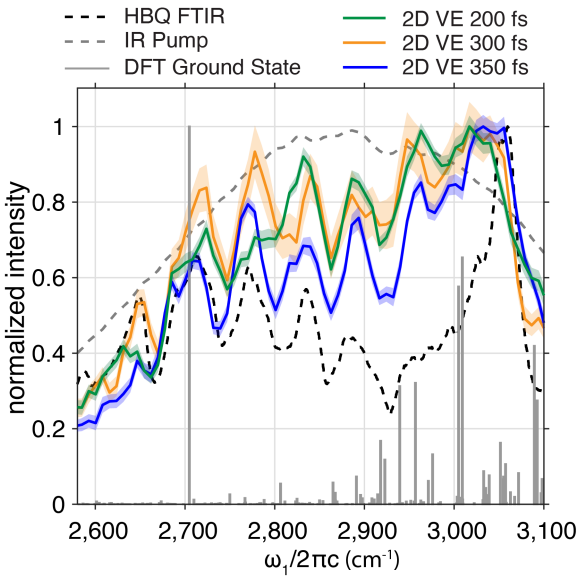

Figure A.8. 2D VE projections onto excitation axis (ω_1) of the ESA feature at τ_2 = 200 fs (green), 300 fs (orange), and 350 fs (blue). Normalized projections are compared to normalized ground state FTIR. The IR pump spectrum is shown in dashed gray, and ground state frequency calculations are shown in solid gray. 2D VE surfaces are shown in the main text in Fig. 2.6.

A.4 DFT Calculations

DFT calculations (from Ref. [3]) reveal the four molecular orbitals involved in the $S_1 \leftarrow S_0$ transition. The $S_1 \leftarrow S_0$ transition has mainly HOMO→LUMO character, but transitions into the LUMO from HOMO-1 and transitions to LUMO+1 from HOMO-1 and HOMO also contribute. As can be seen in the molecular orbital plots (top and left panels, yellow and blue surfaces), the electron density is very delocalized. Difference densities between the orbitals help illustrate the extent of delocalization (purple and teal surfaces). Ground state vibrational frequencies with the anharmonic correction were also calculated for HBQ in CCl_4. Table A.1 lists the fundamental modes (1-66) for HBQ.

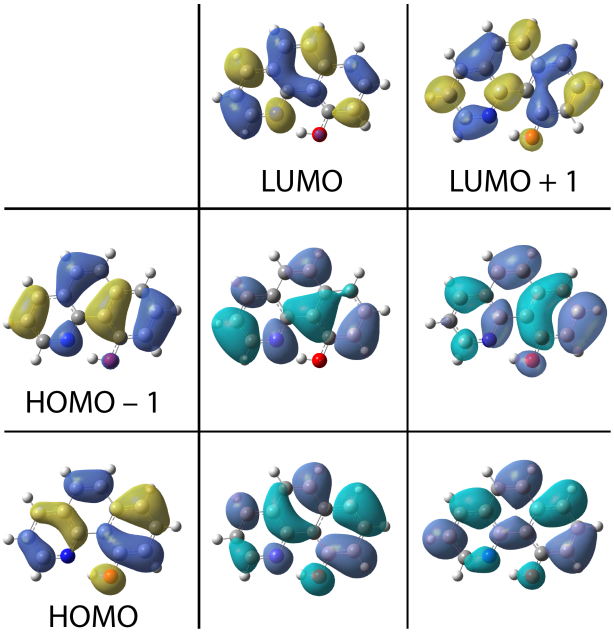

Figure A.9. The four molecular orbitals involved in the $S_1 \leftarrow S_0$ transition (yellow and blue, top and left panels). Occupied molecular orbitals are shown on the left (HOMO, HOMO-1), and unoccupied molecular orbitals are shown on the top (LUMO, LUMO+1). Difference densities show changes to electronic density delocalized across the molecular backbone of HBQ and around the oxygen (proton- and hydrogen bond- donor).

Table A.1. Calculated fundamental frequencies for HBQ in CCl_4. [3]

Mode	ω (Harm., cm^{-1})	ω (Anharm., cm^{-1})	$\Delta\omega$ (cm^{-1})	I (a.u.)	Δ I (a.u.)
1	89.38	86.89	-2.49	1.5881	-1.074
2	112.66	116.7	4.04	0.2042	-0.1116
3	204.65	208.06	3.41	0.025	-0.1934
4	227.39	220.02	-7.37	3.8106	-0.9462
5	249.96	241.81	-8.15	3.3802	-0.7534
6	287.17	290.07	2.9	0.2653	0.1839
7	389.04	386.9	-2.15	2.0223	0.2748
8	412.28	406.51	-5.76	3.9444	-3.2034
9	418.43	416.47	-1.96	0.3972	0.0089
10	485.85	504.1	18.26	0.0069	-0.5771
11	508.3	505.15	-3.15	2.4953	-0.0774
12	512.37	538.21	25.83	2.5573	-1.1259
13	517.78	514.97	-2.81	0.9936	-1.4704
14	556.33	559.13	2.79	0.3594	0.1938
15	579.04	571.72	-7.32	3.7798	-4.0646
16	581.05	596.35	15.3	0.0209	-0.0912
17	640.75	668.6	27.86	0.0975	-0.1137
18	691.94	683.61	-8.33	9.8939	-4.0711
19	726.27	726.78	0.51	50.1921	13.5228
20	729.56	721.78	-7.78	1.2121	-0.6767
21	767.95	761.12	-6.84	2.2068	-28.9357
22	791.94	812.55	20.61	10.997	7.2037
23	815.57	939.82	124.25	0.7705	-9.0449
24	819.07	812.25	-6.82	7.3876	-3.58

Calculated fundamental frequencies for HBQ in CCl_4, continued. [3]

Mode	ω (Harm., cm^{-1})	ω (Anharm., cm^{-1})	$\Delta\omega$ (cm^{-1})	I (a.u.)	Δ I (a.u.)
25	843.1	869.99	26.89	1.3854	-148.1503
26	873.32	788.07	-85.25	22.3678	-3.4019
27	877.04	867.61	-9.43	1.2268	-0.7261
28	892.95	918.68	25.73	5.7116	-0.5644
29	959.67	971.37	11.69	0.9963	-0.4565
30	978.74	1002.6	23.86	1.0122	0.8385
31	985.43	981.86	-3.57	0.1628	-0.4128
32	993.4	1038.18	44.78	0.0904	-0.2798
33	1028.85	1014.85	-14	1.7933	-2.8436
34	1043.14	1028.68	-14.47	11.5709	-10.3451
35	1086	1064.32	-21.67	3.7595	-5.9602
36	1099.82	1090.02	-9.8	0.2988	0.2074
37	1151.39	1140.97	-10.41	10.6573	-9.7879
38	1169.46	1159.78	-9.68	11.371	4.8761
39	1194.53	1218.01	23.48	1.8519	-3.1478
40	1227.99	1197.75	-30.24	1.0734	-4.2624
41	1233.38	1211.8	-21.58	4.8164	-3.3207
42	1258.46	1233.65	-24.81	11.4601	-5.9056
43	1297.02	1273.18	-23.84	56.8074	-61.3435
44	1320.81	1294.81	-26.01	9.6565	-10.0094
45	1345.65	1322.34	-23.31	10.2981	-6.1336
46	1363	1334.04	-28.96	51.2869	-14.1909
47	1421.36	1385.96	-35.41	5.8191	-8.7165
48	1427.85	1396.52	-31.33	32.0354	-63.8054

Calculated fundamental frequencies for HBQ in CCl_4, continued. [3]

Mode	ω (Harm., cm^{-1})	ω (Anharm., cm^{-1})	$\Delta\omega$ (cm^{-1})	I (a.u.)	Δ I (a.u.)
49	1449.87	1429.73	-20.14	10.158	-8.111
50	1465.99	1442.64	-23.35	32.7638	-29.3738
51	1506.5	1458.22	-48.28	48.0777	-32.5189
52	1535.57	1503.22	-32.35	0.008	-7.4099
53	1565.3	1535.17	-30.12	0.4345	-77.9046
54	1609.25	1572.25	-37	1.4259	-91.1499
55	1625.62	1587.27	-38.35	41.63	-21.0633
56	1648.72	1617.39	-31.33	12.5942	9.012
57	1663.6	1615.71	-47.89	1.4772	-59.0538
58	3148.4	2716.86	-431.54	231.4866	-444.6869
59	3163.28	3032.42	-130.86	1.5828	-4.0146
60	3164.93	3112.43	-52.49	91.4634	21.3671
61	3167.59	3048.23	-119.36	168.988	164.1226
62	3170.88	3022.6	-148.29	74.6021	47.4757
63	3180.31	3053.42	-126.89	34.9799	27.5382
64	3182.96	3026.91	-156.05	114.3829	79.3012
65	3194.04	3090.76	-103.28	10.435	-4.3122
66	3199.73	3068.94	-130.79	2.7653	-2.8189

BIBLIOGRAPHY

[1] M. Khalil, O. Golonzka, N. Demirdöven, C. J. Fecko, and A. Tokmakoff, "Polarization-selective femtosecond Raman spectroscopy of isotropic and anisotropic vibrational dynamics in liquids," *Chemical Physics Letters*, vol. 321, pp. 231–237, Apr. 2000.

[2] D. McMorrow and W. T. Lotshaw, "The frequency response of condensed-phase media to femtosecond optical pulses: spectral-filter effects," *Chemical Physics Letters*, vol. 174, pp. 85–94, Oct. 1990.

[3] M. Balasubramanian, A. Reynolds, T. J. Blair, and M. Khalil, "Probing Ultrafast Vibrational Dynamics of Intramolecular Hydrogen Bonds with Broadband Infrared Pump-Probe Spectroscopy," *Chemical Physics*, vol. 519, pp. 38–44, Mar. 2019.

Appendix B

SUPPORTING INFORMATION: SPECTRAL SIGNATURES OF ULTRAFAST EXCITED STATE INTRAMOLECULAR PROTON TRANSFER FROM COMPUTATIONAL MULTI-EDGE TRANSIENT X-RAY ABSORPTION SPECTROSCOPY

Relevant publications, with the permission of ACS publishing:

- [1] Caroline M. Loe, Chelsea Liekhus-Schmaltz, Niranjan Govind, and Munira Khalil, "Spectral Signatures of Ultrafast Excited-State Intramolecular Proton Transfer from Computational Multi- edge Transient X-ray Absorption Spectroscopy, J. Phys. Chem. Lett, Vol. 12, no. 40, pp. 9840–9847, 2021.

B.1 Steady State Calculations

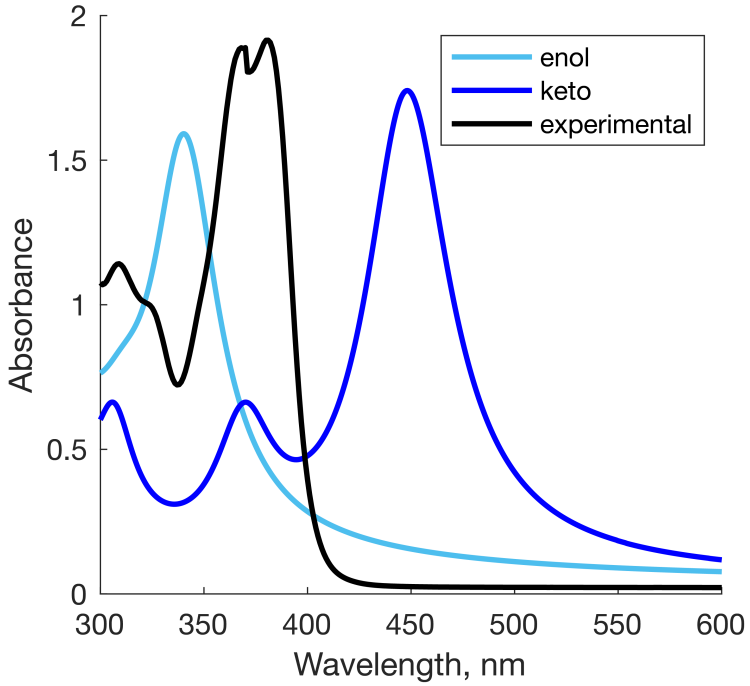

Figure B.1. Calculated and experimental UV-vis spectra of HBQ. Lowest energy peak shown for both calculations (enol, light blue; keto, dark blue).

B.2 Molecular Dynamics Simulations

Atom distances in geometries from each step of the *ab initio* molecular dynamics simulations are plotted under an average. Only atoms involved in proton transfer were chosen for analysis. Ground and excited state geometries are compared in table S1. Geometries of the ground state enol and enol* are the same, as expected at time 0.

Table B.1. O···H, N–H, N···O distances (Å) in ground and excited state geometries

	O···H	N···H	N···O
E[a]	1.003	1.643	2.562
E*[b]	1.003	1.643	2.562
K[a]	1.575	1.063	2.517
K*[c]	1.707	1.036	2.605

[a] From ground state geometry optimizations; [b] From zeroth step of excited state geometry optimization; [c] From excited state geometry optimization.

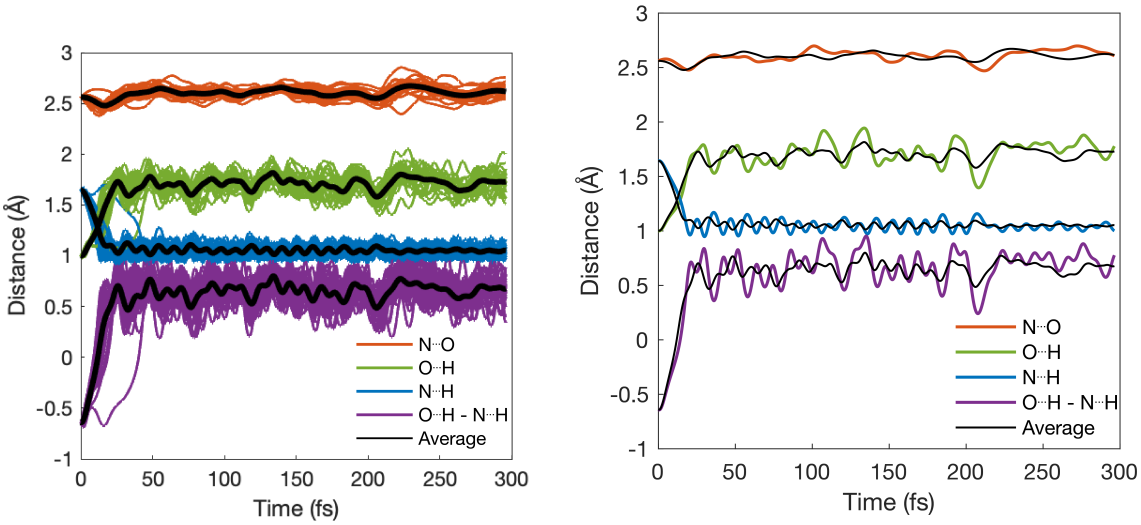

(a) All 25 excited state AIMD trajectories, with an average.

(b) Single excited state AIMD trajectory used for LR-TDDFT XANES calculations.

Figure B.2. Distances between atoms in excited state AIMD trajectories from 0 to 300 fs, shown in color. Averages are plotted in black.

B.3 Excited State XAS Calculations

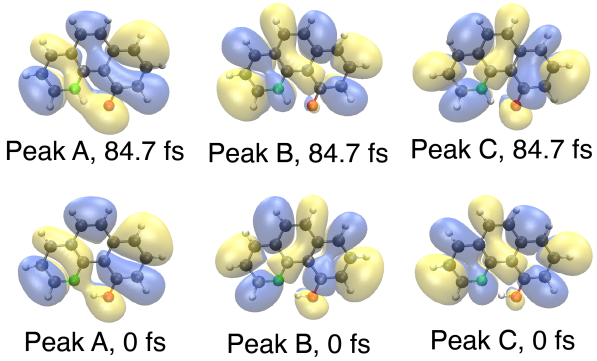

Figure B.3. Excited state molecular orbitals corresponding to the dominant final state orbitals involved in transitions A, B, C in transient spectra. Molecular orbitals are shown for the E* and K*, and were calculated from excited state geometries as described in the Computational Methods section.

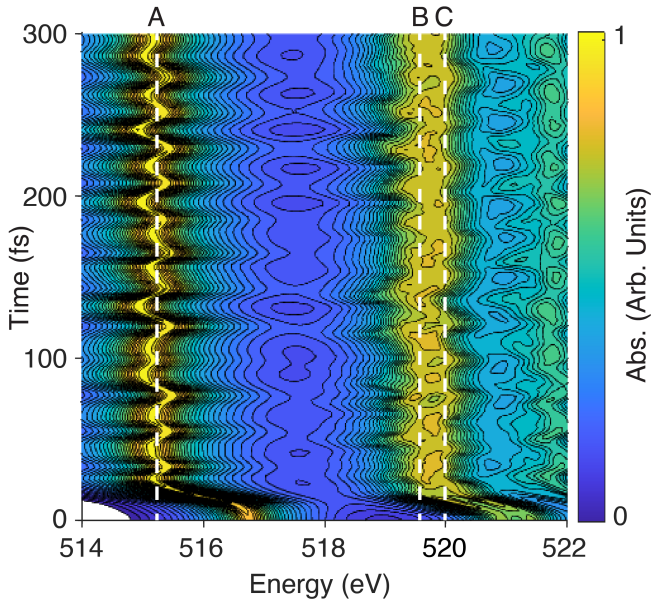

Figure B.4. Average of 20 calculated ultrafast transient XAS at the oxygen K-edge for 300 fs, plotted on a logarithmic scale and normalized. Contour levels are drawn every 3% after a minimum cutoff value (in white). Dashed vertical lines denote the long-time average of each peak at 515.3 eV, 519.5 eV, and 520.0 eV. 20 trajectories were selected at random from the total original 25.

B.4 Fourier Analysis

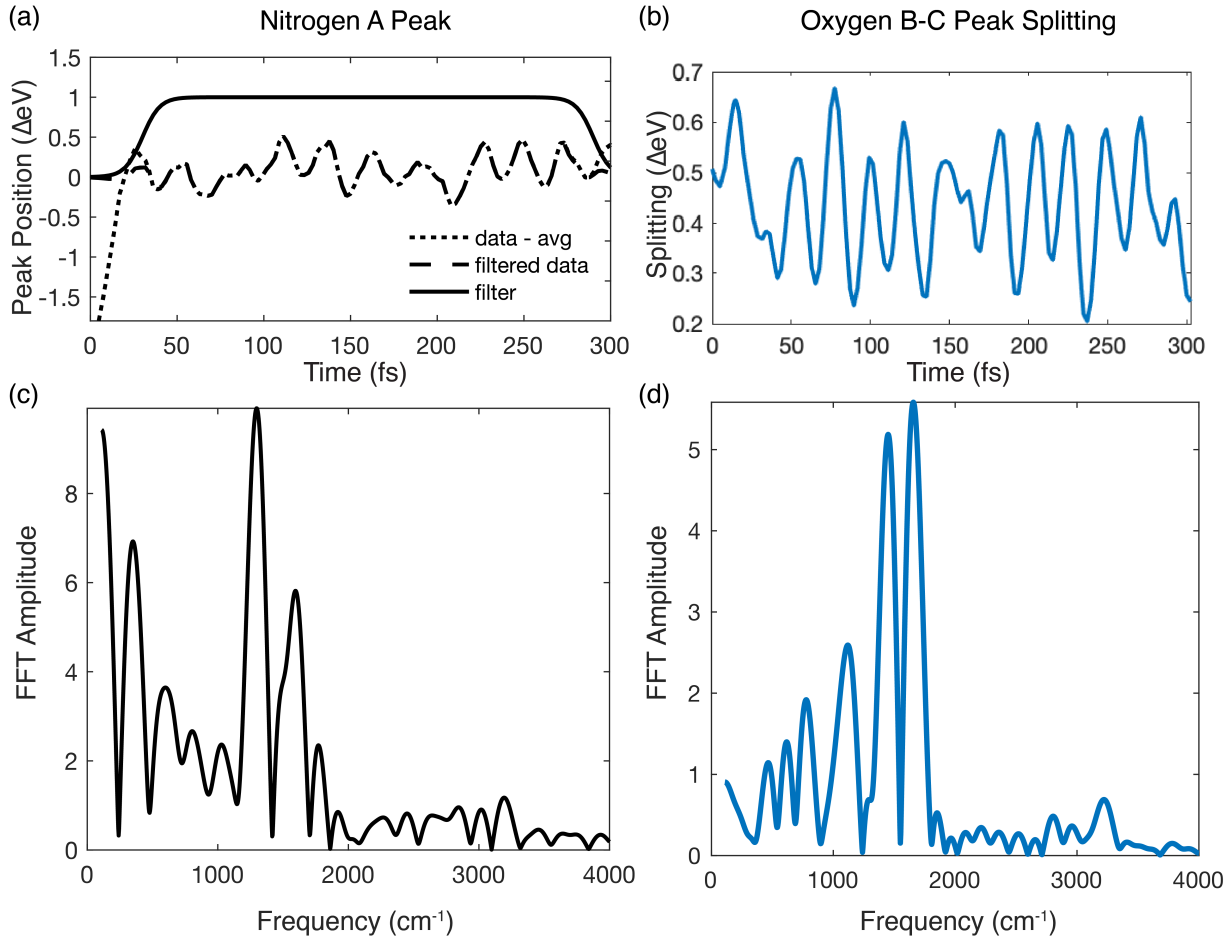

Figure B.5. a) Time trace of nitrogen A peak with windowing function, b) Time trace of splitting between oxygen B and C peaks, c) Fourier transform of nitrogen A peak, and d) Fourier transform of oxygen B-C splitting.

Table B.2. Average atom distances (Å) for peaks and troughs of spectral features chosen for Fourier analysis.

		O···H	N–H	N···O
Nitrogen A:	peaks	1.77	1.04	2.62
	troughs	1.66	1.06	2.60
Nitrogen B:	peaks	1.79	1.06	2.62
	troughs	1.67	1.04	2.61
Oxygen A:	peaks	1.64	1.10	2.62
	troughs	1.77	1.04	2.60

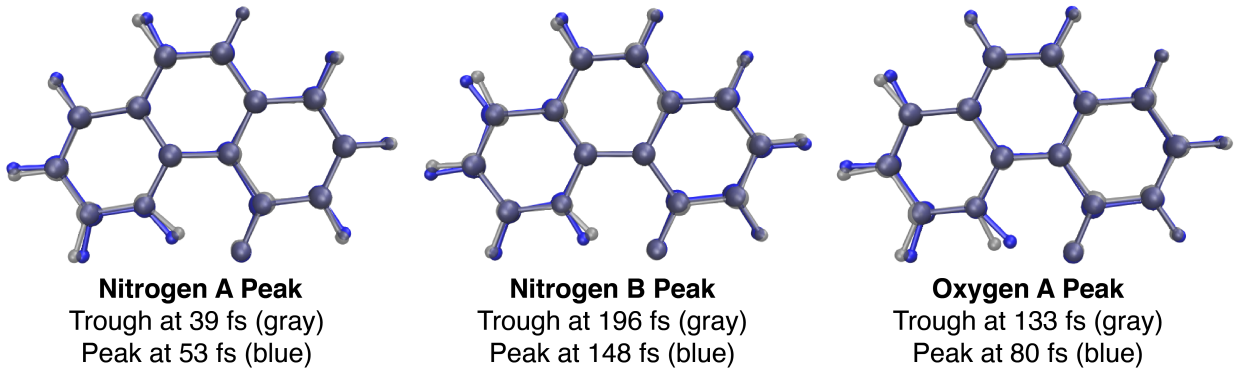

Figure B.6. Shifting geometries at one peak and one trough time point for nitrogen A/B and oxygen A peaks. Troughs (lower energy) are in gray and peaks (higher energy) are blue. In the nitrogen excited state XAS, there is a shorter distance between O and H atoms, while the opposite is true for the oxygen XAS. See Table S2 for average distances.

Table B.3. Frequencies from the Fourier transform of the nitrogen XAS A peak position compared to frequencies from a harmonic excited state frequency calculation (cont. on next page).

Nitrogen A Peak XAS Frequency	**Intensity**	**K* Mode**	**Intensity (a.u.)**	**Mode Description**
351 cm^{-1}	6.9	**375 cm^{-1}**	0.016	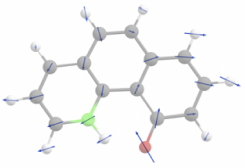
598 cm^{-1}	3.6	**636 cm^{-1}**	0.053	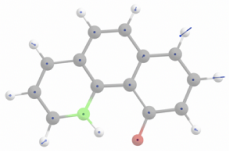
805 cm^{-1}	2.7	**800 cm^{-1}**	0.001	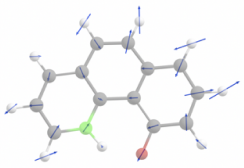
		866 cm^{-1}	0.018	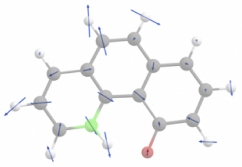
1029 cm^{-1}	2.4	**1007 cm^{-1}**	0.033	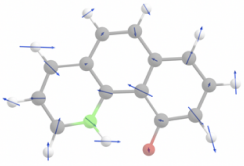
		1018 cm^{-1}	0.062	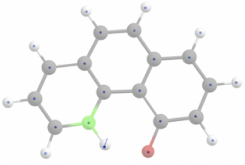

XAS Frequency	Intensity	K* Mode	Intensity (a.u.)	Mode Description
		1036 cm^{-1}	0.058	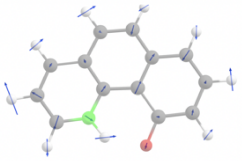
		1065 cm^{-1}	0.209	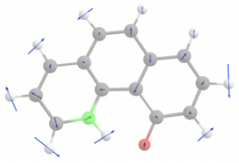
1296 cm^{-1}	9.9	**1287 cm^{-1}**	0.080	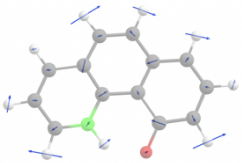
		1319 cm^{-1}	0.262	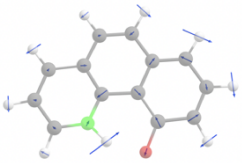
1594 cm^{-1}	5.8	**1580 cm^{-1}**	0.019	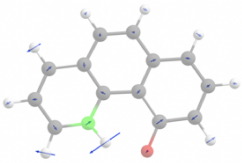
		1590 cm^{-1}	0.092	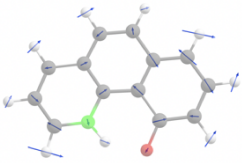
1771 cm^{-1}	2.3	**1747 cm^{-1}**	1.428	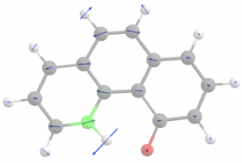
3194 cm^{-1}	1.2	**3181 cm^{-1}**	1.805	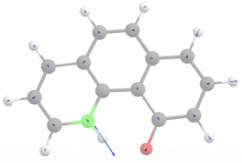

Table B.4. Frequencies from the Fourier transform of the nitrogen XAS B peak position compared to frequencies from a harmonic excited state frequency calculation (cont. on next page).

Nitrogen B Peak XAS Frequency	Intensity	K* Mode	Intensity (a.u.)	Mode Description
354 cm^{-1}	4.8	**375 cm^{-1}**	0.016	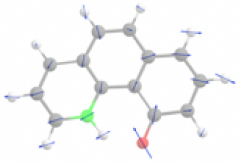
611 cm^{-1}	4.6	**636 cm^{-1}**	0.053	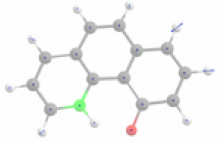
832 cm^{-1}	2.9	**866 cm^{-1}**	0.019	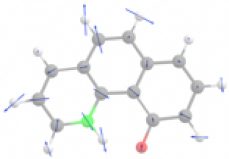
1012 cm^{-1}	2.7	**1007 cm^{-1}**	0.033	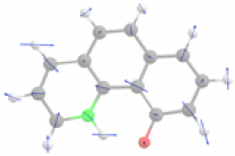
		1018 cm^{-1}	0.062	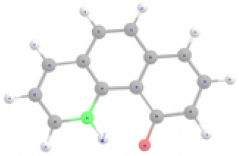
		1036 cm^{-1}	0.058	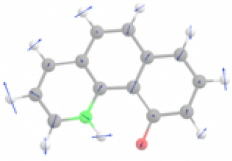
		1065 cm^{-1}	0.209	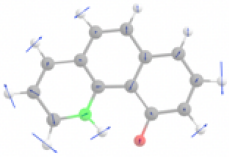

XAS Frequency	Intensity	K* Mode	Intensity (a.u.)	Mode Description
1306 cm^{-1}	11.2	**1287 cm^{-1}**	0.080	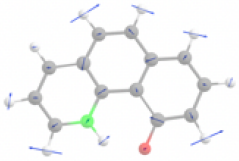
		1319 cm^{-1}	0.262	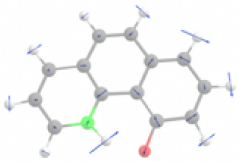
1470 cm^{-1}	3.3	**1450 cm^{-1}**	0.189	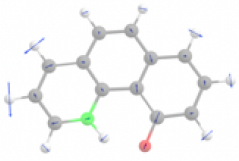
		1496 cm^{-1}	0.123	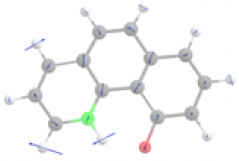
1597 cm^{-1}	4.8	**1580 cm^{-1}**	0.019	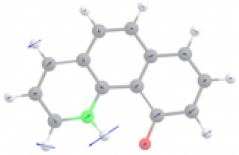
		1590 cm^{-1}	0.092	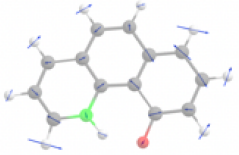
1751 cm^{-1}	2.4	**1747 cm^{-1}**	1.428	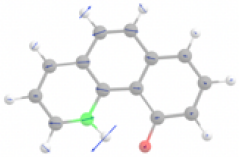
3217 cm^{-1}	2.1	**3181 cm^{-1}**	1.805	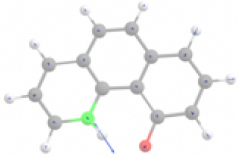

Table B.5. Frequencies from the Fourier transform of the oxygen XAS A peak position compared to frequencies from a harmonic excited state frequency calculation.

Oxygen A Peak XAS Frequency	**Intensity**	**K* Mode**	**Intensity (a.u.)**	**Mode Description**
297 cm^{-1}	3.4	**250 cm^{-1}**	0.058	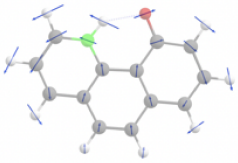
775 cm^{-1}	4.7	**800 cm^{-1}**	0.001	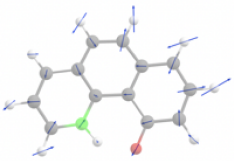
1139 cm^{-1}	6.1	**1149 cm^{-1}**	0.063	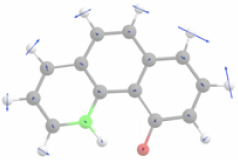
1306 cm^{-1}	6.2	**1319 cm^{-1}**	0.262	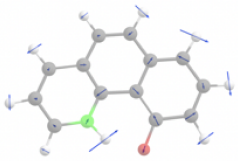
1467 cm^{-1}	11.9	**1450 cm^{-1}**	0.189	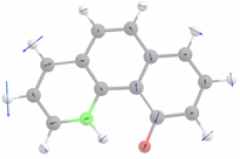
1654 cm^{-1}	22.1	**1590 cm^{-1}**	0.092	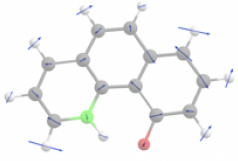
1841 cm^{-1}	3.8	**1747 cm^{-1}**	1.428	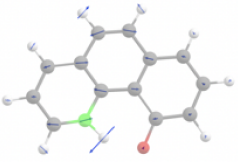
3220 cm^{-1}	3.5	**3181 cm^{-1}**	1.805	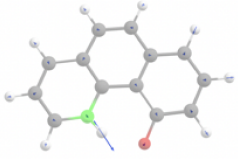

B.5 Calculation Examples

Table B.6. Representative input files from calculations on NWChem have been included to provide an example of each type of calculation used in this work.

File Name	Description
input-gs-opt	ground state geometry optimization input (enol)
input-uvvis-open	ground state UV-Vis input (enol)
input-N-enol-xanes-open	ground state nitrogen K-edge XANES input
input-opt-root1	excited state geometry optimization input
input-es-md-rand-7	*ab initio* molecular dynamics input (0-135 fs)
input-root1-000	SCF converged for excited state geometry
input-swap-000	Occupancy swap to obtain excited state molecular orbitals
input-es-freq	K* harmonic frequencies input

```
echo

start HBQ-enol-pce-opt

scratch_dir /scratch

#memory stack 1600 mb heap 100 mb global 3000 mb noverify
memory 7500 mb noverify
#memory 8192 mb noverify

charge 0

geometry units angstroms nocenter noautoz noautosym
load ./HBQ-enol.xyz
end


basis "ao basis" spherical print
  * library Def2-TZVP
end

driver
 xyz HBQ-enol-pce-open-opt
 maxiter 200
end

cosmo
 do_gasphase false
 dielec 2.5
end

dft
  xc pbe0
  maxiter 500
  mulliken
  direct
  tolerances tight
end
task dft optimize
```

```
echo

start HBQ-enol-pce-open-uvvis

scratch_dir /scratch

#memory stack 1600 mb heap 100 mb global 3000 mb noverify
memory 7500 mb noverify
#memory 8192 mb noverify

charge 0

geometry units angstroms nocenter noautoz noautosym
load ./HBQ-enol-pce-open-opt-010.xyz
end


basis "ao basis" spherical print
  * library Def2-TZVP
end

driver
 xyz HBQ-enol-pce-open-uvvis
 maxiter 200
end

cosmo
 do_gasphase false
 dielec 2.5
end

dft
  odft
  xc pbe0
  maxiter 500
  mulliken
  direct
  vectors input HBQ-enol-pce-opt.movecs output HBQ-enol-pce-open-
uvvis.movecs
end
#task dft optimize
#task dft freq

tddft
  civecs
  nroots 50
  notriplet
end
task tddft
```

```
echo

start HBQ-enol-pce-open-Nkedge

scratch_dir /scratch

#memory stack 1600 mb heap 100 mb global 3000 mb noverify
memory 7200 mb noverify
#memory 8192 mb noverify

charge 0

geometry units angstroms nocenter noautoz noautosym
load ./HBQ-enol-pce-open-opt-010.xyz
end


basis "ao basis" spherical print
  * library Def2-TZVP
end

#driver
# xyz HBQ-tce-opt.out
# maxiter 200
#end

cosmo
 do_gasphase false
 dielec 2.5
end

dft
  odft
  xc pbe0
  maxiter 500
  mulliken
  direct
  vectors input HBQ-enol-pce-open-opt.movecs output HBQ-enol-pce-open-
Nkedge.movecs
end

set tddft:do_s2 .false.
tddft
  ewin -15 -14
  cis
  civecs
  nroots 50
  notriplet
end
task tddft
```

```
echo

start HBQ-enol-pce-opt-root1

scratch_dir /scratch

#memory stack 1600 mb heap 100 mb global 3000 mb noverify
memory 7200 mb noverify
#memory 8192 mb noverify

charge 0

geometry units angstroms nocenter noautoz noautosym
load ./HBQ-enol-pce-opt-010.xyz
end

basis "ao basis" spherical print
  * library Def2-TZVP
end

driver
 xyz HBQ-enol-pce-opt-root1
 maxiter 200
end

cosmo
 do_gasphase false
 dielec 2.5
end

set lindep:n_dep 0

dft
  xc pbe0
  maxiter 500
  mulliken
  direct
end

set tddft:do_s2 .false.
tddft
  cis
  civecs
  nroots 10
  notriplet
  grad
    root 1
  end
end
#task dft
```

```
task tddft optimize
```

```
echo

restart HBQ-enol-pce-freq-root1-qmd-rand-7

scratch_dir /scratch

#memory stack 1600 mb heap 100 mb global 3000 mb noverify
memory 7200 mb noverify
#memory 8192 mb noverify

charge 0

geometry units angstroms nocenter noautoz noautosym
 load ./HBQ-enol-pce-opt-root1-000.xyz
end

basis "ao basis" spherical print
  * library Def2-TZVP
end

cosmo
 do_gasphase false
 dielec 2.5
end

set lindep:n_dep 0

dft
  xc pbe0
  maxiter 500
  mulliken
  direct
end

set tddft:do_s2 .false.
tddft
  cis
  civecs
  nroots 1
  notriplet
  grad
    root 1
  end
end

qmd
  nstep_nucl  20000
  dt_nucl     10.0
  com_step    10
  rand_seed   77426
```

```
  thermostat  none
  print_xyz   1
end
task tddft qmd
```

```
echo

start md-root1-000

scratch_dir /scratch

#memory stack 1600 mb heap 100 mb global 3000 mb noverify
memory 7200 mb noverify
#memory 8192 mb noverify

charge 0

geometry units angstroms nocenter noautoz noautosym
load ./es-md-rand-7-000.xyz
end

basis "ao basis" spherical print
  * library Def2-TZVP
end

cosmo
 do_gasphase false
 dielec 2.5
end

# enforces no linear dependent vectors
set lindep:n_dep 0

dft
  odft
  xc pbe0
  maxiter 500
  mulliken
  direct
  vectors output md-root1-000.movecs
end
task dft
```

```
echo

start md-root1-000

scratch_dir /scratch

#memory stack 1600 mb heap 100 mb global 3000 mb noverify
memory 7200 mb noverify
#memory 8192 mb noverify

charge 0

geometry units angstroms nocenter noautoz noautosym
load ./es-md-rand-7-000.xyz
end

basis "ao basis" spherical print
  * library Def2-TZVP
end

cosmo
 do_gasphase false
 dielec 2.5
end

 occup
 55 55
load ./occup.inp
end

# enforces no linear dependent vectors
set lindep:n_dep 0

dft
  odft
  xc pbe0
  maxiter 500
  mulliken
  direct
  vectors input md-root1-000.movecs output md-swap-alpha-
root1-000.movecs
end
task dft
```

```
echo

start HBQ-enol-pce-freq-root1-qmd

scratch_dir /scratch

#memory stack 1600 mb heap 100 mb global 3000 mb noverify
memory 7200 mb noverify
#memory 8192 mb noverify

charge 0

geometry units angstroms nocenter noautoz noautosym
 load ./HBQ-enol-pce-opt-root1-000.xyz
end

basis "ao basis" spherical print
  * library Def2-TZVP
end

cosmo
 do_gasphase false
 dielec 2.5
end

set lindep:n_dep 0

dft
  xc pbe0
  maxiter 500
  mulliken
  direct
end

set tddft:do_s2 .false.
tddft
  cis
  civecs
  nroots 1
  notriplet
  grad
    root 1
  end
end

qmd
  nstep_nucl  20000
  dt_nucl     10.0
  com_step    10
  rand_seed   12345
```

```
  thermostat  svr 100
  print_xyz   1
  targ_temp   298.15
end
task tddft qmd
```

BIBLIOGRAPHY

[1] C. M. Loe, C. Liekhus-Schmaltz, N. Govind, and M. Khalil, "Spectral signatures of ultrafast excited-state intramolecular proton transfer from computational multi-edge transient x-ray absorption spectroscopy," *The Journal of Physical Chemistry Letters*, vol. 12, pp. 9840–9847, Oct. 2021.

Appendix C

TRANSIENT INFRARED SPECTROSCOPY OF 10-Hydroxybenzo[*h*]quinoline

Few transient infrared spectroscopy (tIR) experiments have previously been done at the NH stretching region of a proton transfer complex. Very early in the development of optical pump-probe spectroscopy (in 1986), Elsaesser et al. performed tIR on 2-(2-hydroxyphenyl)-bezothiazole (HBT), an excited state intramolecular proton transfer (ESIPT) compound, at both the OH/NH stretching region and the carbonyl stretching region. They had an experimental time resolution of ≈6 ps and were able to observe the absorption of both the NH stretch and the carbonyl stretch in the electronic excited state, which provided direct evidence for the existence of an ESIPT. [1] To our knowledge, since then no one has performed tIR on an ESIPT complex at the OH/NH stretching region. HBQ is an excellent candidate for this experiment, especially since we know from tIR and 2D EV experiments in the carbonyl stretching region that there are oscillations on the electronic excited state. [2] Other tIR, IR pump-probe, and 2D IR experiments on NH stretches in solution have been performed. [3–6]

Following photoexcitation of HBQ with the BBnUV pump line, we observed a negatively signed transient signal in transmission mode (excited state absorption at the NH stretching region) with oscillations in it (Fig. C.1(a)). It appeared to decay multiexponentially and was very broad across the detection wavelengths, which is consistent for hydrogen bonded NH stretches. [3] Figures C.1(b) and (c) show the fast Fourier transform of the averaged tIR signal in (a). The experimental layout is the same as that described in Chapter 2, with the exception of using a single IR probe pulse and increasing the power of the BBnUV pump to a range of 150-600 nJ. The spectra shown here were collected with a 500 nJ pump pulse.

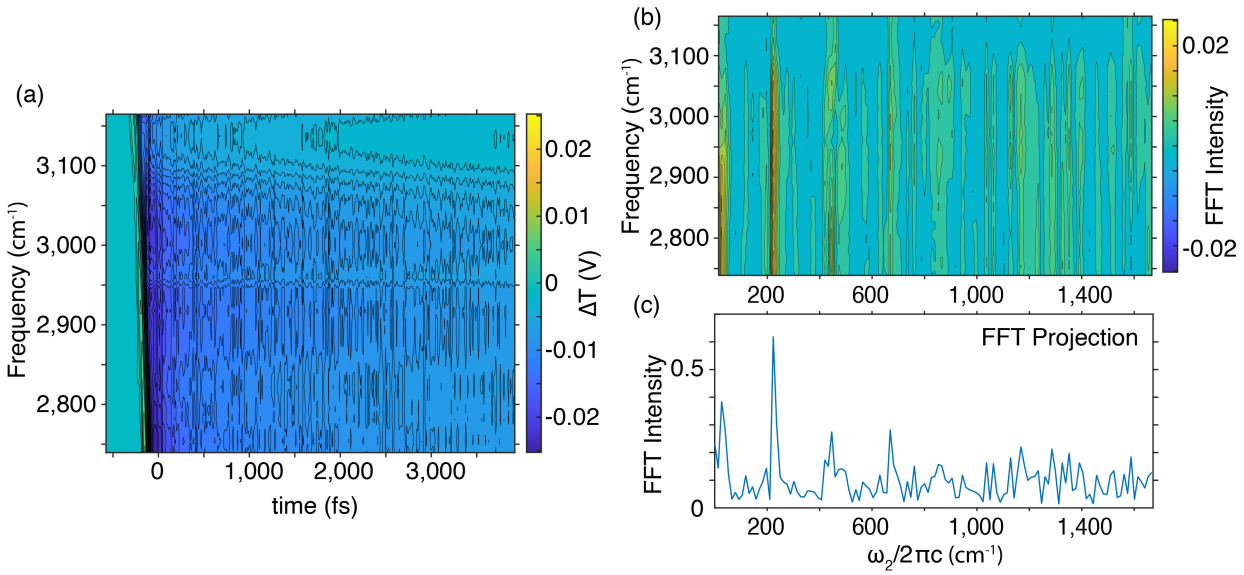

Figure C.1. Transient IR spectrum of HBQ in CCl_4 with Fourier transformed spectrum. a) Transient IR at the NH stretch, grating centered at 2950 cm^{-1} with 10 fs steps. b) Absolute value FFT of the tIR spectrum, following subtraction of biexponential decay and windowing with a hyperbolic tangent function. c) Projection of the frequencies in (b). Spectra are not normalized by the probe, and contours in (a) and (b) are plotted every 5% from 10% to 100%.

Three sets of averaged time domain data were collected out to 3 ps (ZZZZ polarization) with 10 fs steps. The FFT's used 2^8 zero padding. Chirp in the IR probe pulse from a ZnSe polarizer before the sample area causes a phase flip in the FFT surface (Fig. C.1(b)), which is why the absolute value is shown. There are several strong low frequency modes above the noise level in Fig. C.1(c). Unfortunately, we found that the strength of the signal depended on where the incident beams hit the sample cell.

With the pump and probe hitting a fresh spot on the sample cell window, the tIR signal was very weak and grew in after ≈5-10 seconds of irradiation with the pump and probe beams when the pump pulse energies were 500 nJ. After decreasing the pump energy to 150 nJ per pulse and moving to a fresh spot, the same effect occurred but on a slower timescale. If nothing was moved, the pump and probe were blocked, and the sample was left to flow for

up to an hour, when the beams were unblocked again, the "problem spot" was still there. This led us to believe that some form of photodamage from the visible pump or an effect of the chlorinated solvent interacting with CaF_2 windows was causing sample to stick to the sample cell windows. It is also plausible that the observed increase in signal strength was not caused by photodamage, but by an increased concentration at the irradiated site on the CaF_2 window. The BBnUV pump spot size was the same as it had been for VE experiments (≈135 µm), while the IR probe spot size was ≈160-180 µm. A 100 µm teflon spacer was used in the sample cell. Dissolving fresh sample, cleaning the sample cell windows, and redoing pump-probe overlap through the pinhole did not prevent this effect. The BBnUV pump spot size was increased to around 200 µm, while the IR probe remained around 170-180 µm. The signal did plateau after some time, and also happened at other grating positions. With a dilution of HBQ in CCl_4 (<1 mM, used for rinsing the sample cell), if the beams passed through the same spot on the sample cell window that had been irradiated with the BBnUV light while the 25 mM solution flowed previously, the same magnitude of difference signal appeared. If the sample cell was moved off of that spot, the difference signal went away and grew back in on a much smaller scale, as might be expected for a very dilute sample. Repeating the experiment with 25 mM HBQ in tetrachloroethylene (PCE) yielded the same results. This may be an area to troubleshoot in future experiments at the NH stretch in HBQ. As far as we can tell, tIR and 2D EV experiments in the C=O stretching region and fingerprint region were not affected by this phenomenon, although the excited state vibrations in those regions absorb more strongly than the NH stretch does. If there is an overall stronger tIR signal in those regions than at the NH stretching region, changes in the signal strength in the ones to tens of mV would be less noticeable.

BIBLIOGRAPHY

[1] T. Elsaesser and W. Kaiser, "Visible and infrared spectroscopy of intramolecular proton transfer using picosecond laser pulses," *Chemical Physics Letters*, vol. 128, pp. 231–237, Jul. 1986.

[2] J. W. Sandwisch, *Investigation of the Role Nonadiabatic Energy Relaxation Plays in Excited State Intramolecular Proton Transfer using Multidimensional Electronic-Vibrational Spectroscopy*. PhD thesis, University of Washington, 2023.

[3] C. Greve, N. K. Preketes, H. Fidder, R. Costard, B. Koeppe, I. A. Heisler, S. Mukamel, F. Temps, E. T. J. Nibbering, and T. Elsaesser, "N–H Stretching Excitations in Adenosine-Thymidine Base Pairs in Solution: Pair Geometries, Infrared Line Shapes, and Ultrafast Vibrational Dynamics," *The Journal of Physical Chemistry A*, vol. 117, pp. 594–606, Jan. 2013.

[4] S. Knop, J. Lindner, and P. Vöhringer, "OH and NH Stretching Vibrational Relaxation of Liquid Ethanolamine," *Zeitschrift für Physikalische Chemie*, vol. 225, pp. 913–926, Oct. 2011.

[5] A. V. Tivanski, C. Wang, and G. C. Walker, "Vibrational Mode Coupling to Ultrafast Electron Transfer in $[(CN_5)OsCNRu(NH_3)_5]^-$ Studied by Femtosecond Infrared Spectroscopy," *The Journal of Physical Chemistry A*, vol. 107, pp. 9051–9058, Oct. 2003.

[6] A. M. Stingel, C. Calabrese, and P. B. Petersen, "Strong Intermolecular Vibrational Coupling through Cyclic Hydrogen-Bonded Structures Revealed by Ultrafast Continuum Mid-IR Spectroscopy," *The Journal of Physical Chemistry B*, vol. 117, pp. 15714–15719, Dec. 2013.

Appendix D

ALIGNING THE 800C OPA AND DFG

The generation of mid-infrared (MIR) pulses can be accomplished with the combination of a near-infrared (NIR) optical parametric amplifier (OPA), which produces two near-infrared pulses in the range of ≈1000–2000 nm, and a difference frequency generation (DFG) setup, which takes the output signal and idler pulses and uses a nonlinear crystal such as $AgGaS_2$ (AGS) to take the difference frequency. The OPA is seeded with the output of a Ti-Sapphire amplifier, ideally sub-100 fs pulses centered at 800 nm, with a $1/e^2$ beam diameter of ≈10 mm. The input beam is split in the OPA. A very small portion is focused into a sapphire to be spectrally broadened and generate white light using self phase modulation. A section of the spectrum of white light serves as the "signal." The "pump" is the 800 nm light. A second, and weak, portion of the 800 nm light mixes with the white light in a type I beta barium borate (BBO) crystal. The angle of the crystal with respect to the incoming beams dictates the phase matching conditions for which NIR wavelength of the white light (signal) is selected to be amplified by the 800 nm pump. The difference between the pump and the signal wavelength sets the wavelength of the "idler" pulse. The frequencies of signal and idler sum up to the frequency of the pump. For example, using an 800 nm pump and a 1350 nm signal, the wavelength of the idler will be 1964 nm. A second pass through the BBO with the stronger signal pulse and another, more intense pump pulse generates a much stronger idler pulse, which can then be used with the stronger signal pulse to generate MIR. The DFG output using the signal and idler will be the difference between the two frequencies, so in this case will be 4318 nm (2315 cm^{-1}). The angle of the AGS crystal in the DFG with respect to the incoming beams also dictates the phase matching conditions for the incoming NIR light, and therefore what exactly the center wavelength of the generated MIR pulse will

be.

The new OPA in lab 1 is a TOPAS-Prime from Light Conversion (via Coherent) and should require very little hands-on adjustment. However, you may need to align the double-pass OPA-800C previously used in lab 1 and/or build a DFG setup. The aspect of this alignment which has the greatest impact on overall MIR light stability is the quality of the white light. Refer to Fig. D.1 for the alignment procedure below. The OPA was a commercial purchase from Spectra Physics (c. 2007), and the breadboard it came on does not have many spots for irises. Much of the alignment needs to be done by eye, looking at the overlap of visible beams on a white business card.

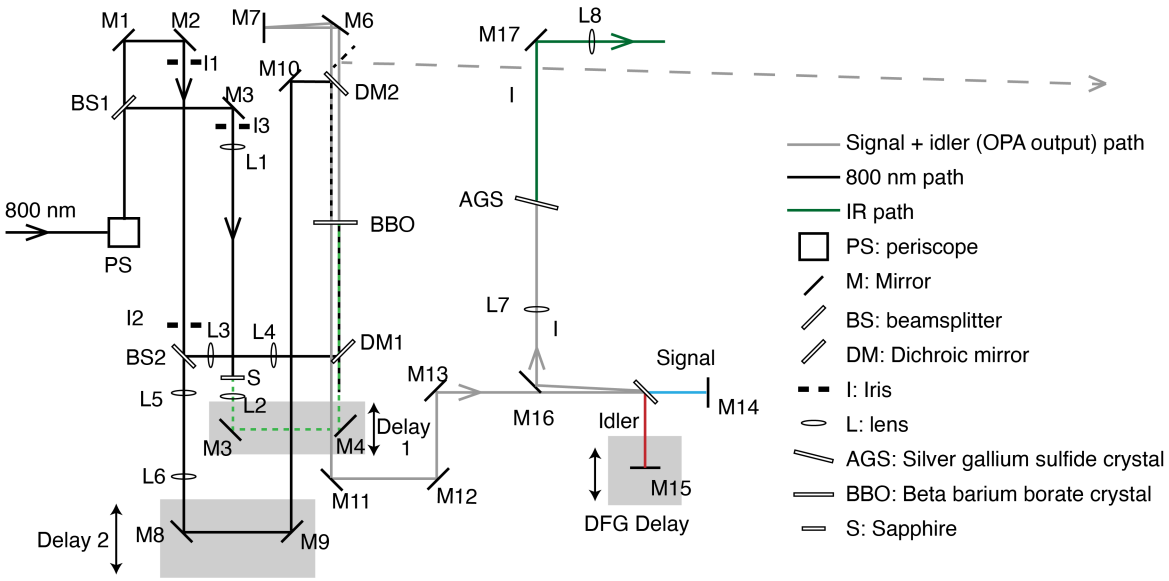

Figure D.1. Layout of OPA-800C and home-built DFG.

OPA and DFG Alignment

1. Place a card or beam block between I2 and BS2, and one card or beam block before M4.

2. The OPA should be seeded with 0.8–1 mJ of 800 nm light, polarized horizontally in the

laboratory plane. The periscope will flip the polarization at the input from horizontal to vertical.

3. The 800 is split at BS1 for white light generation (reflection, very weak) and for the OPA pump (transmission). Check that the pump arm is on the irises at I1 and I2. Then check that the white light is centered on the iris at I3. The lenses should not need adjusting if the input beam is collimated.

4. Check the white light quality and compression. Look at a business card after the sapphire and lens, between M3 and M4. Close the iris (I3) for the 800 nm light before the sapphire down most of the way, until there is almost no light left on the card. There should be a faint red dot in the center surrounded by flickering redish yellow light. It helps to turn off the lights to see better.

5. Adjust the compression of the amplifier (Spitfire Pro) using the stage motor on the laptop. The two options, "jog" and "cycle" do different things. "Jog" moves the stage a discrete amount per click of the mouse. "Cycle" moves the stage as long as the clicker on the mouse is held down. Start by using the second or third slowest speed of the stage (adjusted on the slider) and watch the faint light on the card. If it gets brighter, the amplifier output is closer to compressed. Try to optimize the brightness of the white light on the card. Each time the white light gets brighter, close down the iris a little bit more to avoid saturating the sapphire and to be able to see changes in white light generation more easily. When you have optimized the compression, open the iris just until there is a bright white light with no striations or interference patterns (this indicates that the sapphire is being saturated and could burn). The bright core of the white light should have a bluish halo around it. Figure 4.18 in Chapter 4 shows an example of good quality white light generated in a sapphire.

6. Check that the shape of the white light is round. If it's oblong, then the alignment

of the 800 nm seed through L1 and L2 is off. Adjust the pointing of BS1 and M3 to make the white light as round as possible. Then check that the path of the white light through the whole OPA is level and hits all the right optics.

7. Align the first pass of the OPA. Block the light transmitted through BS2. Place a card as close as possible to DM1 to look at the overlap of the white light transmitted through DM1 and the 800 reflected off of DM1. Adjust the pointing of BS2 (near-field) to bring the 800 nm beam to the center of the white light, looking at the white light core (not the colored rings).

8. Use a small floating pick-off mirror after DM2 to send the first pass to a far field and look at it on a card. The beams will diverge and make it easier to adjust alignment. Adjust the pointing of DM1 to bring the pump arm to the center of the white light. It may help to move slightly off of the timing with the first delay stage, then block half of the white light with a card from the top and side to see how well overlapped the beams are. The pre-amp arm will be blue after passing through the BBO when the delay 1 timing is off.

9. Repeat steps 7 and 8 until no more adjustments are needed, then adjust the timing of the first pass delay stage until there is a green halo around the center of the white light.

10. Look at the power at the exit of the OPA following only the first pass, placing the power meeter after M13. Keep the pump arm for the second pass blocked (after BS2). Depending on the input power to the OPA, you should be able to get close to 1.1-1.3 mW after the first pass on the blue Ophir power meter.

11. Align the second pass. Block the beam just after its second pass through DM2 (propagating towards the BBO) and unblock the power arm, which will reflect off of DM2. Adjust the pointing of M8 to center the 800 on the first pass output.

12. Look at the beams on a card between M11 and M12. Adjust the pointing of M10 so that they overlap.

13. Repeat steps 11 and 12 until no more adjustments are needed. Then look at the power after M13 and adjust delay 2 to maximize the output. With the first pass well aligned, aim for an output of 150–180 mW.

14. As a final check, place the floating long pass filter after M13. There should be a faint red dot and a blue dot. These are are overlapped with the signal and idler, and should stay collinear with one another into the far field. If they are not collinear, even if they are overlapped at the AGS crystal in the DFG, the output IR beam mode will be poor and unstable. Adjust the pointing of M8 and M10 so that these beams are collinear. Unfortunately this alignment is not an exact science and may take some trial and error.

15. Check the power output of the DFG. Aim for 2-3 µJ after the long pass filter (when the spectrum is centered at 4.8 µm — this will differ for other wavelengths). If the power is low and adjusting the DFG delay does not help, assume that the alignment and stability of the OPA are the problems. The DFG alignment is almsot never the problem.

16. Looking at the power of the DFG output, fine tune the pointing of M8 and M10, and iterate between adjusting delays 1, 2, and the DFG delay to optimize the power output.

17. To change the center wavelength output of the DFG, first align both the OPA and DFG. Look at the power of the IR and rotate the angle of the AGS crystal a couple degrees, without losing IR output. Then adjust the angle of the BBO in the OPA to maximize the power of the IR generated in the AGS.

Some other notes:

- If the OPA alignment seems great and the DFG output is still very very low (≈10% of the goal), then a weak back reflection of the signal from the dichroic beamsplitter might be interacting with the idler in the AGS. Move the DFG delay several mm away from its position to find the correct timing, scanning over the entire stage if necessary.

- There will be many many back and side reflections from the dichroic optics and various filters. Make sure that all of these are blocked.

- The gold mirrors (M11, M12, M13) at the end of the OPA burn easily. If the power seems low, check that the beams are not hitting any burn spots. If they are hitting burn spots, either rotate the mirrors or replace them. The same goes for the signal mirror in the DFG (M14).

- AGS burns very easily, so it is best to keep the DFG crystal on a translation stage to move in the X and Y directions without changing the pointing of anything in the DFG. You can also play with how close to the beam focus the AGS is placed after L7. (Remember that this may affect the IR beam mode and collimation.)

- Some polarizers are marked along the axis of transmitted light, and some are marked along the axis of the wires blocking light. Double check whichever polarizer you use if you need to check polarizations somewhere.

Aligning this OPA is more of an art than a science. It can take a lot of trial and error. Good luck!

Appendix E

LABVIEW AND MATLAB CODE FOR LAB 1

E.1 For τ_1

- **T1_HeNe_MCT_Interferogram_collect.vi**: Runs a fast scan. Collected through the DAQ.

- **XPS_Time_Scan_v6.vi**: Runs a step scan, or any kind of scan that steps a delay stage and is collected through the lock-in detector.

- **t1_FastScanWorkup.m**: Sorts bins and plots τ_1 fast scan.

- **FFT_linearScan.m**: Plots and fits step scan to a gaussian. The frequency axis will be more accurate with a longer τ_1 range (-1800 fs – +150 fs). Otherwise, use SingleC_IRF.m to plot step scan or just run and plot a fast scan if you want to see the IR spectrum.

E.2 For τ_2

- **XPS_Time_Scan_v6.vi**: Runs a step scan for a silicon trace. Be sure to trigger the lock-in from the visible chopper and change the stage to the appropriate one for τ_2.

- **SingleC_IRF.m**: Plots and fits the IRF obtained from a silicon trace.

E.3 CCD

- **CCDacquire_vTrial8.vi**: View a real-time spectrum or chopped signal on the CCD.

- **CCD_image_acquire_v_01.vi**: View a real time image of the entire 200 x 1600 pixel array.

- **CCDTime Scan_v5_rbw.vi**: Used for 1D VE and CaF_2 traces. Steps one stage (over τ_2) and collects data from the CCD.

- **cooler.vi**: Cools the CCD to -80° C. Currently required for all vi's that operate the CCD, although the noise level of our experiments really doesn't require deep cooling. (This is left over from Mike's and Trevor's attempts at a fifth order experiment).

- **VEfastScan_V06.vi**: Used for a τ_2 scan in 2D VE collection. Start cycling S2 (τ_1 delay) separately.

- **CCD_axis.m**: Calibrate the CCD axis (from pixels to nm).

- **ch8_timing.m**: Plot scans from channel 8 timing and CCD offset to determine correct settings.

- **XDVE_MCT_Iterative_plotter_rbw.m**: Plot the individual MCT data from 2D VE scans against the overall average to identify scans where the fast scanning was off.

- **ve_1d_t2_scan_workup_avg.m**: Plot an average of 1D VE scans in a directory with the same root name.

- **ve_1d_t2_scan_workup_rbw.m**: Plot individual 1D VE scans.

- **veFastScanFileFinder_DT_CCD_offs.m**: Function called by processing code for 2D VE scans (ve_fastscan_workup_file_finder_DT_CCD_offs.m).

- **ve_fastscan_workup_file_finder_DT_CCD_offs.m**: Processing code for raw 2D VE scans.

- **XDVEFastScanWorkup_v_03.m**: 2D VE processing code I have edited and added onto. More automated, but has more options, including ΔT/T math.

- **XDVEFastScanWorkup_v_03_rbw_original.m**: Original 2D VE processing code. Bare bones, but easier to troubleshoot and build off of. Does work for ΔT/T.

E.4 Other

- **FPAS2acqmainMX_UltrafastTIR.vi**: Use for real-time viewing of IR spectrum, chopped detection, and to collect transient IR. The 2D IR collection capability in this vi may need some work.

- **Read_lockin.vi**: Shows lock-in reading on computer.

- **spot_size_calculator.vi**: Calculates the $1/e^2$ spot size diameter based on full beam power and power through a pinhole. Be sure to double check the size of the pinhole used.

- **stage_cycling_extrema_calc.vi**: Calls the most recent $\tau_1 = 0$ fs position from the S2 notepad file and returns the stage positions to cycle between for a given τ_1 range (generally -1800 – +150 fs).

- **Time_Distance_conv.vi**: Convert between stage distance in mm and fs. 1 mm in stage distance is equivalent to 2 mm in beam path traveled since they are all retroreflectors.

VITA

Caroline M. Loe was born in Minneapolis, Minnesota in 1996. She attended St. Olaf College, where she studied Chemistry and Spanish and graduated cum laude with a Bachelor of Arts degree in 2018. She was also involved in the music department, singing in choir for one year and playing oboe and English horn in the Philharmonia orchestra for four years. Following graduation from St. Olaf, Caroline spent a year teaching English in Lugo, Spain. In the fall of 2019, she joined the Khalil group at the University of Washington where she remained for the duration of her Ph.D. studies until her defense in August 2024. In her free time she enjoys downhill skiing, hiking, backpacking, running, baking, knitting, and spending time with her family.